MULTI-DIMENSIONAL CHARACTERIZATION OF THE LASER AND ELECTRON BEAMS OF THE CORNELL ENERGY RECOVERY LINAC PHOTOINJECTOR PROTOTYPE

A Dissertation

Presented to the Faculty of the Graduate School

of Cornell University

in Partial Fulfillment of the Requirements for the Degree of

Doctor of Philosophy

by

Heng Li

August 2012

MULTI-DIMENSIONAL CHARACTERIZATION OF THE LASER AND ELECTRON BEAMS OF THE CORNELL ENERGY RECOVERY LINAC PHOTOINJECTOR PROTOTYPE

Heng Li, Ph.D.

Cornell University 2012

The Cornell Energy Recovery Linac (ERL) prototype photoinjector was built at Cornell University several years ago. The goal was to demonstrate that the photoinjector can produce the ultra-low emittance and high-current electron beam that will be used for the entire Cornell ERL facility. A high repetition-rate high-power Yb-doped fiber laser system produces the electron beam from a photocathode. The photocathode is one critical component of the photoinjector that can produce electron beams with low emittance, short bunch length, and high current. On the photocathode, the laser pulse shape maps to the electron bunch profile, and this mapping becomes complicated at higher bunch charge because of the virtual charge effect. The uniform ellipsoidal electron bunch distribution is the optimal distribution, because the linear space charge effect can be compensated by the linear optics downstream; the optimized laser pulse shape can be different because of the complicated mapping from the virtual charge effect. In order to achieve the optimized laser pulse shape, it requires three-dimensional (3D) laser pulse intensity shaping and 3D laser intensity diagnostics. We demonstrate the fidelity and accuracy of the 3D laser intensity diagnostic from a noncollinear first-order cross-correlator, and the optical temporal phase retrieval from the same setup. We also present the slice emittance measurement, that is, the time-resolved emittance measurement, at both near-zero

charge and 77 pC; it provides insight into the emittance compensation process and contributes to the emittance optimization. The calibrations and related issues are discussed as well. With such capabilities, we achieved the smallest emittances that have ever been measured from this photoinjector at 5 MeV beam energy with usable bunch charge, which was reported as one milestone of the Cornell ERL.

BIOGRAPHICAL SKETCH

I was born in Jiajiang, Leshan, Sichuan, People's Republic of China on October 20th, 1982. It is a beautiful small town with more than two thousand-year history and the Qiyi river running across it; and it is near the Mountain Emei, part of the Hengduan Mountains from Tibet to the middle west China. I had my high school education at Leshan No.1 Middle School which was founded in 1898. I left Sichuan and went to Anhui, which is thousands of kilometers from my home town for my undergraduate education at the University of Science and Technology of China from 2001 to 2005. After I received my Bachelor of Science degree, I came to Cornell University at Ithaca, New York, United States to pursue my further education. I spent two years working with Prof. Anders Ryd, on building and testing the pixel test station for the Compact Muon Solenoid (CMS) pixel detector test station for the Large Hadron Collider from 2006 to 2007. Although I was more interested in the data analyzing part, I did learn a lot from working on the detector hardware. Then I would like to pursue some research that had the more direct impact for the human beings, and joined Prof. Frank Wise's group, that focuses on the optical laser science and the quantum dots for the sustainable energy. I began to work on the high power high repetition rate Yb-doped fiber laser system for the Cornell ERL. Later, with the help from colleagues, I developed the multi-dimensional laser and electron beam characterization techniques in order to optimize the electron emittance of the Cornell ERL.

ACKNOWLEDGEMENTS

First of all, I would like to thank my advisor, Prof. Frank Wise, for his constant support and encouragement of my research and study, for his painstaking teaching on writing scientific papers, and for his words and deeds as a scientist. I am deeply thankful to Prof. Ivan Barazov, for his guidance on the numerical accelerator simulations as well as experiments, which has contributed a lot for what I have learned and also two chapters of this thesis. I am very thankful to Prof. Sol Gruner, for his guidance and kindly help on the big picture of the Cornell ERL. I am very thankful to Dr. Bruce Dunham, for his collaborations and support from the accelerator experiments to the inspiring discussions. I am very thankful to Prof. Andre' LeClair, for his guidance and help on understanding the intrinsic laser noise. I am very thankful to Prof. Ander Ryd, for his guidance and help on building and testing of the pixel test station at Cornell for the CMS detector.

I am very thankful to Dr. Zhi Zhao, for his insightful discussions of the laser science and the optical phase retrieval, and his help. I am very thankful to Prof. Andy Chong, for his collaborations and discussions on the Airy-Bessel pulse measurements. I am very thankful to Dr. Dimitre Ouzounov, for his collaborations and discussions on the starting dynamics of the dissipative soliton fiber lasers, and teaching me the laser optics in lab. I wish to thank Yang Zhang, for the perceptive discussions of the physics and his help. I wish to thank Shian Zhou, Khanh Kieu, Lyuba Kuznetsova, William Renninger, Simon Lefrancois, Luming Zhao, Hui Liu, Erin Stranford, Lingjie Kong, Peng Li for the stimulating discussions on the fiber laser physics. I wish to thank Adam Bartnik, for his support on the laser system and the accelerator experiments. I wish to thank John Dobbins, for his help on the automation of the beam diagnostics, and his

support of the beam experiments. I wish to thank Karl Smolenski, for his mechanical design of the mounts for the beam diagnostics and his support on the experiments. I wish to thank Shijie Yang, and David Kreinick, for their help on the computation resources. I wish to thank John Barley, Luca Cultrera, Yulin Li, Xianghong Liu, Florian Loehl, Rong Huang, Roger Kaplan, Atoosa Meseck, Peter Quigley, and Vadim Veshcherevich for teaching me the experimental accelerator physics. I wish to thank Colwyn Gulliford, for the discussion of accelerator physics and also making students laugh in the Wilson lab. I wish to thank Jim Shanks, Michael Ehrlichman, Joseph Calvey, Jared Maxson, and Hyeri Lee for the discussions on the accelerator physics. I wish to thank Dr. Tow Yee Yau, and Dr. Robert Mendola, for their help.

I wish to thank Debra Hatfield, Kacey Bray, Monica Wesley, Renee King, Peggy Steenrod, Todd Hawkins, and Lonie Sheldon, for helping me with administrative matters.

I wish to thank Hanying Li, Hao Peng, Wen Fu, Rong Long, Yeyun Zhou, Yang Xie, Qiu Zhao, Yi Xie, Yong Chen, Bo Li, Hongbo Han, Pu Wang, Jie Dai, Jian Hu, Ding Pan, Jingjiang Peng, Peng Zheng, Jun Yang, Xianpei Chen, Ji Cheng, Lin Xue, Peijun Zhou, Wan Li, Yongtao Cui, Huolin Xin, Mengqiao Wang, Luqiao Liu, Xinwei Wu, Pengsheng Ji, Yao Wang, Yi Yang, Shikui Wang, Shukui Zhang, Miao Wang, Lee Li, Luo Xiao, Kan Li, Chenchen Wan, Fan Yu, Shan Huang, Jie Gao, Jie Chen, Xiaoxu Lu, Ting Chen, Pingli Huang, Yu Tian, Jie Wang, Ru Zhang, and Yang Yang, for their help.

I am greatly indebted to my family, for giving me the physical and intellectual strength, and for encouraging and supporting me throughout my entire education.

Research presented in this thesis is supported by the National Science Foundation (NSF) award DMR-0807731. Portion of the laser work were supported by the NSF grants ECS-0701680 and PHY-0131508 and the National Institutes of Health (NIH) grant EB002019.

TABLE OF CONTENTS

LIST OF TABLES

LIST OF FIGURES

CHAPTER 1

INTRODUCTION

The x-ray was discovered by Wilhelm Röntgen in the 19th century and has been used in scientific experiments since then. Particle physicists built synchrotrons to study the fundamental elements that constitute this universe. When the relativistic charged electrons are bent by the magnetic field, they emit synchrotron radiation (SR). SR has wide spectrum range and can be used for scientific experiments such as biology, material science, and condensed matter physics [1].

Scientists built first-generation x-ray light sources in the 1960s, and the second-generation and third-generation later; most of them are storage rings. The brightness is one important parameter of these facilities. It is defined as the flux density in the phase space, and determines the angular resolution and signal-to-noise ratio in crystallography experiments. Higher brightness is preferred [1]. The undulator and wiggler were developed to improve the brightness. The undulator has many alternating dipole magnets with a small spatial period; the traveling electrons produce SR that can be added coherently together to improve brightness. The wiggler has less dipole magnets with a relative larger spatial period, and can produce greater bandwidth radiation. The third-generation x-ray light sources were designed to have longer straight sections [2]. The undulators and wigglers are inserted at these sections, where the electron beam emittance is small to give high brightness. In the third-generation x-ray sources, the technology is mature after forty-year development and almost all the phenomena are well understood both theoretically and experimentally [3, 4, 5, 6].

The brightness is still a premium for the x-ray users, but the storage ring structure puts an upper limit on the achievable brightness. SR happens in a quantized manner, and it has fluctuations in both the wavelength and intensity. This effect changes the original electron momenta, and smears out their distributions. After thousands of round trips, the electron beams reach the equilibrium state: the phase space distributions are Gaussian because of the central limit theorem. Because the bending and the SR happen mostly in the horizontal plane, its phase space volume is larger compare to the one in the vertical plane, by 10 to 100 times [2]. Although there is still space for optimization by improving the lattice structure, by focusing the beam before the bending magnets, the upper limit of brightness is imposed by the equilibrium process. Another limitation is the electron bunch length. In the state-of-the-art storage rings, it is tens of picosecond. However, to probe the chemical reactions requires x-ray pulse less than 100 femtosecond; these require more advanced light sources [3, 4, 5, 6].

In the linear accelerators (linacs), there are no such limitations from the equilibrium process, because the electron beams are only accelerated once and can preserve their properties from the injectors. Nevertheless, the power consumption becomes a real concern: for a 5 GeV, 100 mA linac, the power is 500 MW. It requires a power plant for one facility. However, if the energy can be recycled, the concept becomes feasible [5, 6, 7]. Tigner had the idea of the Energy Recovery Linac (ERL) back in the 1970s, and proposed that it can be realized by high repetition Superconducting Radio-Frequency (SRF) cavities [2]. The perimeter of the facility is designed such that after one round trip, the phase differences between the previous and current electron bunches are out of phase by π [Fig. 1.1]. Then the phases from the preceding electrons are in-trough, and their energies are deposited to the SRF cavities. The newly injected electrons

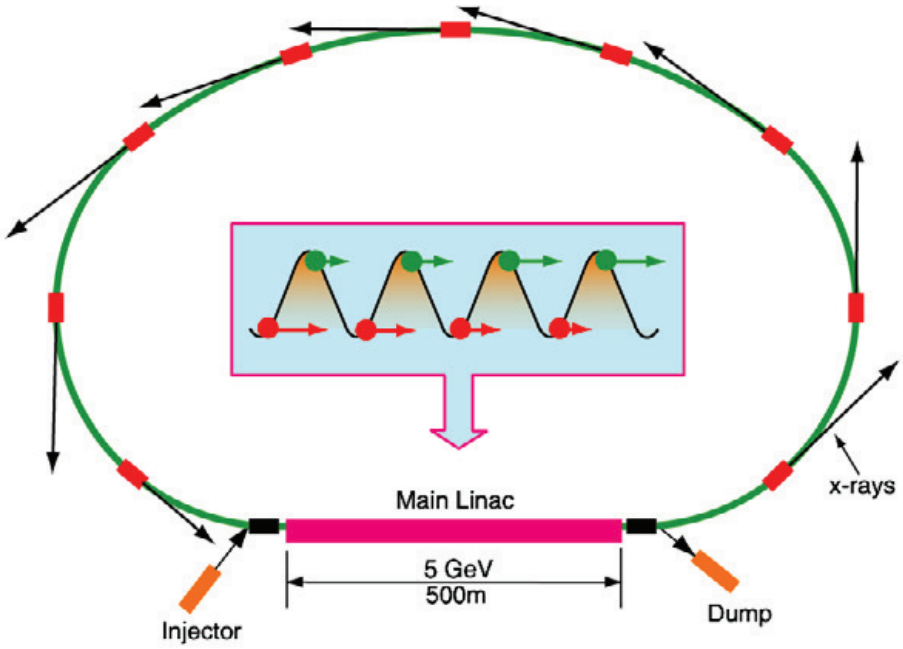

Figure 1.1: The concept of the Cornell ERL. The energy is stored inside the SRF cavities and more than 99% of the energy can be saved. For 5 GeV beam energy, 100 mA beam current, the power consumption is much less than 500 MW. Reproduced from ref. [3].

are accelerated on-crest, and can reuse the energy inside the SRF cavities. Because the electron bunches circulate inside the facility only once (at most several times), they preserve the phase space distribution from the injector and are far away from the equilibrium [5]. The phase space distribution of the injector can be superior, and improvement can be made by upgrading the injector with relatively less cost. Cornell has been a leader in accelerator physics, and became involved in the research of the Cornell ERL, which includes the photoinjector that can deliver high current and ultra-low emittance [3, 4, 5, 7].

The Cornell ERL holds the promise to produce the x-ray light that is hundreds to thousands times brighter than the currently available sources [Fig. 1.2]. Meanwhile, Free Electron Lasers (FELs) have also been developed. One example is the Linac Coherent Light Source (LCLS) at the SLAC National Accelera-

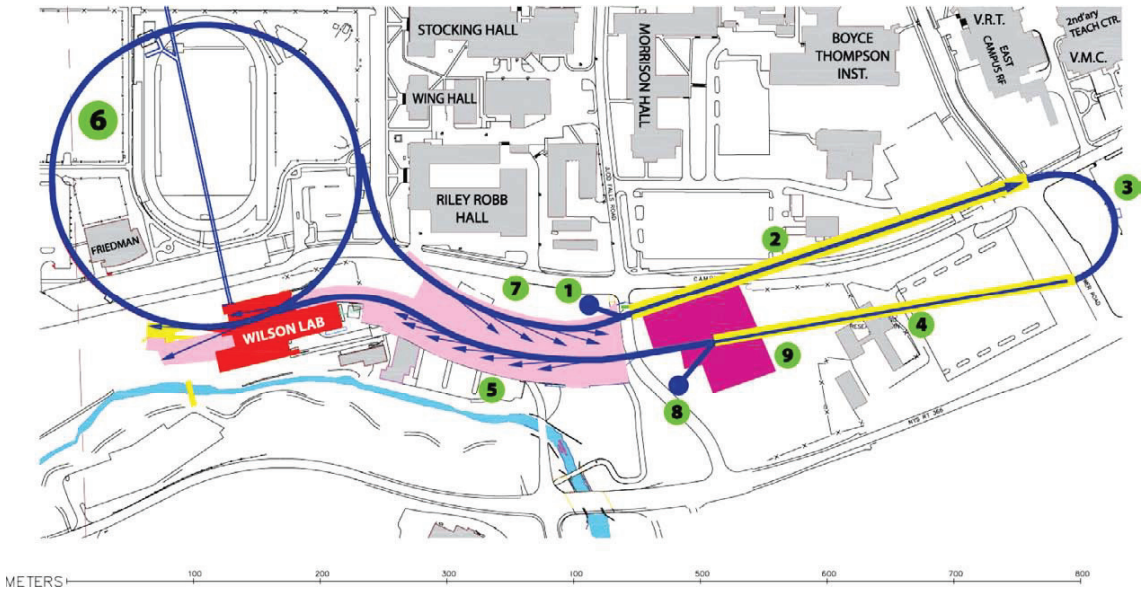

Figure 1.2: The infrastructure plan of the Cornell ERL. It uses the the first linac to accelerate the injected the electron beam to 2.5 GeV, then it circles clockwise to the other linac to reach the 5 GeV beam energy. After that the electron beam circles around the storage ring and produces x-rays at different experiment stations. Reproduced from ref. [3].

tor Laboratory. The peak brightness of FELs is considerably higher, and their repetition rate is a lot lower compared with ERLs; they serve different scientific experiments and are complementary to each other [4, 5, 6]. Although the bunch charges from ERLs are much smaller compared to the FELs, and it is hard to realize the self-amplified stimulated emission, people are also investigating possibilities to implement the FELs in the ERLs because the ERLs are extremely flexible [4, 5, 6].

The LCLS demonstrates the capability of the FELs, with astonishing peak brightness and very short bunch length [9, 10]. The x-ray pulses are so bright that the scattering patterns can be recorded before they destroy the sample[11]. It enables the capability to do pump-probe experiments on the scale smaller

than 100 fs and has tremendous impacts on science and technology nowadays. On the other hand, the ERLs are capable of experiments that require continuous attention from samples and are also much faster for raster experiments when the beam needs to be focused down to less than 100 nm [3, 4, 8].

In accelerator physics, the emittance describes the volume of the phase space. The brightness is inversely proportional to the convolution between the diffraction limited (DL) photon emittance ($\lambda/4\pi$) for a Gaussian mode and the electron emittance. In the hard x-ray regime ($\lambda < 1$Å), the electron emittance is usually larger compared to the DL photon emittance. Thus, the ultra-low emittance is extremely important for the hard x-ray facilities.

In order to produce the ultra-low emittance required by the Cornell ERL, we first need to understand the electron beam properties. The slice emittance measurement was developed to characterize the time-resolved emittance. It is based on the two-slit method and a vertical deflecting Radio Frequency (RF) cavity. It enables the emittance characterization in the time domain. We employed this capability to achieve the smallest emittance that has ever been measured in this photoinjector in 2011. It is a large improvement from the previously recorded 3.6 mm-mrad in 2010 [12]. It gives 0.8 mm-mrad normalized emittance and 0.3 mm-mrad normalized core emittance at 5 MeV beam energy [12]. In the experiments presented in this thesis, the beam energy is limited to 5 MeV mainly because of the safety issues such as the radiation concern and the neutron production threshold. Numerical simulations show that the emittance can be furthermore reduced at higher beam energy especially higher gun voltage. Numeric simulations also show that by optimizing the laser pulse three-dimensional (3D) intensity profile, the emittance can be further reduced

by a factor of two because it can make the uniform ellipsodial electron beam density distribution, where the linear space charge effects can be compensated by the linear optics downstream [13, 14]. Therefore, we developed the method of measuring the 3D laser intensity [15]. We also demonstrated that it can retrieve the temporal phase information [16, 17]. The starting dynamics of the dissipative soliton lasers is also presented as the periphery work for the laser pulse characterizations [18].

This thesis focuses on the generation and characterization of the ultra-low emittance. It begins with the overview of the photoinjector, then it covers the starting dynamics of dissipative Yb-doped soliton fiber lasers. After that it describes the 3D laser pulse intensity characterization and follows with the temporal phase retrieval from the same setup [15, 16, 17]. It follows with the gun and RF cavity voltage calibrations and the related issues in the slice emittance measurement, and later presents the slice emittance measurements at 5 MeV beam energy.

The photoinjector starts with the laser system, which shines light on the photocathode, and generates electrons from the photoelectric effect. These electrons are accelerated by the direct current (DC) gun and pass through the emittance compensation components in the A1 section, then further accelerated to 5 to 15 MeV by the cryomodule in the A2 section, then focused by the quadrupoles in A3 section, and merged into the main linac from the B1 section [Fig. 1.3]. Advanced diagnostics are implemented in order to achieve the high current and ultra-low emittance. We perform the projected and slice emittance measurements in both the A4 and the B1 section. The C2 section has one dipole and a view screen, where the time-resolved energy spread can be measured. The A5

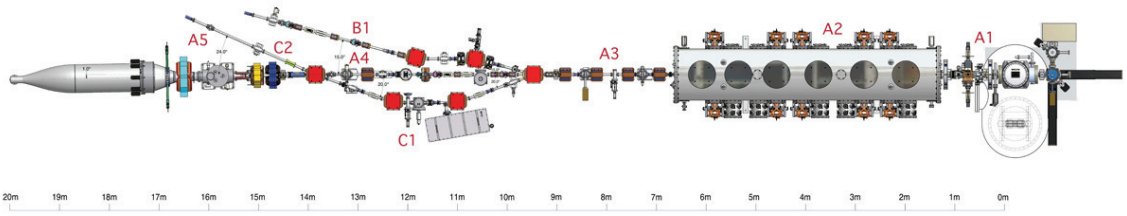

Figure 1.3: The schematic of the Cornell ERL photoinjector. The beam direction is from the right to the left.

section has the dump, and the electrons are dumped there.

1.1 The physics properties

There are several important physics properties that will be mentioned later in this thesis, this section gives their definitions.

1.1.1 Emittance

Let us take the horizontal emittance as an example. There are many particles in the ensemble, each of them has the position (x) and normalized momentum ($x' = \frac{\vec{p}_x}{p_x}$). The sigma matrix of the transverse emittance is defined by [2]

$$\Sigma \equiv \begin{bmatrix} \langle x^2 \rangle & \langle xx' \rangle \\ \langle x'x \rangle & \langle x'^2 \rangle \end{bmatrix} = \epsilon \begin{bmatrix} \beta & -\alpha \\ -\alpha & \gamma \end{bmatrix}, \tag{1.1}$$

where $\langle ... \rangle$ means the ensemble average, $\epsilon = \sqrt{\langle x^2 \rangle \langle x'^2 \rangle - \langle xx' \rangle^2}$ is the emittance, α, β, γ are the Twiss parameters which describe the shape and orientation of the

ellipse,

$$\alpha = -\frac{\langle xx' \rangle}{\epsilon}, \quad \beta = \frac{\langle x^2 \rangle}{\epsilon}, \quad \epsilon = \frac{\langle x'^2 \rangle}{\epsilon}, \tag{1.2}$$

where β is the β-function in accelerator physics, which is equivalent to the Rayleigh range z_R in optics. The emittance ϵ gets smaller as the particles are accelerated, while the normalized emittance ϵ_N remains constant, it is defined as

$$\epsilon_N \equiv \epsilon \times \left(\gamma \frac{v}{c}\right), \tag{1.3}$$

where γ is the Lorentz factor, v is the particle velocity, and c is the speed of light. The thermal emittance is the emittance from the initial electrons generated from the photocathode; it sets the lower limit for normalized emittance that can be achieved from the photoinjector. For a multi-alkali cathode, the mean thermal energy of these electrons is 160 meV, and corresponds to 0.12 mm-mrad normalized emittance for the 1 mm diameter laser beam. This will be discussed in the later parts of this thesis.

The electromagnetic wave also has emittance. In x-ray experiments, the beam is normally focused on the sample. Therefore, its field across the sample can be calculated from the Fraunhofer's diffraction integral. For a Gaussian beam, it is shown that the DL photon emittance is $\lambda/4\pi$, where λ is the wavelength [2]. The DL emittance is the lowest achievable photon emittance.

1.1.2 Brightness

The flux (F) characterizes the strength of radiation per time, per unit bandwidth, it is normally defined as [2]

$$\text{Flux} = \frac{\text{N}_{\text{ph}}}{\text{sec} \cdot 0.1\%\text{bw}}, \tag{1.4}$$

where N_{ph} stands for the photon number and bw stands for the bandwidth.

The brightness is the beam density in the six-dimensional phase space. It is the photon density per unit time, per unit area, per unit solid angle, per unit bandwidth. Its unit is normally defined as this in literatures:

$$\frac{\text{N}_{\text{ph}}}{\text{sec} \cdot \text{mm}^2 \cdot \text{mrad}^2 \cdot 0.1\%\text{bw}}. \tag{1.5}$$

The brightness is an invariant property in statistical physics, which means that the optics cannot improve it [1, 2]. If the photo-distribution obeys the Gaussian distribution, the brightness can be calculated as

$$\text{Brightness} = \frac{F}{4\pi^2 \sigma_{\text{T,x}} \sigma_{\text{T,x'}} \sigma_{\text{T,y}} \sigma_{\text{T,y'}}}, \tag{1.6}$$

where $\sigma_{\text{T,u}}$, $\sigma_{\text{T,u'}}$ are the effective beam size and divergence in the u-axis (u=x,y) [2]. For the Gaussian distribution, $\epsilon_{\text{ph,u}} = \sigma_{\text{T,u}} \sigma_{\text{T,u'}}$. Therefore the Eq. 1.6 can be written as

$$\text{Brightness} = \frac{F}{4\pi^2 \epsilon_{\text{ph,x}} \epsilon_{\text{ph,y}}}. \tag{1.7}$$

When there is no correlation in the electron beam, the brightness of the x-ray is the convolution between a single electron's contribution and the electron's brightness [2]. Assume the radiation from one single electron is DL; we have $\epsilon_{ph,u} = \epsilon_{el,u} \otimes \epsilon_{ph}$ (u=x, y). Where $\epsilon_{el,u}$ is the electron emittance on the u-axis, $\otimes$ stands for the convolution. The brightness can be written as [2]

$$\text{Brightness} = \frac{F}{4\pi^2(\epsilon_{el,x} \otimes \epsilon_{ph})(\epsilon_{el,y} \otimes \epsilon_{ph})}, \tag{1.8}$$

where $\epsilon_{ph} = \lambda/4\pi$ is the DL photon emittance. For hard x-ray sources (λ <0.1 Å), the electron emittance $\epsilon_{el,u}$ is usually several times larger than the DL photon emittance ϵ_{ph}. Therefore, the brightness is inversely proportional to the electron emittance squared, and ultra-low electron emittance is extremely important to achieve the outstanding brightness for the ERLs [5].

1.2 The laser system

The laser system is the very front end; it delivers high-power, stable, shaped laser pulses to the photocathode. In order to achieve the electron beam quality that satisfies the photoinjector design, current photocathode technology limits the light spectrum range from the ultra-violet to the visible wavelength [2]. The fiber laser system fits the requirement of the high repetition rate and high power, while the waveguide properties insure the excellent beam quality. Most of the current state-of-the-art high power and MHz-to-GHz repetition rate fiber laser systems work at 1 μm because of the gain material technology, and they can be frequency doubled to provide green light around 500 nm [19, 20, 21, 22, 23, 24,

25]. We use the Yb-doped fiber laser system. Assuming a 1% quantum efficiency for the photocathode, it requires about 20 nJ pulse energy at 520 nm wavelength to generate 80 pC bunch charge. At 1.3 GHz, it corresponds to 26 W laser power. When counting the beam loss from the shaping and delivering, more than 50 W laser power is required. We have resolved many engineering challenges in the past several years in order to meet the requirement of the Cornell ERL [20, 24].

The pulse propagation equation describes the pulse evolution in fiber lasers and amplifiers, and it can be derived from the Maxwell equations, with the assumption that the spatial and temporal part are decoupled from each other. In the fiber, this assumption is true because of the waveguide properties. The slowly varying amplitude of the pulse is $A(z,T)\exp(i\omega_0 t)$, where ω_0 is the optical carrier frequency, z is the fiber position, and T is the retarded time. In the pulse's moving frame, the pulse propagation equation is [26]:

$$\frac{\partial A}{\partial z}+\frac{\alpha}{2}A+\frac{i\beta_2}{2}\frac{\partial^2 A}{\partial T^2}-\frac{\beta_3}{6}\frac{\partial^3 A}{\partial T^3}=i\gamma(|A|^2A+\frac{i}{\omega_0}\frac{\partial}{\partial T}(|A|^2A)-T_RA\frac{\partial|A|^2}{\partial T}), \tag{1.9}$$

where α is the linear small signal gain, β_2, β_3 are the group velocity dispersion and the third-order dispersion, γ is the nonlinear parameter, T_R is the Raman nonlinear response time, $\gamma(\omega_0)=\frac{n_2(\omega_0)\omega_0}{cA_{\text{eff}}}$ is the nonlinear coefficient, where A_{eff} is the effective area of the fiber. In the picosecond regime, the third order dispersion, the self-steeping, and the Raman effect are not important, and they can be ignored [26]. The Eq. 1.9 can be simplified:

$$i\frac{\partial A}{\partial z}=-i\frac{\alpha}{2}A+\frac{\beta_2}{2}\frac{\partial^2 A}{\partial T^2}-\gamma|A|^2A, \tag{1.10}$$

the gain, the dispersion and the nonlinearity determine the pulse evolution in the fiber. Write $A(z,T) = \sqrt{P_0}\exp(-\alpha z/2)U(z,T)$, where P_0 is the peak power of the pulse. The dispersion length L_D and the nonlinear length L_{NL} are defined as:

$$L_D = \frac{T_0^2}{|\beta_2|}, \qquad\qquad L_{NL} = \frac{1}{\gamma P_0}. \tag{1.11}$$

where T_0 is the pulse duration. The Gaussian shaped pulse will broaden by a factor of $\sqrt{2}$ after propagating a distance L_D, while the nonlinear phase shift increases by 1 after propagating a distance L_{NL}. The nonlinear phase accumulation ϕ_{NL} distorts the pulse shape and generally speaking, it should be avoided in amplifiers. As a rule of thumb, we usually keep the nonlinear phase accumulation ϕ_{NL} below 2π in the amplifiers to maintain high conversion efficiency for the second harmonic generation (SHG), which requires both energy conservation and phase matching (momentum conservation) [25].

We have both 50 MHz and 1.3 GHz laser system for the ERL photoinjector. The 50 MHz system is mainly used for the emittance measurements, because the two-slit emittance measurement system (EMS) can only handle up to hundreds of μA beam current. The 1.3 GHz system is dedicated for high current running and will eventually be used for the entire facility. Both the 50 MHz and 1.3 GHz laser systems have similar temporal laser profile shaping systems to optimize the laser temporal profile, and they share the same spatial laser profile shaping system.

Table 1.1: The 50 MHz laser amplifier parameters

Stage	Pre-amp DPA	Main amplifier
Gain fiber	Yb-501	DC-200/40-PZ-Yb-03
Fiber length	30 cm	200 cm
Core absorption	>125 dB/m @ 915 nm	10 dB/m @ 976 nm
Pulse length	~2.5 ps	~2.5 ps
Input energy	~0.1 nJ	~3 nJ
Output energy	~4 nJ	~100 nJ
Mode field diameter	6±1 μm	30±2 μm
ϕ_{NL}	~0.2	~ 1.5π

1.2.1 The 50 MHz laser system

The 50 MHz laser system constitutes a Yb-doped soliton fiber laser oscillator, a divided pulse amplifier (DPA), the main stage amplifier, a Pockels cell, a SHG crystal, four YVO_4 temporal shaping crystals, and the transportation lenses as shown in Fig. 1.2.1. The amplifier parameters are listed in Table. 1.1. It shares the transverse shaping apparatus with the 1.3 GHz system on the optical table near the gun, that has the beam expander, the spatial shaping iris, the virtual cathode Charge-Coupled Device (CCD) camera.

The Yb-doped soliton fiber laser oscillator has a 1200/mm grating pair inside to provide -4 ps^2 dispersion, so that the laser works in the soliton regime. One end mirror is glued on a piezoelectric element and is used to synchronize the laser with the RF clock. The pulse energy is 0.3 nJ, the bandwidth is 0.7 nm and the pulse duration is 2.5 ps full-width at half maximum (FWHM), its time-bandwidth product is 0.4 and not far away from the transform limited value

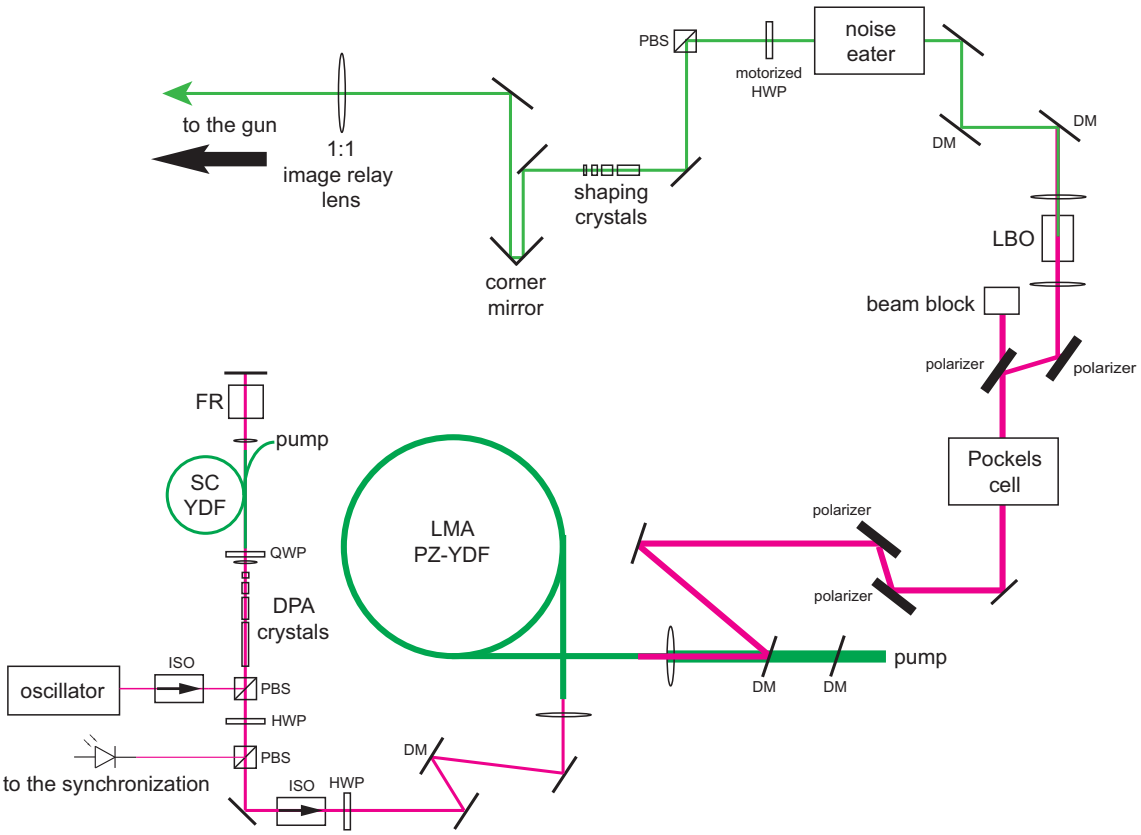

Figure 1.4: The schematic of the 50 MHz laser system. ISO, optical isolator; PBS, polarization beam splitter; DPA, divided pulse amplifier; SC YDF, single-mode Yb-doped fiber; FR, Faraday rotator; HWP, half wave plate; QWP, quarter wave plate; DM, dichroic mirror; LMA PZ-YDF, large-mode-area single-polarization Yb-doped fiber.

0.32. The dispersion length L_D is on the order of 10 m, and it can be ignored in the amplifier stage. The nonlinear phase accumulation is limited by the divided pulse amplifier (DPA) and the large mode area fiber amplifier to be smaller than 2π (Table. 1.1). The DPA is there to ensure a small nonlinear phase shift before the main amplifier, in order to preserve the beam quality. Then these pulses are amplified in the DPA that has four YVO_4 birefringent crystals (57.6 mm, 28.8 mm, 14.4 mm, 7.2 mm) to divide the original pulse to sixteen smaller pulses in order to mitigate the self-phase modulation effect from the nonlinearities; one

quarter-wave plate is also used to lower the nonlinearity by a factor of 1.5 from changing the linear polarization to the circular polarization [26, 27]. The gain fiber (Yb-501) length is 30 cm with pump absorption >125 dB/m at 920 nm. The pulse energy is amplified to 4 nJ after this pre-amplifier. The nonlinear phase accumulation in the DPA is 0.2 and is negligible. The gain fiber for the main amplifier is the large-mode-area single-polarization fiber from NKT photonics, DC-200/40-PZ-Yb-03. The fiber has length 2 m with pump absorption 10 dB/m at 976 nm. These pulses are amplified to 100 nJ. The nonlinear phase accumulation ϕ_{NL} here is 1.5π. These pulses go through two Brewster angle polarizers to clean their polarization before entering the Pockels cell. The Pockels cell changes the polarization of the input pulse train. With one polarizer after, it chops the pulses to macro-pulse for the emittance measurement. The repetition rate of the macro-pulse can be adjusted from hundreds of Hz up to 5 kHz, while the macro-pulse duration can be adjusted from 300 ns to 10 μs. Two Brewster angle polarizers are placed behind the Pockels cell to dump the unwanted power and also to prepare the linear polarization for the SHG. These pulses go through a 15 mm LBO crystal at $178^{\circ}C$ for the noncritical phase match SHG process [25], frequency doubled to 520 nm. The SHG conversion efficiency at 100 nJ is normally 40% [20]. Then these pulses go through four YVO_4 shaping crystals with the crystal lengthes 15.1, 7.55, 3.78, 1.89 mm. At 520 nm, one mm YVO_4 crystal corresponds to 1 ps time delay between the ordinal and the extraordinal pulses, and these pulses are stacked together to produce the near flat-top temporal distribution after passing through these crystals because of the group velocity difference. These pulses are delivered to the gun optical table that is 30 m away from the shaping crystals. Three 1:1 image relay lenses are used for the laser beam transport. The pointing stability just after the main amplifier

is usually less than 1 mrad, however, after 30 m propagation, it corresponds to 3 mm position jitter that are not acceptable for practical experiments. Thus we used three 1:1 image lenses to image relay the point just after the SHG crystal three times before it reaches the optical table near the gun. The pointing stability is improved to hundreds of μm after the image relay system. On the gun table, the beam is magnified by a three-lens telescope which magnifies the beam before an iris and then the laser beam is truncated by this iris to produce the truncated-Gaussian or near-flat-top transverse distribution for the experiments. The image on the iris is imaged onto the photocathode and the virtual cathode CCD camera.

1.2.2 The 1.3 GHz laser system

The 1.3 GHz laser system is described in detail in the ref. [24].

The 1.3 GHz laser system has a commercial laser oscillator from the PriTel company. It is also synchronized with the RF clock. The pulses from the oscillator have a bandwidth 2 nm and pulse duration 8 ps and can be dechirped by a grating pair to 800 fs FWHM. The amplifier parameters are listed in Table. 1.2, the nonlinear phase accumulation after the main amplifier is 0.5π. The optical power from the oscillator is 20 mW and it is amplified by a double-pumped single-mode fiber amplifier to 250 mW, then it goes through a preamplifier, the power increases to 3.5 W. Then the pulses are amplified by the main amplifier to 150 W. These pulses are dechirped by a transmission grating pair to 800 fs. After the compressor, the optical power is 110 W. After dechirping, the pulse width is 890 fs; these pulses are frequency doubled by the same type of 15 mm LBO

Table 1.2: The 1.3 GHz laser amplifier parameters

Stage	Pre-amp 1	Pre-amp 2	Main amplifier
Gain fiber	Yb-164	DC-135/15-PM-Yb	DC-200/40-PZ-Yb-03
Fiber length	300 cm	220 cm	250 cm
Core absorption @ 976 nm	30 dB/m	8 dB/m	10 dB/m
Pulse length	~8 ps	~8 ps	~8 ps
Input energy	~10 pJ	~150 pJ	~2 nJ
Output energy	~200 nJ	~2.7 nJ	~100 nJ
Mode field diameter	6±1 μm	16±1 μm	30±2 μm
ϕ_{NL}	~0.1	~ 0.1	~0.5π

crystal to 65 W optical power at 520 nm wavelength [24].

1.3 The photocathode and the photoemission gun

The photoemission gun can generate electrons with very low emittance and very short bunch length, and the initial bunch shape can be optimized by shaping the initial laser pulse profiles. Cornell has chosen the DC type photoemission gun because of the 1.3 GHz repetition rate and the 100 mA requirements.

Several types of photocathode have been tested at the Cornell ERL. The merits are the high quantum efficiency (QE), the short response time, the low transverse mean emittance, and the long lifetime. It is still one active research area in

the accelerator community [2]. We normally use semiconductor photocathodes because of their high QE.

Let us take GaAs photocathode as one example. It has all the merits mentioned above (except long life time) and has also been widely studied [2]. When a laser pulse hits a GaAs photocathode, valence electrons on the top of the valence band are excited into the conduction band. There are some diffusion processes (electrons collide with the lattice or the phonon), some electrons will go to the surface of the cathode, and escape into the vacuum. One thin layer of Cs is deposited on the surface of the GaAs to produce negative electron affinity, and it makes the photoemission process much more efficient. KCsSb cathodes have also been used. We have demonstrated 50 mA operating current from the GaAs cathode, and are investigating how to extend its lifetime at such a high current [12].

After the electrons are generated from the photocathode, they are accelerated by the gun high voltage (HV). The initial electrons have the thermal emittance, which is the mean transverse energy of the photoelectrons. Because of the Coulomb forces, these electrons repel each other and the emittance grows rapidly. When these electrons are accelerated, in their own moving frame, the repulsive forces are decreased by a factor of γ^2 (γ is the Lorentz factor). So that the higher the electric field, the earlier that the emittance will be frozen. The DC type photoemission gun can provide stable high currents, however, its voltage is limited by the current technology [28]. We normally operate this gun at 350 kV, which corresponds to $\gamma \sim 1.7$. This is several times smaller compared to the RF guns [2], thus it is more challenging to compensate the emittance downstream. The gun HV is 350 kV, which is much lower compared to the 6 MeV

from the RF gun at the LCLS. Because the transverse space charge effect scales with $1/\gamma^2$, therefore, the 0.8 mm-mrad emittance result at 80 pC bunch charge is comparable with the 1.2 mm-mrad at 1.2 nC values from the LCLS [9, 10].

There has been a lot of work on increasing the gun HV, which includes using a ceramic with guarding rings to reduce the field emission and the stress. New guns are being built in the Wilson lab, and the research of using a SRF gun is also underway at many labs.

1.4 The emittance compensation section

When the electron bunch has a uniform ellipsoidal distribution, the space charge (SC) force is linear and the emittance growth can be compensated by the linear optics downstream [29]. We have an emittance compensation section between the gun and the cryomodule. This section contains two solenoids with a bunching cavity (buncher) between them. The first solenoid focuses the electron beam inside the buncher, while the second solenoid focuses the beam inside the first SRF cavity of the cryomodule. The buncher is used to give a negative chirp on the bunch to compensate the longitudinal space charge effect [30].

Without the SC effect, the bunch length is 30 ps FWHM or 8 ps root mean square (rms) when it enters the buncher; while at the full bunch charge 80 pC and 2 mm diameter initial beam size, the bunch length increases to 60 ps FWHM or 20 ps rms. The bunch has a positive energy chirp: the head (tail) part gets accelerated (decelerated) and travels faster (slower). The buncher operates in the bunching mode (-90 degree from the on-crest value), and gives a negative chirp to the bunch to compress the bunch length. The bunch length is compressed to

14 ps rms after the buncher, and can be further compressed by the SRF cavities when they operate closer the bunching phase.

1.5 The SRF cavities

The SRF cavities are inside the cryomodule, where the temperature is 1.8 K. The Cornell ERL photoinjector has five two-cell SRF cavities, each of them can boost the beam energy by several MeV [31, 32]. After the photoinjector, the beam energy can be varied from 5 to 15 MeV. Because of the practical purposes such as the radiation concern and the neutron production threshold, we normally operate at beam energy from 5 to 6 MeV.

1.6 Beam diagnostics

We have advanced beam diagnostics in order to monitor the beam properties and also for the research purposes. We have the spectrometer to measure the beam energy, the beam position monitors (BPMs) to measure the beam position, the Faraday cup to measure the beam current, and also the two-slit emittance measurement system (EMS) to measure the transverse beam emittance.

1.6.1 Beam position monitors

The beam position monitor (BPM) has specially designed antennas and can pick up the signal from the electron bunches traveling through them. When an elec-

tron bunch passes through the BPM, it generates current intensity. By analyzing the current data, we can get the beam position, the bunch arrival time and the bunch charge. It is widely used in the Cornell ERL and can monitor the beam operation in real-time [2].

1.6.2 Spectrometer

The electron beam is bent in the C2 section of the photoinjector by the dipole magnet. It hits a view screen downstream the dipole. The energy spread can be measured on the view screen. With the deflecting cavity turned on, time-resolved energy spread can be measured. By inserting the vertical and horizontal slits in the A4 section, we can measure the energy spread at a particular phase space point. We compare the measured time-resolved energy spread with simulation to gain insight of the beam dynamics.

1.6.3 Bunch charge measurement

We measure the bunch charge in several different ways. The current reading from the gun gives the most accurate reading, however, it needs sufficient current (tens of mA). The Faraday cup collects the current from of the electron beam and the bunch charge can be calculated straightforwardly:

$$q = \frac{\bar{I}}{DF \cdot f_0}, \tag{1.12}$$

where $\bar{I}$ is the average current measured by the Faraday cup, DF is the duty factor, f_0 is the repetition rate of the drive laser. The BPM intensity can also measure the bunch charge after it is calibrated by the other methods.

1.6.4 Emittance measurement systems

There are several ways to measure the projected emittance. One of them is to scan a quadrupole magnet and reconstruct the emittance using tomography [2], however, it does not work well when the transverse SC effect dominates the emittance growth. We use the two-slit method to measure the projected beam emittance [2]. We use magnet corrector pairs to move the beam transversely, and a slit to sample the beam. Effectively, the first slit selects the transverse position of the phase space while the second slit selects the transverse momentum of the phase space, as illustrated in Fig. 1.5. By scanning the two magnet corrector pairs, we can scan the entire phase space and reconstruct the project emittance [2]. In our experiment, the charge is collected in a Faraday cup connected to a fast charge-to-voltage amplifier, and a 100×100 point phase space scan can be done within 10 seconds. This capability enables the real-time transverse projected emittance optimization in experiments. When we replace the Faraday cup with a defecting cavity and a view screen, we can measure the time-resolved slice emittance, which will be discussed later in one chapter of this thesis.

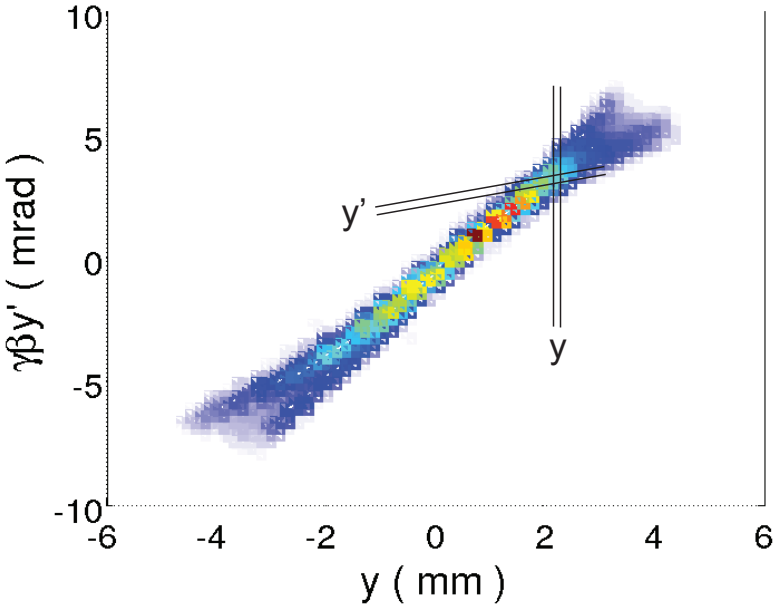

Figure 1.5: The measured vertical emittance phase space distribution.

BIBLIOGRAPHY

[1] X-Ray Data Booklet, http://xdb.lbl.gov/, (2009).

[2] A. W. Chao, and M. Tigner, "Handbook of Accelerator Physics and Engineering", World Scientific, (2009).

[3] D. H. Bilderback, J. D Brock, D. S. Dale, K. D. Finkelstein, M. A. Pfeifer, and S. M. Gruner, "Energy recovery linac (ERL) coherent hard x-ray sources", New Journal of Physics, 12, 035011 (2010).

[4] D. H. Bilderback, P. Elleaume, and E. Weckert, "Review of third and next generation synchrotron light sources", J. Phys. B: At. Mol. Opt. Phys. **38**, S773-S797 (2005).

[5] S. M. Gruner, D. Bilderback, I. Bazarov, K. Finkelstein, G. Krafft, L. Merminga, H. Padamsee, Q. Shen, C. Sinclair, and M. Tigner, "Energy recovery linacs as synchrotron radiation sources (invited)", Rev. Sci. Instrum. **73**, 1402 (2002).

[6] S. Benson, M. Borlandb, D.R. Douglasa, D. Dowellc, C. Hernandez-Garciaa, D. Kayrand, G.A. Kraffta, R. Leggf, E. Moogb, T. Obinag, R. Rimmera, V. Yakimenkod, "X-ray sources by energy recovered linacs and their needed R&D", Nucl. Instrum. Meth. A 637 (2011).

[7] G. R. Neil, C. L. Bohn, S. V. Benson, G. Biallas, D. Douglas, H. F. Dylla, R. Evans, J. Fugitt, A. Grippo, J. Gubeli, R. Hill, K. Jordan, R. Li, L. Merminga, P. Piot, J. Preble, M. Shinn, T. Siggins, R. Walker, and B. Yunn, "Sustained Kilowatt Lasing in a Free-Electron Laser with Same-Cell Energy Recovery", Phys. Rev. Lett. **84**, 662 (2000).

[8] Q. Shen, I. Bazarov, and P. Thibault, "Diffractive imaging of nonperiodic materials with future coherent X-ray sources", J. Synchrotron Radiat. **11**, 432 (2004).

[9] R. Akre, D. Dowell, P. Emma, J. Frisch, S. Gilevich, G. Hays, Ph. Hering, R. Iverson, C. Limborg-Deprey, H. Loos, A. Miahnahri, J. Schmerge, J. Turner, J. Welch, W. White, and J. Wu, "Commissioning the Linac Coherent Light Source injector", Phys. Rev. ST Accel. Beams **11**, 030703 (2008).

[10] Y. Ding, A. Brachmann, F.-J. Decker, D. Dowell, P. Emma, J. Frisch, S. Gilevich, G. Hays, Ph. Hering, Z. Huang, R. Iverson, H. Loos, A. Miahnahri,

H.-D. Nuhn, D. Ratner, J. Turner, J. Welch, W. White, and J. Wu, "Measurements and Simulations of Ultralow Emittance and Ultrashort Electron Beams in the Linac Coherent Light Source", Phys. Rev. Lett. **102**, 254801 (2009).

[11] H. N. Chapman, et al., "Femtosecond X-ray protein nanocrystallography", Nature **470**, 7377 (2011).

[12] Cornell ERL Elog, https://webdb.lepp.cornell.edu/elog/ERL+L0/.

[13] Y. Li, and J. W. Lewellen, "Generating a Quasiellipsoidal Electron Beam by 3D Laser-Pulse Shaping", Phys. Rev. Lett. **100**, 074801 (2008).

[14] I. V. Bazarov and C. K. Sinclair, "Multivariate optimization of a high brightness dc gun photoinjector", Phys. Rev. ST Accel. Beams **8**, 034202 (2005).

[15] H. Li, I. V. Bazarov, B. M. Dunham, F. W. Wise, "Three-dimensional laser pulse intensity diagnostic for photoinjectors", Phys. Rev. ST Accel. Beams 14, 112802 (2011).

[16] H. Li, Z. Zhao, I. V. Bazarov, B. M. Dunham, and F. W. Wise, "Direct optical phase retrieval from a three-dimensional interferometer", accepted by Conference on Lasers and Electro-Optics (CLEO) 2012.

[17] H. Li, C. Wan, A. Chong, and F. W. Wise, "Three-dimensional intensity and temporal phase measurement of the Airy-Bessel wave packet", submitted to Frontiers in Optics (FiO) 2012.

[18] H. Li, D. G. Ouzounov, and F. W. Wise, "Starting dynamics of dissipative-soliton fiber laser", Opt. Lett. **35**, 2403-2405 (2010).

[19] D. J. Richardson, J. Nilsson, and W. A. Clarkson, "High power fiber lasers: current status and future perspectives [Invited]", JOSA B, **27**, B63 (2010).

[20] D. Ouzounov, H. Li, B. Dunham, and F. W. Wise, "Fiber-based drive laser systems for the Cornell ERL electron photoinjector", Proc. SPIE 7581, 75810N (2010).

[21] F. Ö. Ilday, J. Buckley, W. Clark, and F. W. Wise, "Self-similar evolution of parabolic pulses in a laser", Phys. Rev. Lett. **92**, 213902 (2004).

[22] A. Chong, J. Buckley, W. Renninger, and F. W. Wise, "All-normal-dispersion femtosecond fiber laser," Opt. Express, **14**, 10095 (2006).

[23] S. Lefrancois, T. S. Sosnowski, C.-H. Liu, A. Galvanauskas, and F. W. Wise. "Energy scaling of mode-locked fiber lasers with chirally-coupled core fiber". Opt. Express **19**, 3464-3470 (2011).

[24] Z. Zhao, B. M. Dunham, I. Bazarov, and F. W. Wise, "Generation of 110 W infrared and 65 W green power from a 1.3-GHz sub-picosecond fiber amplifier", Opt. Express, **20**, 4850 (2012).

[25] R. W. Boyd, "Nonlinear Optics", Academic Press, second edition, 2003.

[26] G. P. Agrawal, "Nonlinear Fiber Optics", Academic Press, fourth edition, 2007.

[27] L. J. Kong, L. M. Zhao, S. Lefrancois, D. G. Ouzounov, C. X. Yang, and F. W. Wise, "Generation of megawatt peak power picosecond pulses from a divided-pulse fiber amplifier", Opt. Lett. **37**, 253-255 (2012).

[28] B. M. Dunham, C. K. Sinclair, I. V. Bazarov, Y. Li, X. Liu, and K. W. Smolenski; "Performance of a Very High Voltage Photoemission Electron Gun for a High Brightness, High Average Current ERL Injector", Proceedings of the 2007 Particle Accelerator Conference, IEEE 1-4244-0917-9, 1224-1226 (2007).

[29] B.E. Carlsten, "New photoelectric injector design for the Los Alamos National Laboratory", Nucl. Instrum. Meth. A **285** 313-319 (1989).

[30] K. J. Kim, "Rf and space-charge effects in laser-driven rf electron guns", Nucl. Instrum. Meth. A **275**, 201-218 (1989).

[31] V. Medjidzade, M. Liepe, S. Belomestnykh, S.Belomestnykh, R.L. Geng, H. Padamsee, V. Shemelin, and V. Veserevich, "Design of the CW Cornell ERL Injector Cryomodule", in Proc.of 2005 Particle Accelerator Conference, Knoxville, TN, (2005).

[32] V. Veshcherevich, S. Belomestnykh, M. Liepe, V. Medijidzade, H. Padamsee, V. Shemelin, N. Sobenin, A. Zavadtsev, "Design of High Power Input Coupler for Cornell ERL Injector Cavities", 12th International Workshop of RF Superconductivity, Cornell University (SRF, July 10-15, 2005).

CHAPTER 2

THE STARTING DYNAMICS OF DISSIPATIVE-SOLITON FIBER LASERS

The starting dynamics of an all-normal-dispersion Yb-doped fiber laser are studied experimentally and compared to an existing stochastic model of starting from quantum noise. The laser reaches mode-locking 10 to 100 times faster than a soliton laser with similar parameters. According to the model, the fast starting can be attributed to the large pulse energy in the normal-dispersion laser. We also report direct observations of starting from relaxation oscillations and discuss that process in light of the theory.

Originally published as H. Li, D. G. Ouzounov, and F. W. Wise, Opt. Lett. **35**, 2403 (2010).

2.1 Introduction

The field of ultrafast science and technology depends on the availability of sources of ultrafast pulses, and this has motivated extensive studies of pulse evolution in mode-locked lasers. The phase-locking of a large number of longitudinal cavity modes is a fascinating process, and the self-starting is an important practical attribute of a mode-locked laser. Quite a few studies of the starting dynamics of mode-locked lasers have been reported [1, 2, 3, 4, 5, 6, 7, 8, 9, 10, 11, 12, 13, 14, 15, 16]. To date, all work on starting dynamics has addressed lasers with anomalous cavity group-velocity dispersion (GVD) and soliton-like pulse shaping. These studies have considered solid-state lasers and Er-doped fiber lasers.

A number of models have been proposed to explain the observed threshold power for the mode-locking, and these tend to focus on the competition between phase-locking and decoherence processes [2, 3, 4, 5, 6, 7, 9, 10, 13]. Recently, Gordon *et al*. developed a stochastic theory of the onset of mode-locking, in which starting is viewed as a noise-induced escape over an entropic barrier, and mode-locking constitutes a thermodynamic phase transition [15, 16]. This model indicates that quantum noise initiates the pulsation, and the free-running cavity modes are coupled together by the saturable-absorber nonlinearity. The group-velocity dispersion (GVD), which is crucial to the steady mode-locked state, is not a factor in the starting dynamics.

Normal-dispersion femtosecond lasers, in which pulses are dissipative solitons, have demonstrated major performance advantages [17, 18]. Here we report a study of the starting dynamics of an all-normal-dispersion (ANDi) fiber laser. The stochastic theory accounts for the starting dynamics under some conditions, although the starting times are ~10 times faster than in soliton lasers owing to higher pulse energies. In addition, we directly observe the influence of relaxation oscillations on the starting, which can speed up the starting process by another order of magnitude.

2.2 The starting dynamics of Yb-doped soliton fiber lasers

The starting dynamics of an Yb-doped soliton fiber laser were measured as a control experiment. The laser is described in [19], and the fiber lengths and grating pair were chosen for net cavity GVD of -0.18 ps^2. Nonlinear polarization evolution acts as the saturable absorber. The repetition rate is 46 MHz and

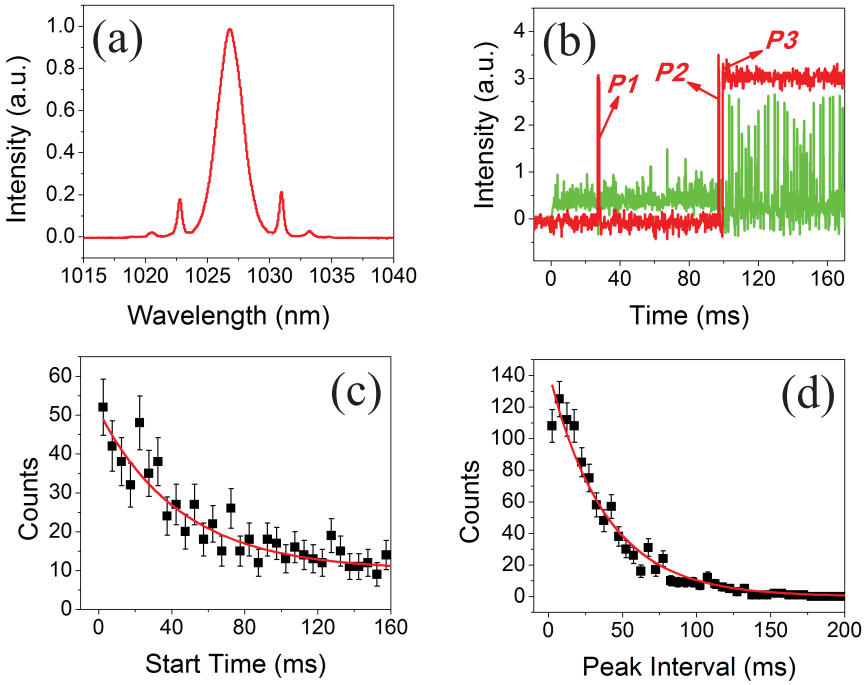

Figure 2.1: Results from soliton laser. a) spectrum, b) pulse energy and 2-photon absorption traces. Green: pulse energy, red: peak intensity. c) start time histogram and exponential fit, d) peak fluctuation interval histogram and exponential fit. The peak intervals are the time intervals between peaks P1, P2 and P3 in Fig. 1(b). Peak positions are defined as where the peaks start.

the intra-cavity pulse energy is 0.6 nJ. With these parameters, the laser operates in the soliton regime [Fig. 2.1(a)]. The pulse is transform-limited, with 700 fs duration, and 0.4 nJ output energy. A mechanical chopper is placed inside the cavity. An InGaAs detector is used to monitor the pulse energy, and a GaAsP photodiode, which only detects 1-μm light through 2-photon absorption, monitors the peak intensity.

Typical measured traces are shown in Fig. 2.1(b). We define the zero of time as when the cavity mode is first completely unblocked by the chopper wheel. Aliasing produces structure in the pulse energy trace (green), but it does not

interfere with the analysis, because we are only interested in the position when the trace rises above the noise floor. The starting time is defined as when the laser reaches the mode-locked state as indicated by a stable 2-photon current level. Fluctuations in the peak power (red) are observed before the onset of mode-locking. The distribution of time intervals between peak fluctuations can help unveil the origin of fluctuations. We recorded thousands of pulse energy and peak intensity traces, and analyzed their statistical properties.

The results are similar to those of prior measurements of soliton lasers [1, 2, 3, 4, 5, 6, 7, 8, 9, 10, 11, 12, 13, 14, 15, 16]. The start times exhibit an exponential distribution [Fig. 2.1(c)], which implies that the fluctuations are domintated by quantum noise [16]. The peak fluctuation time intervals also obey the exponential distribution [Fig. 2.1(d)], which indicates that the peak fluctuation birth rate is constant in time, another signature of quantum noise. The average start time is 100 ms, close to the results in [16].

2.3 The starting dynamics of Yb-doped dissipative soliton fiber lasers

The normal-dispersion regime is accessed by removing the grating pair from the laser and adding a filter; the setup is otherwise unchanged. The resulting GVD is 0.08 ps^2 and the repetition rate is 52 MHz. The spectrum [Fig. 2.2(a)] exhibits the steep sides and cat-ear structure of dissipative-soliton formation. The chirped output pulse is 10 ps in duration, and can be dechirped to 200 fs, near the transform limit. The pulse energy ranges from 3 to 5 nJ, depending on the pump power. Example traces of the pulse energy and peak power are

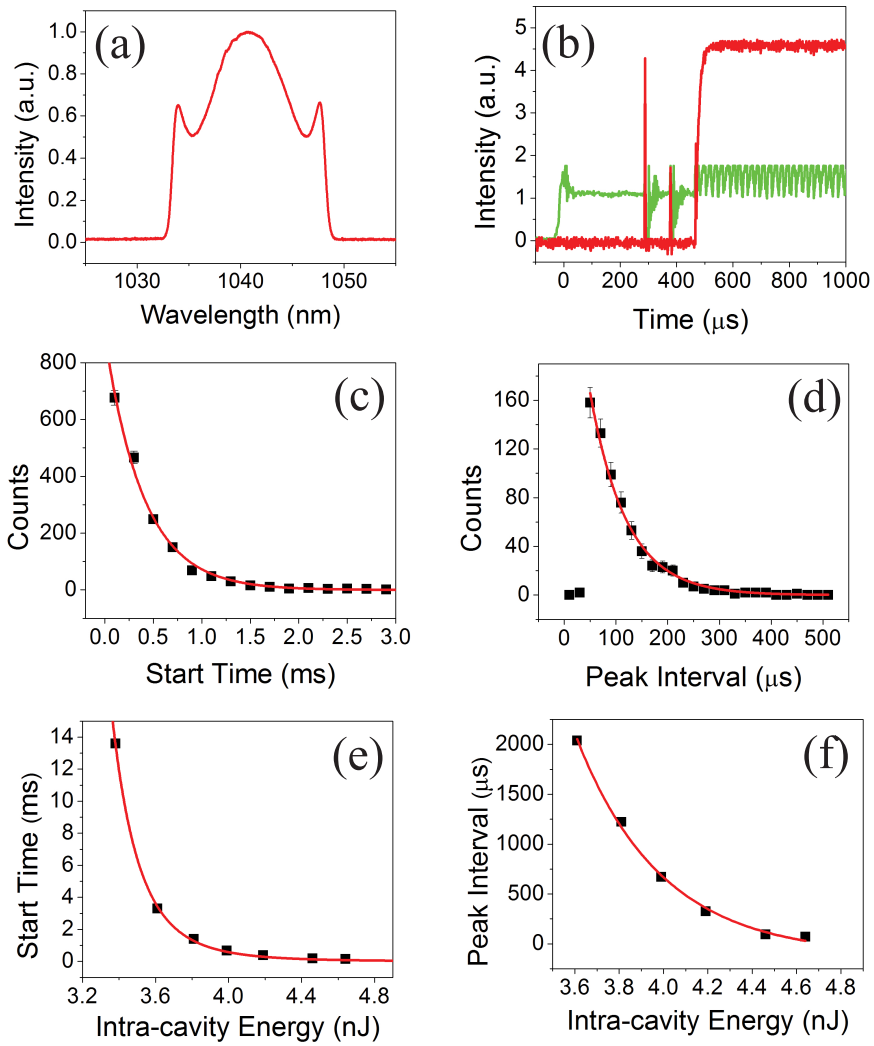

Figure 2.2: Results from ANDi laser. a) spectrum, b) pulse energy and 2-photon absorption traces. c) start time histogram and exponential fit, d) peak interval histogram and exponential fit, e) intra-cavity energy vs. start time, fitted by model in [16], f) intra-cavity energy vs. peak interval and exponential fit.

shown in Fig. 2.2(b). Peak intensity fluctuations occur before the mode-locked state is reached, as in the soliton case. In the ANDi laser, short-lived pulsations occur after each peak fluctuation, but fail to reach the steady mode-locked state.

Although the pulse evolution in the ANDi laser is very different from soli-

ton evolution, the distributions of the start times and fluctuation intervals [Figs. 2.2(c, d)] are exponential and again indicate the dominant role of quantum noise. However, the start times range from 140 μs to 14 ms, which is an order of magnitude shorter than the start times in the soliton laser. The start time varies rapidly with the intra-cavity pulse energy [Fig. 2.2(e)], as predicted by the stochastic model [16]. The fluctuation interval ranges from 70 μs to 2 ms and exhibits an analogous dependence on pulse energy. Higher cavity energy produces a higher peak fluctuation birth rate, and in turn a shorter starting time.

Starting dynamics in soliton and dissipative-soliton lasers are similar (although with distinct time scales) because dispersion and the refractive nonlinearity have little impact on the initial pulse formation. When mode-locking is starting, fluctuations occur on the scale of mode-beating: hundreds of picoseconds to nanoseconds. Thus only the saturable absorber nonlinearity couples free-running cavity modes. These conditions are consistent with the assumptions of the stochastic model [16], and it accounts well for the experimental observations.

Sources of noise other than quantum noise can contribute to the initial fluctuations. In the course of these experiments, we configured the ANDi laser to operate with increased output coupling. The spectrum [Fig. 2.3(a)] is essentially unchanged, and the pulse duration is unchanged. Under these conditions, the pulse energy and peak power undergo regular and periodic variations [Fig. 2.3(b)], in contrast to the random fluctuations presented above. The peaks have instrument-limited duration of 1 μs. The peak interval distribution [Fig. 2.3(c)] is localized around 70 μs, and its width decreases with increasing pulse energy. The distributions of peak positions and starting times overlap

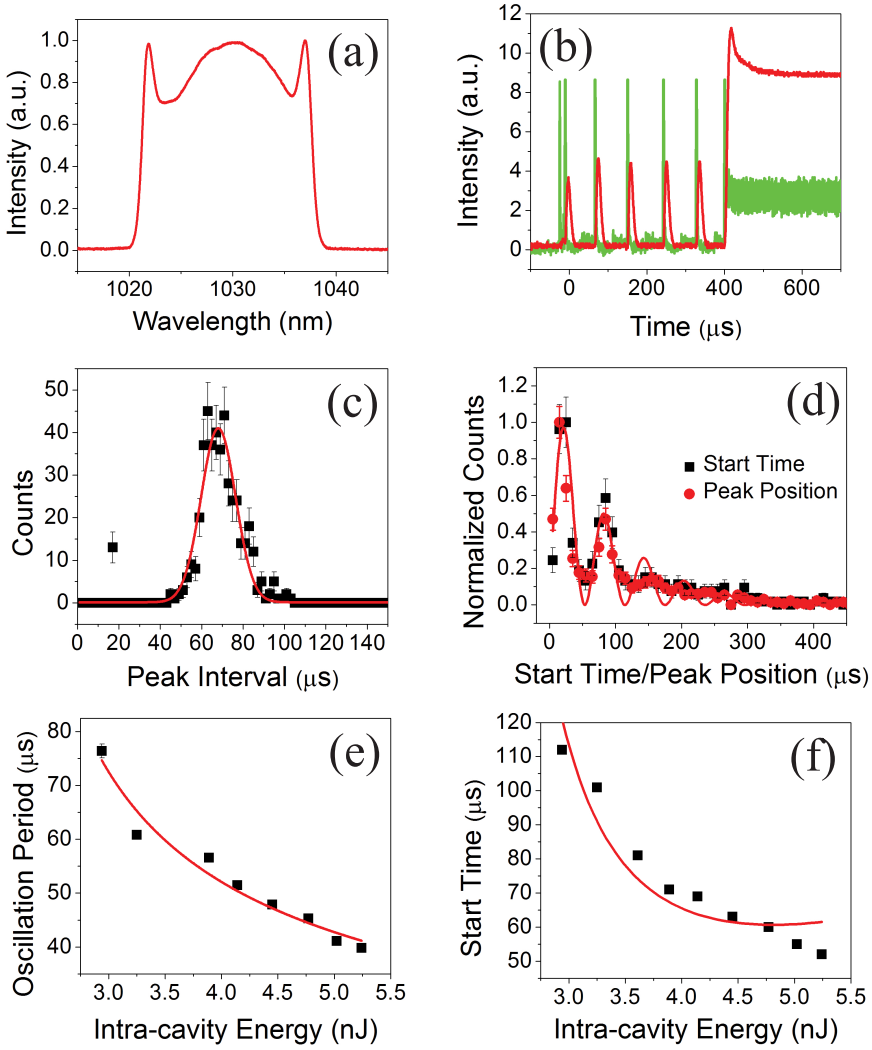

Figure 2.3: Results that show relaxation oscillations. a) spectrum, b) pulse energy and 2-photon absorption traces, c) peak interval histogram and Gaussian fit, d) start time and peak position histograms, and best-fit exponentially-decaying sinusoid, e) intra-cavity energy vs. oscillation period. Symbols are measured and line is model of [20], with parameters $K \sim 10^{-3}$, $N \sim 5\times10^{8}$, γ_c ~10 to 50 ns^{-1}, γ_2 ~2.3 ms^{-1} for each cavity mode, r ~2 to 20, [20], f)intra-cavity energy vs. start time and best-fit model in [16].

substantially [Fig. 2.3(d)], so starting is clearly correlated with the strong pulsation.

The parameters of the Yb fiber lasers studied here imply that relaxation oscillations should occur with periods of 40 to 80 μs and damping times of 10 to 150 ms. The period of observed pulsations is plotted *versus* the pulse energy in Fig. 2.3(e) along with the values calculated from a standard model of relaxation oscillations [20]. The good agreement supports the assignment to relaxation oscillations.

Remarkably, we are unable to find any previous literature report of the role of relaxation oscillations in starting of mode-locking. The relaxation oscillation facilitates the starting; the laser reaches the steady mode-locked states within 200 μs, or less than three periods [Figs. 2.3(c, d)]. The starting time is around 100 μs with 3 nJ energy, and decreases to around 50 μs at 5 nJ energy, much faster than when the fluctuations are random. The relaxation oscillations are more likely to occur with higher intra-cavity energy; no relaxation oscillations are observed when the energy is below 1 nJ. Beyond that, we are unable to state specific conditions or a procedure that is certain to produce the relaxation oscillations. Mode-locked states that appear to be identical from the standard diagnostics (pulse energy, spectrum, autocorrelation) may or may not exhibit relaxation oscillations in the starting process. We conjecture that initial conditions of the atom and the field parameters may determine why one noise source dominates a starting event. Perhaps accurate measurements of the noise spectrum [21] will be able to shed light on this. The influence of relaxation oscillations (or more generally, of gain and loss dynamics) on steady-state mode-locking stability is well-known, and typically observed as sidebands in the radio-frequency spec-

trum. Even when the starting dynamics exhibit the relaxation oscillations as in Fig. 2.3(b), we fail to observe them in the steady-state spectrum, which means that they are attenuated by at least 70 dB relative to the mode-locked peak.

In all the cases presented here, the overall structure of the starting time distribution is exponential, which is a feature of the first-order escape process [16]. It can be viewed as a trial-and-success process. Whenever there are intensity fluctuations of any origin, the system tries to reach the steady mode-locked state until it succeeds. Thus, the starting time distribution in all cases is exponential, but the fluctuation source can add some features to the distribution, such as in Fig. 2.3(d), when relaxation oscillation dominates. The stochastic model does not accurately predict the dependence of starting time on pulse energy [Fig. 2.3(f)], presumably because it does not consider deterministic sources of fluctuations.

2.4 Conclusions

In conclusion, we have studied the starting of mode-locking in an all-normal-dispersion fiber laser. A stochastic theory of the mode-locking transition accounts well for the experiments when the starting is from quantum noise. The laser starts 10-100 times faster than soliton lasers, owing to higher pulse energies. This rapid starting may be valuable to some applications of these lasers. We also observe starting from relaxation oscillations, apparently for the first time. Starting is closely correlated to relaxation oscillations when they occur, and the starting time decreases significantly compared to starting from quantum noise. Future work will address why quantum noise or relaxation oscilla-

tions control the starting, along with any connections to the steady-state noise spectrum.

2.5 Acknowledgements

Portion of this work were supported by the National Science Foundation (ECS-0701680 and PHY-0131508) and the National Institutes of Health (EB002019).

BIBLIOGRAPHY

[1] E. P. Ippen, L. Y. Liu, and H. A. Haus, "Self-starting condition for additive-pulse mode-locked lasers", Opt. Lett. **15**, 183 (1990).

[2] F. Krausz, M. E. Fermann, T. Brabec, P. F. Curley, M. Hofer, M. Ober, C. Spielmann, E. Wintner, and A. J. Schmidt, "Femtosecond Solid-State Lasers", IEEE, J. of Quantum Electron. **28**, 2097 (1992).

[3] C. J. Chen, P. K. A. Wai and C. R. Menyuk, "Self-starting of passively mode-locked lasers with fast saturable absorbers", Opt. Lett. **20**, 350 (1995).

[4] F. Krausz, T. Brabec and Ch. Spielmann, "Self-starting passive mode-locking", Opt. Lett. **16**, 235 (1991).

[5] Y.-F. Chou, J. Wang, H.-H. Liu, and N.-P. Kuo, "Measurements of the self-starting threshold of Kerr-lens mode-locking lasers", Opt. Lett. **19**, 566 (1994).

[6] Ch. Spielman, F. Krausz, T. Brabec, E. Wintner and A. J. Schmidt, "Experimental study of additive-pulse mode locking in an Nd:Glass laser", IEEE J. Quantum Electron. **27**, 1207 (1991).

[7] F. Krausz and T. Brabec, "Passive mode-locking in standing-wave laser resonators", Opt. Lett. **18**, 888 (1993).

[8] J. Hermann, "Starting dynamic, self-starting condition and mode-locking threshold in passive, coupled-cavity or Kerr-lens mode locked solid-state lasers", Opt. Comm. **98**, 111 (1993).

[9] A. K. Komarov, K. P. Komarov and F. M. Mitschke, "Phase-modulation bistability and threshold self-start of laser passive mode-locking", Phys. Rev. A. **65**, 053803 (2002).

[10] J. M. Soto-Crespo, N. Akhmediev and G. Town, "Continuous-wave versus pulse regime in a passively mode-locked laser with a fast saturable absorber", J. Opt. Am. B, **19**, 234 (2002)

[11] R. Roy, A. W. Yu and S. Zhu, "Quantum Fluctuations, Pump Noise, and the Growth of Laser Radiation", Phys. Rev. Lett, **55**, 2794 (1985).

[12] J. A. R. Williams, P. M. W. French, and J. R. Taylor, "An investigation into femtosecond pulse formation in a continuously-pumped passively-mode-locked CPM ring dye laser", IEEE, J. of Quantum Electron., **26**, 1434 (1990).

[13] J. Goodberlet, J. Wang, and J. G. Fujimoto, and P. A. Schulz, "Starting dynamics of additive-pulse mode locking in the Ti:$A1_2O_3$ laser" Opt. Lett., **15**, 1300 (1990).

[14] D. Abraham, R. Nagar, V. Mikhelahsvili, and G. Eisenstein, "Transient Dynamics in Self Starting Passively Mode Locked Fiber Based Soliton Laser", Appl. Phys. Lett. **63**, 2857 (1993).

[15] Vodonos, A. Bekker, V. Smulakovsky, A. Gordon, O. Gat, N. K. Berger, and B. Fischer, "Experimental study of the stochastic nature of the pulsation self-starting process in passive mode locking", Opt. Lett. **30**, 2787, (2004).

[16] A. Gordon, O. Gat, B. Fischer, and F. Kärtner, "Self-starting of passive mode locking", Opt. Exp. **14**, 11142, (2006).

[17] F. W. Wise, A. Chong, and W. H. Renninger, "High-energy femtosecond fiber lasers based on pulse propagation at normal dispersion", Laser & Photonics Rev., **2**, 58 (2008).

[18] W. H. Renninger, A. Chong, and F. W. Wise, "Dissipative solitons in normal-dispersion fiber lasers", Phys. Rev. A **77**, 023814 (2008).

[19] H. Lim, F. Ö. Ilday, F. W. Wise, "Generation of 2-nJ pulses from a femtosecond ytterbium fiber laser", Opt. Lett. **28**, 660 (2003).

[20] A. E. Siegman, Lasers, Oxford University Press, 1986.

[21] I. L. Budunoğlu, C. Ülgüdür, B. Oktem, F. Ö. Ilday, "Intensity noise of mode-locked fiber lasers", Opt. Lett. **34**, 2516 (2009).

CHAPTER 3

THE THREE-DIMENSIONAL LASER PULSE INTENSITY DIAGNOSTIC

Minimizing the electron beam emittance of photoinjectors is an important task for maximizing the brightness of the next-generation x-ray facilities, such as free electron lasers and energy recovery linacs. Optimally-shaped laser pulses can significantly reduce emittance. A reliable diagnostic for the laser pulse intensity is required for this purpose. We demonstrate measurement of three-dimensional spatiotemporal intensity profiles, with spatial resolution of 20 μm and temporal resolution of 130 fs. The capability is illustrated by measurements of stacked soliton pulses and pulses from a dissipative-soliton laser.

Originally published as H. Li, I. V. Bazarov, B. M. Dunham, and F. W. Wise, Phys. Rev. ST Accel. Beams **14**, 112802 (2011).

3.1 Introduction

Next-generation x-ray facilities, such as free-electron lasers (FELs) and energy recovery linacs (ERLs), produce high brightness x-ray beams from diffraction-limited electron beams. The initial electron beam properties determine the performance of the entire facility, which makes the development of low-emittance electron sources a priority [1]. The beam emittance is a result of the interplay of several phenomena, and depends on a number of factors such as the pulse shape of the photoinjector drive laser [2], the three-dimensional (3D) nature of space-charge forces inside the bunch, the boundary conditions near the photocathode [3], the fields in the radio-frequency (RF) linac cavities, and the aberra-

tions of the electron optics in the gun and downstream. Achieving an ideal 3D electron-beam shape is a matter of active research in the accelerator community: a uniform ellipsoidal beam is the optimal shape when considering linear space-charge forces in free space [4], while a cylindrical shape is known to produce small emittances and is a practical solution pursued in several laboratories [5, 6]. However, the optimum intensity profile in a real system generally requires more complicated shapes to achieve the lowest emittance [7]. To experimentally study the effects of the laser shape on beam performance in photoinjectors, a reliable 3D laser pulse intensity diagnostic is required.

Most existing pulse/beam diagnostics measure the field in the space and time domains separately. Second-order autocorrelation is one of the more traditional techniques in the laser field; being simple in its implementation, it, however, can only provide limited temporal and phase information [8]. Frequency-resolved optical gating (FROG) and its successors give both the temporal intensity and phase information, through the spectrogram of the sum frequency generated by the original laser pulse [9]. FROG employs an iterative phase-retrieval algorithm, which works well for most applications. Spectral phase interferometry for direct electric-field reconstruction (SPIDER) technique can also measure the optical field (both the amplitude and phase) by use of a spectral shearing interferometer [10]. Both of these are established techniques for characterization of the full electric field of a light pulse. Typically, a charge-coupled device (CCD) camera is used to display the (time-integrated) transverse intensity profile. While measuring the spatial and time domains separately suffices for many practical cases, the flexibility of the electron generation mechanism in photoinjectors calls for a more general diagnostic capable of providing direct 3D intensity information for the laser pulses incident on the cathode. The

phase information is not necessary because the photocathode is not sensitive to the phase. Two-dimensional (2D) spatiotemporal field diagnostics have been developed [12, 11, 13, 14] and 3D diagnostics have also achieved limited success [15, 16, 17]. Recently, Li *et al*. developed a simple scheme to measure the 3D laser pulse intensity [18, 19, 20], which is essentially a first order noncollinear cross-correlation with a CCD camera as a detector. The proof-of-principle experiment has been performed in [18, 19, 20], but a number of questions remain regarding the method's limitations and capabilities. As a first-order autocorrelation technique, it cannot be sensitive to the phase; would a cross-correlation between a transform limited (TL) pulse and the unknown pulse yield more information than an autocorrelation, which washes out all the phase information? What sets the accuracy of the method? Can the method be verified using other techniques and in what cases does it serve as a reliable 3D laser shape diagnostic? What role does data processing play in arriving at the intensity profiles and how can one improve the data analysis? The present work presents a ready-to-use data analysis toolkit and explores the method's capability in a number of controlled experiments, confirming the accuracy and the practicality of this technique. A quantitative comparison between the measured results and theoretical predictions is presented. The limitations of the method are discussed as well.

We begin with a brief survey of the existing 3D laser pulse diagnostics and follow with the implementation of the 3D intensity measurement. Then we present the measurements of stacked soliton pulses, which offer one practical solution for minimization of electron beam emittance in photoinjectors [6]. We further illustrate the capability of the 3D diagnostic by measuring the pulse from an all-normal dispersion (ANDi) fiber laser [21], which has a complicated tem-

poral shape. We conclude with a discussion of the limitations of this technique and the outlook for future development.

3.2 Spatiotemporal diagnostics

Although diagnostics of the temporal pulse shape are well-developed, 3D spatiotemporal laser diagnostics have had limited success, in part because of the challenges in their implementation. Unlike the temporal field, which can be mapped to some equivalent 1-dimensional representation (such as the spectrum in the frequency domain or intensity in the time domain), or a 2-dimensional representation (such as the spectrogram) and easily measured, the 3-dimensional field can only be accessed by brute force. Thus, the majority of the methods are based on autocorrelation or cross-correlation with an appropriately prepared probe pulse. Di Trapani *et al*. suggested a cross-correlation scheme to image short optical pulses based on non-collinear sum frequency generation (SFG); it offers new capabilities to measure the 3D intensity, but the finite bandwidth of the mixing crystal and the noncollinear mixing process limit its spatiotemporal resolution and require extensive data interpretation [15]. Trebino *et al*. developed a technique based on nonlinear spectral interferometry and in particular demonstrated measurement of a pulse at a focus [16]. Trebino and co-workers also demonstrated full 3-dimensional intensity and phase information from a single hologram, in which two pulses are cross-correlated through a specially made diffractive optical element [17], although the time resolution is limited and the setup is highly specialized. Finally, Li *et al*. presented a generic method based on noncollinear first order cross-correlation [18, 19, 20], whose implementation is simple and which is suitable for measurement of a

large variety of pulses. As a 3D diagnostic, its accuracy and limitations need to be further investigated. We present this systematic study in a number of controlled experiments.

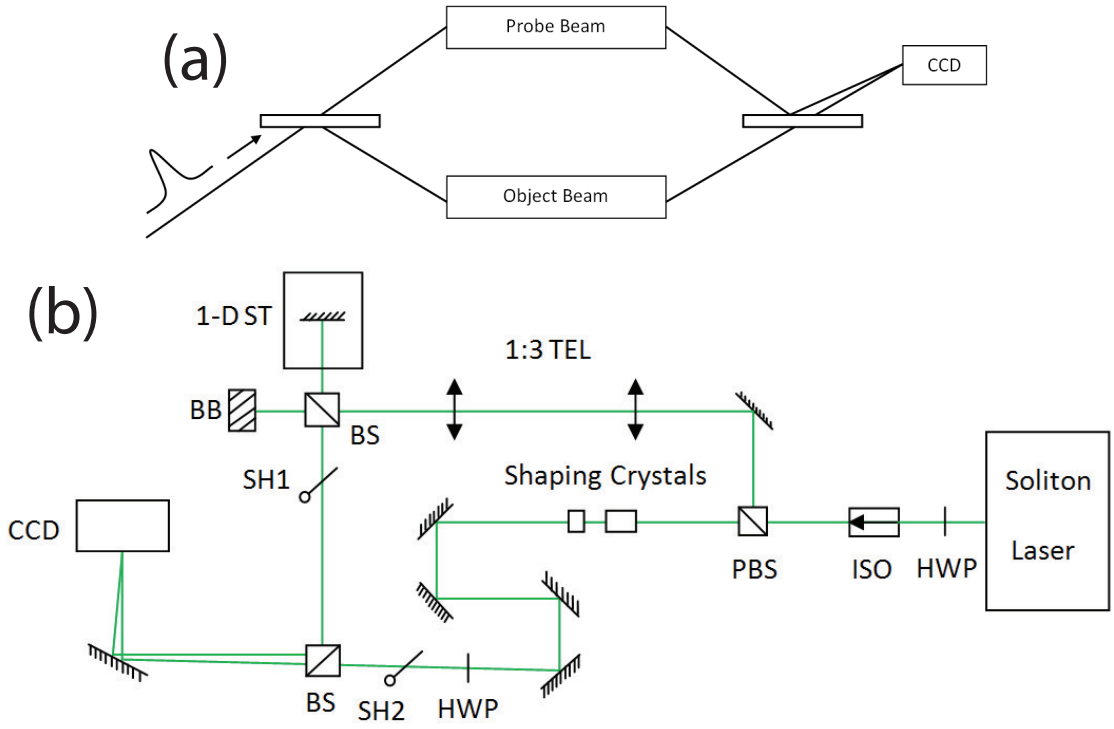

Figure 3.1: a) Conceptual and b) schematic implementation of the diagnostic. (a) the initial beam is split to the probe beam and object beam, with adjustable time delays, then they are combined with a small angle on the CCD camera. (b) the experimental setup to measure stacked soliton pulses. ISO, isolator; HWP, half wave plate; PBS, polarization beam splitter; TEL, telescope; BS, beam splitter; BB, beam block; 1-D ST, motorized one dimensional stage; SH1, shutter 1; SH2, shutter 2; CCD, CCD camera.

3.3 Method and implementation

This method is essentially a noncollinear first order cross-correlation, as illustrated by Fig. 3.1(a). The pulse under investigation (object pulse) is split into

two beams to produce a probe pulse. Ideally, the probe beam should be the transform-limited (TL) version of the original pulse, which was the case in our experiment. These two pulses are combined at a small angle and then detected by a CCD camera. The angle between these two beams is chosen so that the interference fringe spatial period is small but resolvable on the CCD camera. The time delay between the probe and object pulses is adjusted by an optical delay line, and the CCD camera records the time integrated intensity (fluence) $I(\vec{r},\tau)$ as a function of the time delay τ [20] (we refer to this quantity simply as intensity for the rest of the paper):

$$\begin{aligned} I(\vec{r},\tau) &= \int dt|A_o(\vec{r},t)\exp(i\phi_o(t)+i\vec{k_o}\cdot\vec{r}-i\omega_0 t) \\ &+ A_p(\vec{r},t-\tau)\exp(i\phi_p(t-\tau)+i\vec{k_p}\cdot\vec{r}-i\omega_0(t-\tau))|^2 \\ &= I_o(\vec{r})+I_p(\vec{r})+2\cos\{\omega[\tau+\delta(\vec{r})]\} \\ &\quad\times\int dt A_o(t,\vec{r})A_p^*[t-\delta(\vec{r})-\tau,\vec{r}] \\ &\quad\times\cos\{\phi_o(t)-\phi_p[t-\delta(\vec{r})-\tau]\}. \end{aligned} \tag{3.1}$$

$A(\vec{r},t)$ and $\phi(\vec{r},t)$ are the slowly-varying amplitude and phase of the pulse; the subscripts o and p denote the object and probe pulses respectively. $I_o(\vec{r})$ and $I_p(\vec{r})$ are the intensities of the object beam and the probe beam separately, with the coupling term representing the interference between them. When the probe pulse is short compared to the object pulse, Eq. (3.1) can be simplified by applying the δ function approximation, then we obtain the same formula as in [20],

$$I(\vec{r},\tau)\approx I_o(\vec{r})+I_p(\vec{r})+2\cos\omega[\tau+\delta(\vec{r})]\times\sqrt{\Delta t_p i_o(\tau,\vec{r})}\sqrt{I_p(\vec{r})}. \tag{3.2}$$

Δt_p is the duration of the probe pulse, and $i_o(\tau, r)$ is the object pulse intensity at different time delays. The δ function approximation neglects temporal broadening from the cross-correlation, as expected. On the other hand, the effect of cross-correlation on the phase is more complicated and will be discussed further below. The object pulse intensity at time τ can be retrieved from [20]

$$i_o(\tau, \vec{r}) \propto C^2(\tau, \vec{r})/I_p(\vec{r}) \text{ [20]}. \tag{3.3}$$

Here $C(\tau, r)$ is the amplitude of the coupling term in Eq. (3.3); it corresponds to the spatial modulation depth of the interference pattern.

The probe and object beams are combined at an angle for practical reasons. If they overlap perfectly with each other, the time delay line will be sensitive to less than a quarter wavelength; considering the moving part of the delay line and mechanical vibrations in the lab, this configuration is overly sensitive and may produce artifacts that would degrade both the temporal and spatial resolutions. With a small angle between the beams, the ambient noise shifts the phase of the fringes but not the envelope [20]. A larger angle corresponds to finer spatial fringes, and finer resolution. In our experiments, the angle is 0.05 rad, which produces fringes with 20 μm period at 1 μm wavelength. These are resolved by the CCD camera, which has pixel size 4.4×4.4 μm. Thus, our spatial resolution is 20 μm.

The modulation depth $C(\tau, \vec{r})$ should be measured with good fidelity, and this creates several practical considerations for the choice of the CCD camera. Generally speaking, a low-noise and high dynamic-range CCD camera is preferred. The thermal noise from the CCD camera is a known issue; without cool-

ing, the thermal noise from the CCD camera cannot be ignored, and with lower optical intensity increased Poisson noise will appear in the pulse intensity as in Eq. (3.3). The contrast ratio $C(\tau, \vec{r})$ can be very small for the peripheral part of a pulse; increasing $A_p(t, \vec{r})$ increases the contrast ratio, which improves the signal-to-noise ratio achieved by the CCD camera. Practically, the beam spatial intensity distribution is usually a Gaussian, and magnifying the beam by two to three times will serve this purpose. We magnified the probe beam by three times in our experiment.

According to Eq. (3.2), at each time delay we need to know the intensities of the object beam, the probe beam, and the coupling term. Thus we record the beam profiles of the object beam ($img_o(\vec{r}, \tau)$), the probe beam ($img_p(\vec{r}, \tau)$) and the overlapping beam ($img_i(\vec{r}, \tau)$) at each time delay. By applying Eq. (3.3), we can retrieve the object pulse intensity at each time delay.

The envelope of the spatial modulation gives the contrast ratio $C(\vec{r}, \tau)$, while the fine spatial modulation depends on the angle between the object and probe beams. In order to extract the contrast ratio envelope from the interference pattern, we need to take the absolute value of the spatial modulation, and then filter out these modulations with a low-pass filter in the spatial frequency domain:

$$G(\omega) = \sqrt{\frac{1}{1 + (\frac{\omega}{\omega_0})^{2N}}}. \tag{3.4}$$

We use a Butterworth filter (Eq. (3.4)), which has a flat response in the pass band and thus introduces little distortion to the contrast envelope. In our experiment, we set N=8; the bandpass frequency ω_0 is determined by minimizing the probe pulse distortion before and after filtering. After filtering, we inverse

Fourier transform the filtered spatial frequency back to the space domain to obtain the contrast ratio envelope at a given time delay($C^F(\tau, \vec{r})$). We also filter the intensity of the probe beam to make the data processing consistent. This can be expressed as

$$C^F(\tau, \vec{r}) = \text{IFFT2[Filter[FFT2[ABS}(img_i - img_o - img_p(\vec{r}, \tau))]]], \tag{3.5}$$

$$i_o(\tau, \vec{r}) \propto |C^F(\tau, \vec{r})|^2 / I_p^F(\vec{r}). \tag{3.6}$$

Here the notations ABS, FFT2 and IFFT2 refer to absolute value, two-dimensional fast Fourier transform and inverse two-dimensional fast Fourier transform. The superscript F denotes the filtered results.

Whenever a filter is used in data processing, systematic error is introduced. Because of the low-pass nature of the filter, beam profiles with sharp edges can be smoothed out. In our experiment, all the spatial shapes are essentially Gaussian, so that this was not an issue. But for other profiles such as a flat-top, or a high-order super-Gaussian, more optimized filtering may present an advantage. The process is repeated for each intensity slice at a given time delay and their combination provides the 3D laser pulse intensity.

We illustrate the method and its capabilities by performing 3D pulse characterization from two different laser systems. The first is a stack of soliton pulses, which is being used at the Cornell ERL photoinjector [2, 6]. The second is the measurement of the pulse directly from an all-normal-dispersion (ANDi) fiber laser [21], which displays salient temporal features that allows for quantitative comparison with the known pulse shape.

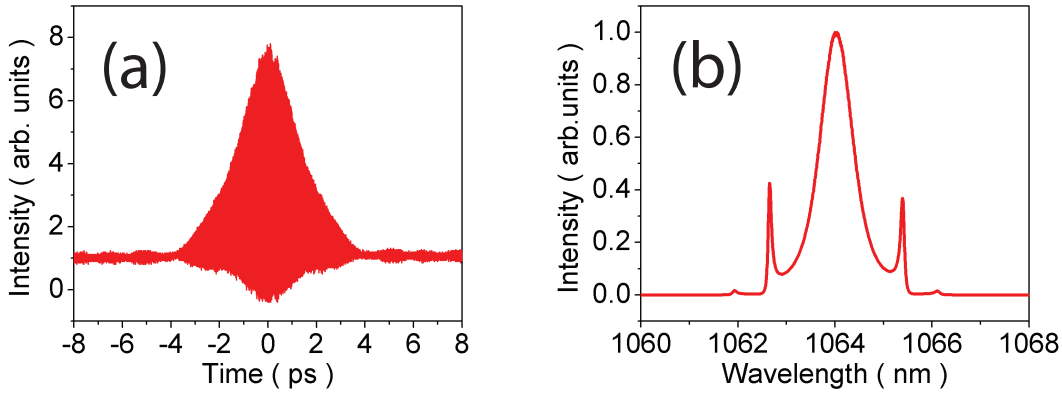

Figure 3.2: The soliton laser characterization. (a) the second-order autocorrelation; (b) the spectrum.

3.4 Measurement of stacked soliton pulses

The experimental setup is depicted in Fig. 3.1(b). It is composed of the soliton laser and the diagnostics. Soliton pulse evolution happens in the anomalous group velocity dispersion (GVD) regime, where the phases accumulated from the nonlinearity and the dispersion cancel each other exactly; this evolution can also happen when the laser cavity has segments of normal and anomalous GVD and net negative GVD. We constructed a soliton laser from a Yb-doped fiber system. A grating pair inside the cavity provides -4 ps^2 GVD, while the fiber dispersion is only around +0.08 ps^2, so that the laser operates in the soliton region. The second-order autocorrelation is shown in Fig. 3.2, and the spectrum exhibits sidebands that correspond to dispersive waves. The full-width at half-maximum (fwhm) pulse duration and spectral bandwidth are around 2 ps and 0.7 nm, respectively; these give a time-bandwidth product of 0.4, which is close to the TL value of 0.32. After producing these pulses, we stacked them together to produce a longer cylinder-likes pulse [22].

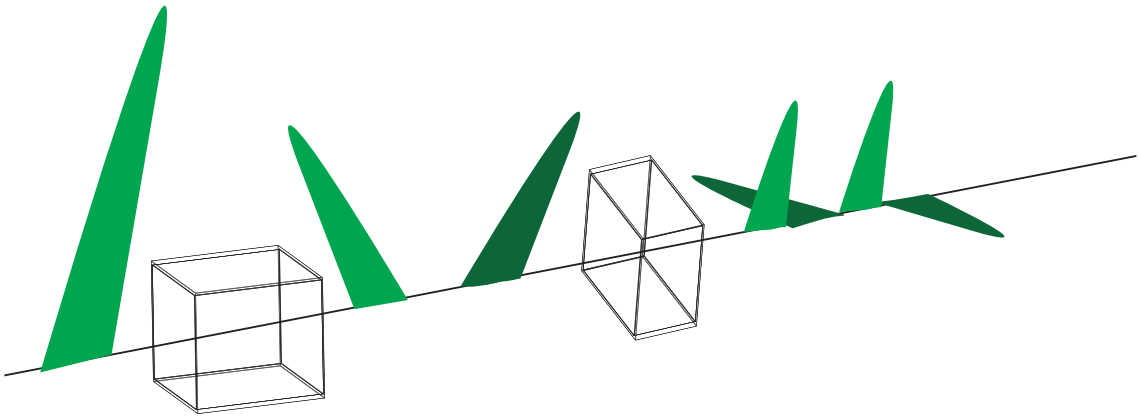

Figure 3.3: Passive beam shaping by two YVO_4 birefringent crystals. Their optical axes are oriented at 45° to each other. By varying this angle, more complicated pulses can be produced in the time domain.

After the pulses are generated from the soliton laser, the beam is split into the object and probe beams [Fig. 3.1(b)]. The object beam passes through two birefringent crystals that are configured to produce four replicas of linear vertical and horizontal polarization, as in Fig. 3.3. Two *a*-cut YVO_4 crystals with lengths 3.4 mm and 6.8 mm are configured with optical axes 45° to each other and the laser beam strikes with polarization 45° to the optical axis of the first crystal. The ordinary (*o*) and extraordinary (*e*) pulse are separated inside the birefringent crystal because of their group velocity mismatch; a 1-mm YVO_4 crystal causes ~0.8-ps delay between the *o* pulse and *e* pulse at 1 μm wavelength. Because the polarization is 45° with respect to the optical axis, the *o* and *e* pulse have the same amplitude. After passing through these two crystals, four replica pulses with equal amplitude are produced, and together they stack to a longer pulse, with nearly flat-top distribution in the time domain [6, 22, 23]. As mentioned before, to reduce the error from the retrieval process, the probe beam is magnified by a 1:3 telescope. A one-dimensional motorized stage with 50-nm precision (PI M-112.12S) serves as the optical delay line; the time delay is set

with 130-fs precision which defines the time resolution. The shutters 1 and 2 in Fig. 3.1(b) are used to select the probe, object, and overlapping beams separately. The shaped pulse has two orthogonal linear polarization, and they are detected separately. The half wave plate (HWP) rotates the polarization of the shaped beam, so that only one polarization projects on the probe beam and contributes to the signal on the CCD camera, while the other polarization is orthogonal to the probe beam polarization, and does not produce a signal. A 14-bit CCD camera (Spiricon GRAS20) serves as the detector, which has spatial resolution 4.4 μm. The data acquisition process precedes the data analysis and both are fully-automated in MATLAB - collection of 200 data points in the time domain with image resolution 1600×1200 (each file is ~1.9 MB) at each slice takes about 10 minutes. After applying Eq. (3.3) to retrieve the object beam intensity, the 3D intensity information is obtained; the data analysis takes around 60 minutes on a quad-core processor with four threads running simultaneously, and it can be further parallelized if more processors are available.

Some sample raw data are shown in Fig. 3.4. The probe beam is magnified by ~3 times [Fig. 3.4(a)] compared to the object beam [Fig. 3.4(b)], so only the center part with adequate intensity overlaps the object beam. When they overlap each other in the time domain, spatial modulations are produced as seen in Fig. 3.4(c, d). When the time delay is large, very little spatial modulation is observed [Fig. 3.4(e, f)]. The envelope of the spatial modulation changes and reflects the pulse intensity profile at each time delay.

Fig. 3.5(a) shows the absolute spatial modulation envelope of Fig. 3.4(c). Its spatial frequency spectrum is depicted in Fig. 3.5(c). The sidebands correspond to the modulation fringes, and the dynamic range is ~10^4, which is limited by

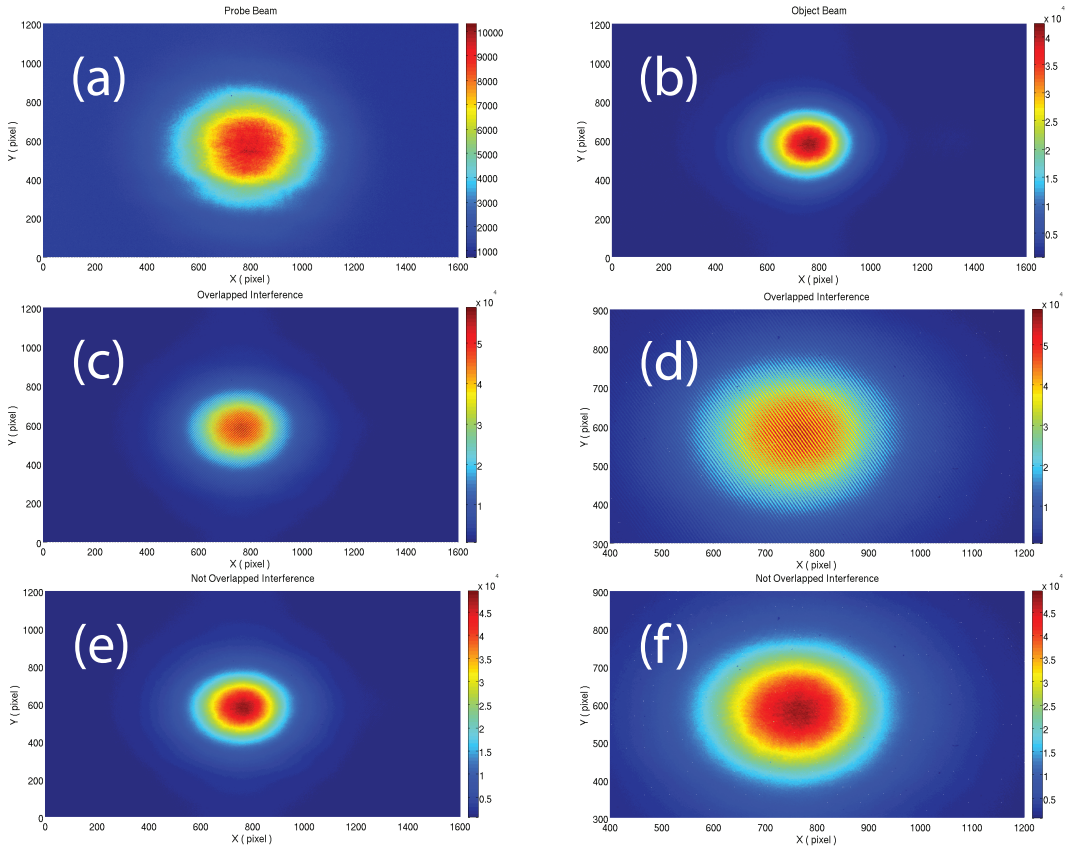

Figure 3.4: The raw data for the stacked soliton case. (a) the probe beam(img_p); (b) the object beam (img_o); (c) the overlapping of the probe and object beam when they overlap in the time domain (the interference, img_i^1). (d) zoomed in image of (c). (e) the overlapping of the probe and object beam when they do not overlap in the time domain (the interference, img_i^2). (f) zoomed in image of (e).

the dynamic range of the CCD camera. After applying the low-pass Butterworth filter, the sidebands are suppressed by a factor of ~10^{20} [Fig. 3.5(d)] and the inverse Fourier transform gives the absolute envelope of the contrast ratio. The object pulse intensity at a given time delay is reconstructed by applying Eq. (3.3).

By repeating this process at each time delay, slices of the 3D object pulse intensity are collected; combining them, we can get the 3D intensity of the object

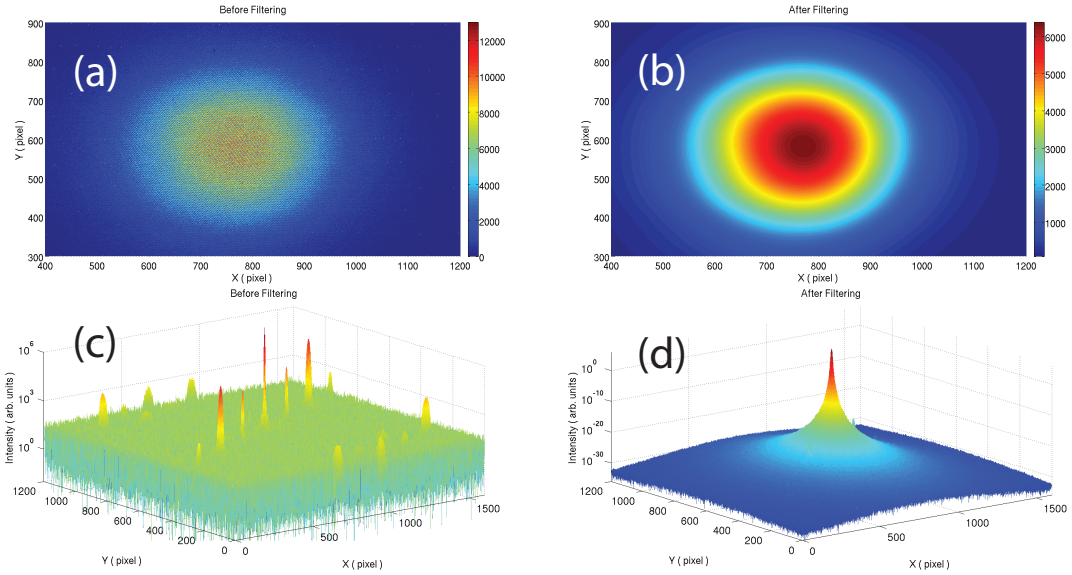

Figure 3.5: The spatial filter. (a) the image before filtering, $ABS(img_i^1 - img_p - img_o)$; (b) the image after filtering; (c) the log scale spatial frequency of (a) before filtering; (d) the log scale spatial frequency intensity of (b), after filtering.

beam, as shown in the iso-intensity surfaces plot [Fig. 3.6(b)], where the false color represents different light intensities. The temporal intensity is obtained by integrating the pulse intensity at each time delay, as shown in Fig. 3.6(a), where we can see the four nearly equal peaks of the stacked soliton pulses. Each polarization has two peaks and these peaks are separated by ~3 ps with each other, as expected; their width is ~2.2 ps which is sightly larger than the 2 ps interferometric autocorrelation measurement, because of the broadening from the cross-correlation. The non-zero intensity values between these peaks come from elliptically-polarized light, which can come from the misalignment of the birefringent shaping crystals as well as the cutting angle error(±0.5°). To verify the result in the spatial domain, we compared the total intensity from the retrieval to the signal on the CCD camera, as shown in Fig. 3.7.

The time-integrated intensity of the object beam on the CCD camera

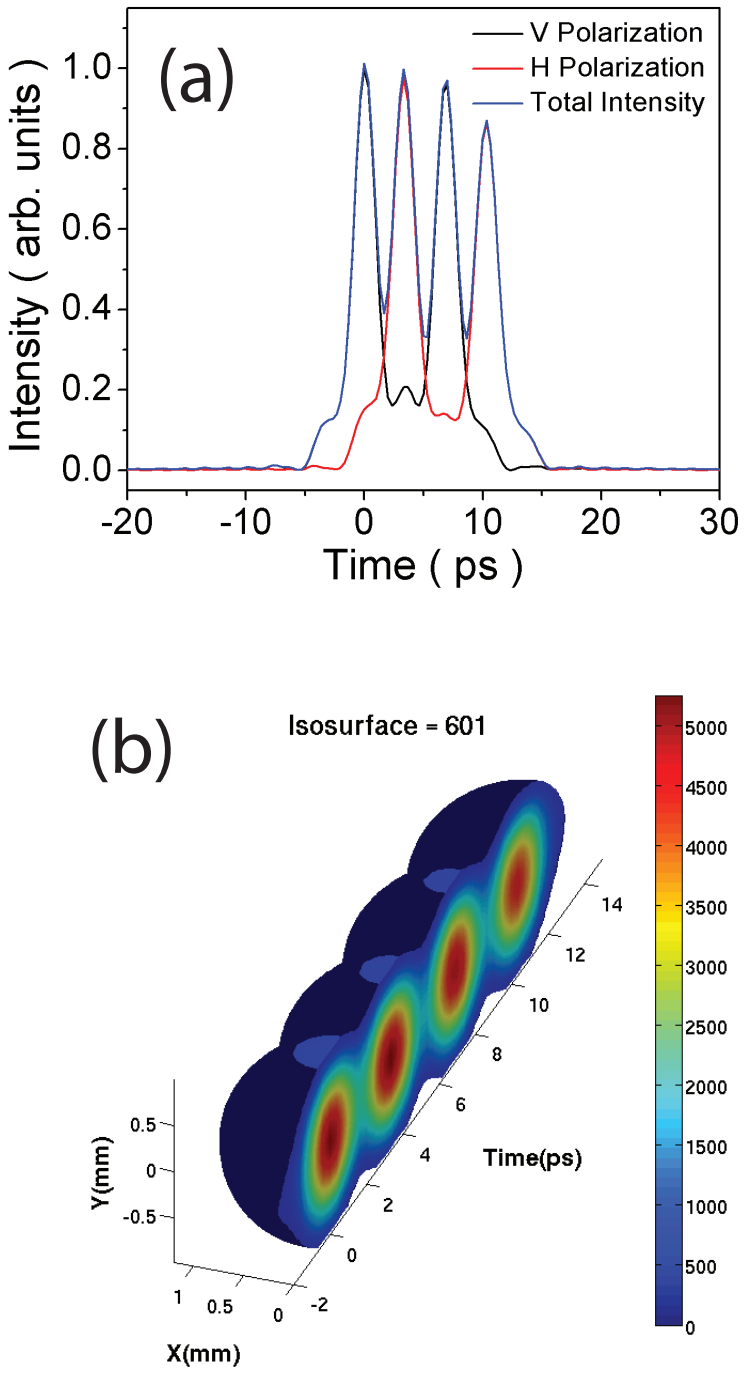

Figure 3.6: Results of measurement of stacked soliton pulses. (a) the temporal intensity distribution obtained by cross-correlation; (b) the 3-dimensional intensity distribution, plotted as iso-intensity surfaces.

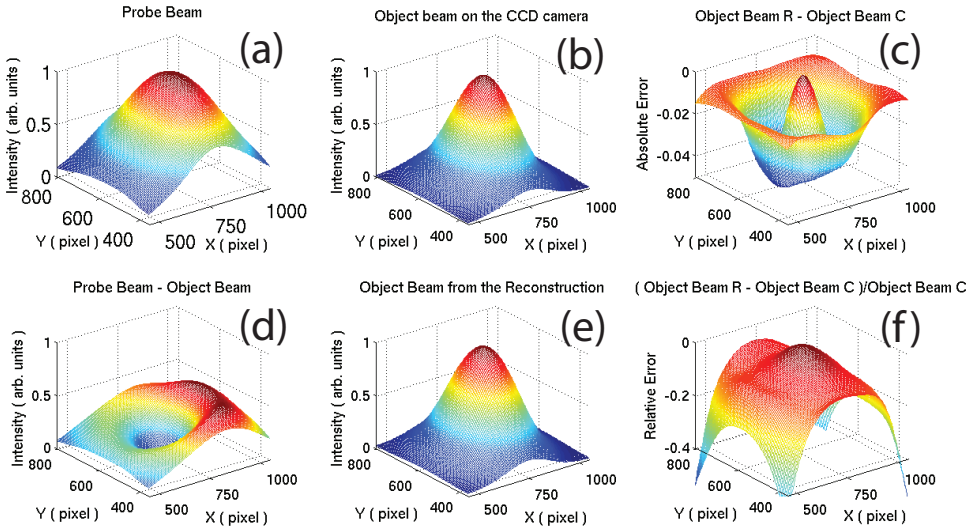

Figure 3.7: The stacked soliton pulses intensity profile. (a) the normalized probe beam intensity; (b) the object beam intensity on the CCD camera; (c) the object beam intensity difference between the retrieval process and the intensity on the CCD camera; (d) the probe beam intensity subtract from the object beam intensity; (e) the object beam intensity from the retrieval process; (f) the relative error of the retrieval process.

[Fig. 3.7(b)] and the one from the retrieval process [Fig. 3.7(e)] are normalized; the difference between them is shown in Fig. 3.7(c), with the relative error shown in Fig. 3.7(f). For the object part, when the normalized intensity is greater than 0.5, the relative error is smaller than 8% and the root mean square (rms) error is less than 2%. Thus, the diagnostic also gives good results for the stacked soliton pulses in the spatial domain.

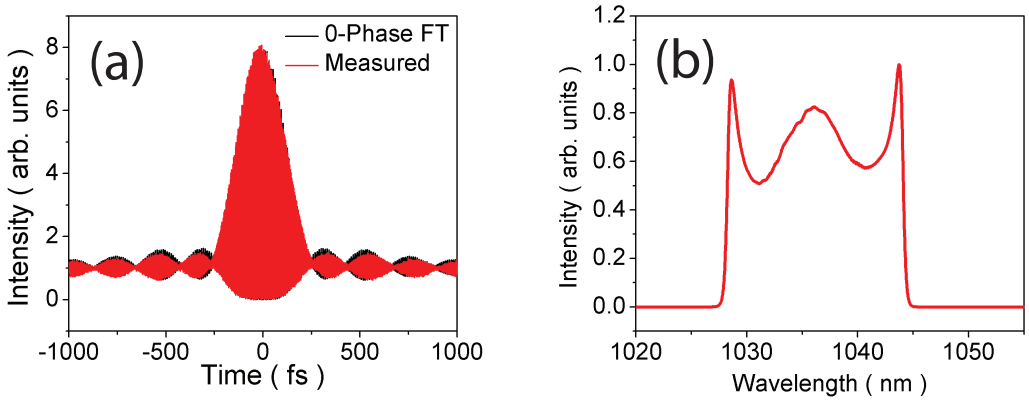

Figure 3.8: The ANDi fiber laser characterization. (a) the second-order autocorrelation, the black curve is the 0-phase spectrum Fourier transform (FT), the red curve is from measurement; (b) the spectrum.

3.5 Measurement of the pulse from an all-normal-dispersion laser

This diagnostic can also handle pulses with more complicated temporal structure, such as the pulse produced directly from a Yb-doped ANDi fiber laser [21]. Unlike in the soliton regime, where the pulse energy is limited by the area theorem [24], the ANDi regime can support much higher pulse energy. However, the pulses have a large and nearly linear frequency sweep or chirp, and are therefore not TL [21].

The linearly-chirped pulses can be dechirped to TL by a grating pair; with -0.33 ps^2 GVD, we dechirped the pulse to ~200 fs, close to the TL [Fig. 3.8(a)]. These pulses serve as the probe beam, also magnified by a 1:3 telescope to reduce the retrieval error. With a setup similar to the one used for the stacked soliton, we measured its 3-dimensional intensity.

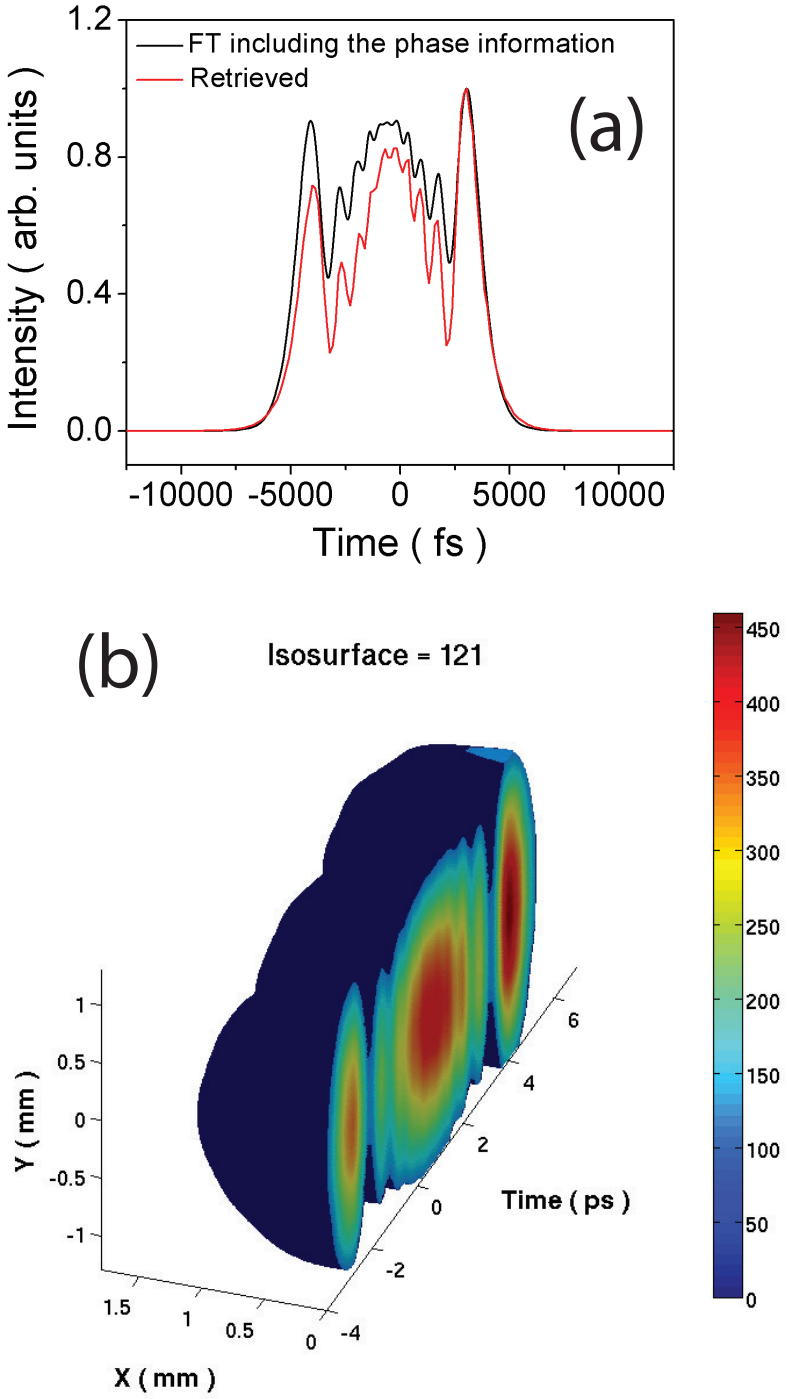

Figure 3.9: The ANDi fiber laser results. (a) the temporal intensity distribution; (b) the 3-dimensional intensity distribution, plotted in the iso-intensity surfaces.

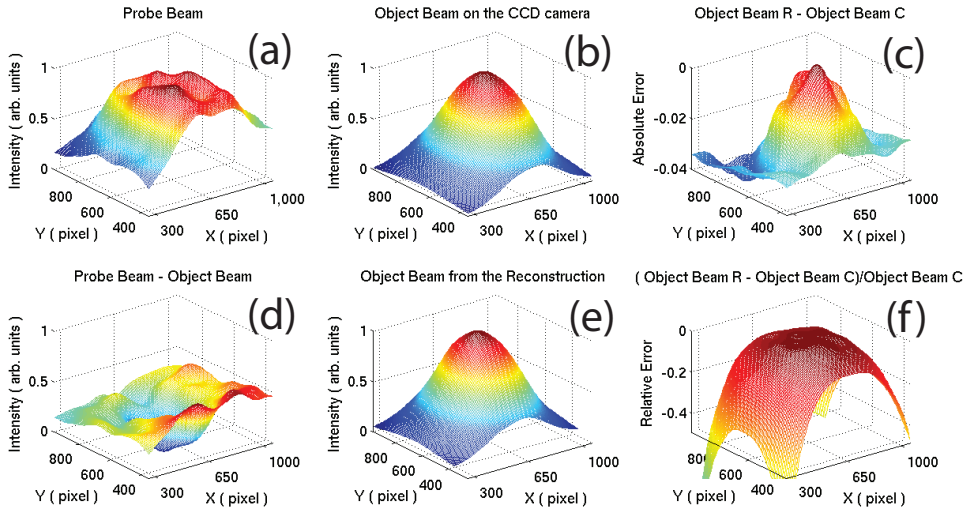

Figure 3.10: The intensity profile of the ANDi fiber laser. (a) the normalized probe beam intensity; (b) the object beam intensity on the CCD camera; (c) the object beam intensity difference between the retrieval process and the intensity on the CCD camera; (d) the probe beam intensity subtract from the object beam intensity; (e) the object beam intensity from the retrieval process; (f) the relative error of the retrieval process.

The temporal intensity is depicted in Fig. 3.9(a). The temporal profile looks similar to the spectrum because the pulse is highly linearly-chirped. The retrieval result is very close to the spectrum FT including the phase information, which again demonstrates good fidelity of this diagnostics. The small discrepancy comes from the δ function approximation in Eq. (3.2). Although the 200-fs probe pulse is indeed much shorter than the ~10 ps object pulse, and the broadening effect from the cross-correlation is negligible (<0.01%), the phase needs to be considered because only the coherent parts will add together. For this particular object pulse, the linear phase change across 200 fs is around π. The phase cross-correlation between the TL probe and highly linearly-chirped object pulses results in a shape similar to the temporal intensity profile of the object pulse. As discussed above, in this situation, the retrieved intensity profile

will have the correct qualitative features, but will have quantitative discrepancy from the correct result. This discrepancy is illustrated in Fig. 3.9(a).

The 3-dimensional intensity is depicted as the iso-intensity surfaces in Fig. 3.9(b). The method successfully recovers the structure present in the pulse. Fig. 3.10 shows good agreement for the spatial domain, even though the probe pulse profile suffered from scratches on the dechirping grating pair, and is far from being a Gaussian. Good results with less than 10% error for the center part of the object beam and ~2% rms [Fig. 3.10(f)] can still be obtained when the normalized intensity is larger than 0.5.

3.6 Discussion and limitations

We measured the 3D intensity of stacked soliton pulses and the pulse produced directly from an ANDi fiber laser based on this method [18, 19, 20]. Our results demonstrate good fidelity of this 3D technique in both the temporal and spatial domains, and illustrate the capabilities of the ready-to-use data-analysis toolkit.

Although in the results presented here the temporal and spatial parts of the pulse/beam were decoupled, the method can also handle situations that include space-time coupling. Some degradation in spatial resolution is anticipated from the spatial filtering in the case of sharp flat-top or super-Gaussian profiles, although we expect the resolution to remain adequate on a scale relevant for photoinjector applications.

There are some limitations to this method. First, it measures the intensity cross-correlation. When the probe pulse is much shorter than the object pulse,

the broadening effect is negligible, but the phase effect needs to be considered. The cross-correlated intensity has the same features as the object pulse, but needs to be correctly weighted. Second, as previously mentioned, the digital filters introduce some systematic error. The low-pass filter removes certain high spatial frequency, which will affect very sharp spatial edges in the laser beam profile. Despite these limitations, the method is simple and provides reliable 3D laser intensity profiles. We intend to apply this technique in our studies on how the electron beam emittance depends on the laser pulse intensity distribution. The 3D diagnostic will help minimize the electron beam emittance by allowing us to control and optimize the laser pulse shape incident on the photocathode.

3.7 Acknowledgments

We wish to acknowledge the support of John Dobbins for the help on the automation, Florian Loehl for the help on the digital filtering, and Dimitre Ouzounov for the helpful discussion. This work was supported by NSF award DMR-0807731.

BIBLIOGRAPHY

[1] S. M. Gruner, D. Bilderback, I. Bazarov, K. Finkelstein, G. Krafft, L. Merminga, H. Padamsee, Q. Shen, C. Sinclair and M. Tigner, "Energy recovery linacs as synchrotron radiation sources (invited)", Rev. Sci. Instrum. **73**, 1402 (2002).

[2] D. G. Ouzounov, I. V. Bazarov, B. Dunham, C. Sinclair, S. Zhou and F. W. Wise, "The laser system for the ERL electron source at Cornell University", Proceedings of PAC07, 10.1109/PAC.2007.4440268 (2007).

[3] I. V. Bazarov, B. M. Dunham and C. K. Sinclair, "Maximum Achievable Beam Brightness from Photoinjectors", Phys. Rev. Lett. **102**, 104801 (2009).

[4] O. J. Luiten, S. B. van der Geer, M. J. de Loos, F. B. Kiewiet and M. J. van der Wiel, "How to Realize Uniform Three-Dimensional Ellipsoidal Electron Bunches", Phys. Rev. Lett. **93**, 094802 (2004).

[5] R. Akre, D. Dowell, P. Emma, J. Frisch, S. Gilevich, G. Hays, Ph. Hering, R. Iverson, C. Limborg-Deprey, H. Loos, A. Miahnahri, J. Schmerge, J. Turner, J. Welch, W. White and J. Wu, "Commissioning the Linac Coherent Light Source injector", Phys. Rev. ST Accel. Beams **11**, 030703 (2008).

[6] I. V. Bazarov, D. G. Ouzounov, B. M. Dunham, S. A. Belomestnykh, Y. Li, X. Liu, R. E. Meller, J. Sikora, C. K. Sinclair, F. W. Wise and T. Miyajima, "Efficient temporal shaping of electron distributions for high-brightness photoemission electron guns", Phys. Rev. ST Accel. Beams **11**, 040702 (2008).

[7] I. V. Bazarov and C. K. Sinclair, "Multivariate optimization of a high brightness dc gun photoinjector", Phys. Rev. ST Accel Beams **8**, 034202 (2005).

[8] J. M. Diels, J. J. Fontaine, I. C. McMichael and F. Simoni, "Contorl and measurement of ultrashort pulse shapes (in amplitude and phase) with femtosecond accuracy", Appl. Optics **24**, 1270 (1985).

[9] R. Trebino and D. J. Kane, "Using phase retrieval to measure the intensity and phase of ultrashort pulses: frequency-resolved optical gating", J. Opt. Soc. Am. A **10**, 1101 (1993).

[10] C. Iaconis and I. A. Walmsley, "Self-Referencing Spectral Interferometry for Measuring Ultrashort Optical Pulses", IEEE J. Quantum Electron **35**, 501 (1999).

[11] W. Amir, T. A. Planchon, C. G. Durfee and J. A. Squier, "Complete characterization of a spatiotemporal pulse shaper with two-dimensional Fourier transform spectral interferometry", Opt. Lett. **32**, 939 (2007).

[12] C. Dorrer, E. M. Koski I. A. Walmsley, "Spatio-temporal characerization of the electric field of ultrashort optical pulses using two-dimensional shearing interferometry", Appl. Phys. B **74**, S209 (2002).

[13] M. Lelek, F. Louradour, A. Barthelemy, C. Froehly, T. Mansourian, L. Mouradian, J. Charmbaret, G. Cheriaux and B. Mercier, "Two-dimensional spectral shearing interferometry resolved in time for ultrashort optical pulse characterization", Opt. Soc. Am. B **25**, A17 (2008).

[14] E. Rubino, D. Faccio, L. Tartara, P. K. Bates, O. Chalus, M. Clerici, F. Bonaretti, J. Biegert and P. D. Trapani, "Spatiotemporal amplitude and phase retrieval of space-time coupled ultrashort pulses using the Shackled-FROG technique", Opt. Lett. **34**, 3854 (2009).

[15] M. A. C. Potenza, S. Minardi, J. Trull, G. Blasi, D. Salerno, A. Varanavicius, A. Piskarskas and P. D. Trapani, "Three dimensional imaging of short pulses", Opt. Commun. **229**, 381 (2003).

[16] P. Bowlan, P. Gabolde, A. Shreenath, K. McGreham, R. Trebino and S. Akturk, "Crossed-beam spectral interferometry: a simple, high-spectral-resolution method for completely characterizing complex ultrashort pulses in real time", Opt. Experess **14**, 11892 (2006).

[17] P. Gabolde and R. Trebino, "Single-frame measurement of the complete spatiotemporal intensity and phase of ultrashort laser pulses using wavelength-multiplexed digital holography", J. Opt. Soc. Am. B **25**, A25 (2008).

[18] Y. Li and J. W. Lewellen, "Generating a Quasiellipsoidal Electron Beam by 3D Laser-Pulse Shaping", Phys. Rev. Lett. **100**, 074801 (2008).

[19] Y. Li and S. Chemerisov, "Manipulation of spatiotemporal photon distribution via chromatic aberration", Opt. Lett. **33**, 1996 (2008).

[20] Y. Li, S. Chemerisov and J. Lewellen, "Laser pulse shaping for generating uniform three-dimensional ellipsoidal electron beams", Phys. Rev. ST Accel Beams **12**, 020702 (2009).

[21] A. Chong, J. Buckley and F. W. Wise, "All-normal-dispersion femtosecond fiber laser", Opt. Exp. **14**, 10095 (2006).

[22] S. Zhou, D. G. Ouzounov, H. Li, I. Bazarov, C. Sinclair and F. W. Wise, "Efficient temporal shaping of ultrashort pulses with birefringent crystals", Appl. Optics **35**, 8448 (2007).

[23] A. K. Sharma, T. Tsang and T. Rao, "Theoretical and experimental study of passive spatiotemporal shaping of picosecond laser pulses", Phys. Rev. ST Accel. Beams **12**, 033501 (2009).

[24] H. A. Haus, "Mode-locking of Lasers", IEEE J. Select. Topics Quantum Electron. **14**, 1173 (2000).

CHAPTER 4

DIRECT OPTICAL PHASE RETRIEVAL FROM A THREE-DIMENSIONAL INTERFEROMETER

We report temporal phase retrieval from a three-dimensional interferometer, which measures the noncollinear first-order cross-correlation. This diagnostic can directly retrieve the temporal phase when transform-limited reference pulses are available.

Originally appeared as H. Li, Z. Zhao, I. V. Bazarov, B. M. Dunham, and F. W. Wise, Conference of Laser and Electro-Optics (CLEO) 2012 CF3C.5. I am still preparing the manuscript for a journal.

4.1 Introduction

The phase of optical pulse is an intrinsic property of the optical field, so knowledge of the phase is fundamentally desirable. Amplitude and phase information are needed for many applications, such as the pulse compression [1, 2, 3], supercontinuum generation [4, 5], or generation of spatiotemporal solitons [6, 7, 8].

The intensity of an ultrashort pulse has been accessible since the invention of the autocorrelation [9], although the pulse shape must be assumed. The phase information has also become available after extensive studies, which have produced techniques such as the frequency-resolved optical gating (FROG) [10], spectral phase interferometry for direct electric-field reconstruction (SPIDER) [11], and their successors. FROG maps the temporal field into the spectrogram

and uses an iterative algorithm to retrieve the temporal field information; it works well in most applications. While SPIDER retrieves the field information from spectral shearing, and uses a direct retrieval algorithm.

However, both FROG and SPIDER can only obtain one-dimensional field information and in most of the cases, three-dimensional field information could only be obtained by brute force mainly because of the challenge of their implementation [12, 13, 14, 15, 16, 17]. Recently, we demonstrated that we could retrieve the three-dimensional intensity information with good fidelity from a three-dimensional interferometer [17], and this diagnostic has more capabilities that need exploration.

Here we present an optical phase retrieval based on this three-dimensional interferometer. The setup is simple, the retrieval process is direct and it can be applied to generic situations.

4.2 The experiment

The setup is essentially a noncollinear first-order cross-correlator with a charge-coupled device (CCD) camera as the detector [17]. The beam is split into the probe and the object beams. Ideally, we prefer the pulses in the probe beam to be transform-limited (TL), but the phases in the object beam can be arbitrary. These two beams are combined with a small angle so that they produce interference fringes when they overlap with each other in the space and time. The angle between these two beams is small and the spatial period of the interference pattern is also small but resolvable on the CCD camera, to provide good spatial resolution [17]. We have demonstrated that three-dimensional intensity

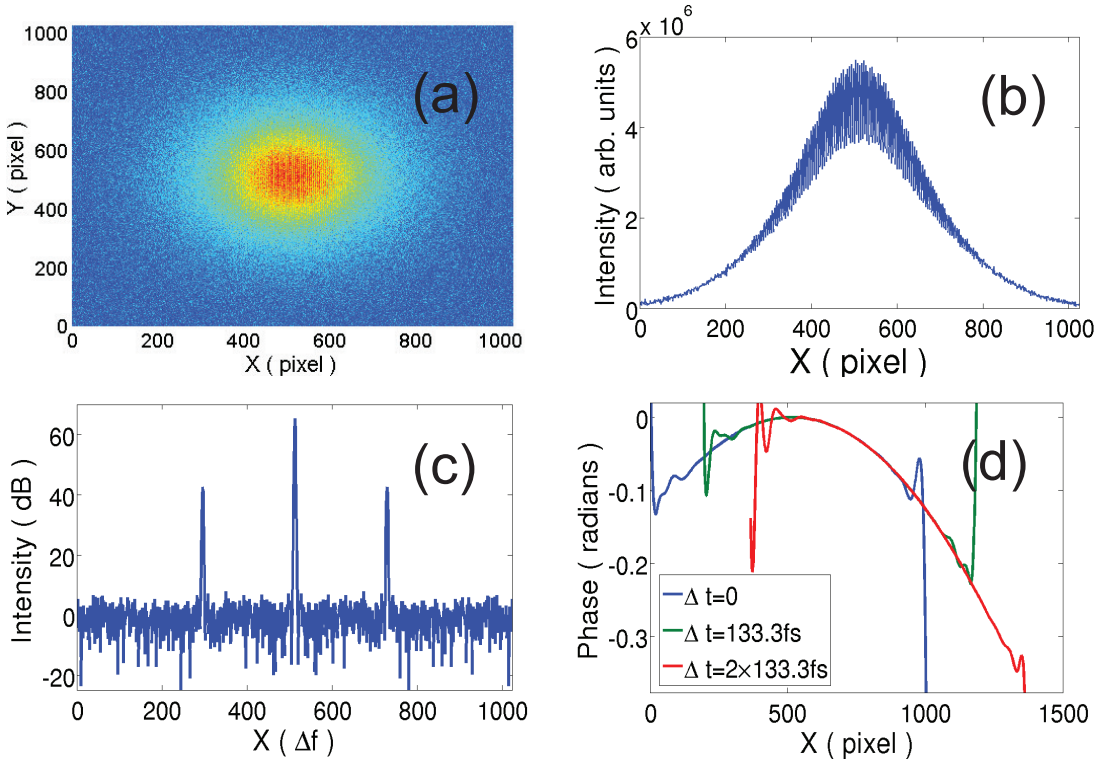

Figure 4.1: The conceptual phase retrieval process: a) the interference pattern on the CCD camera with noise, b) the interference pattern after summing along the direction of the fringes, c) the spatial spectrum, d) combining the temporal phases at different time delays.

could be retrieved with good fidelity [17]. The small angle between these two beams produces a time delay on the interference pattern from one side to the other; therefore the temporal phases are encoded there. Any phase structure that is oversampled by the spatial fringes can be retrieved; in our case, this period is twenty optical cycles at 1 micron wavelength. Because we rely on oversampling to retrieve the phase, there is a lower limit on the signal-to-noise ratio (SNR) of the fringes; for the one-dimensional case, this SNR is several thousand, and most commercial CCDs can satisfy this criterion after integrating over one axis for the one-dimensional phase retrieval. We will focus on the one-dimensional phase retrieval in this paper. After summing along the fringe

direction, a one dimensional fringe pattern is recorded [Fig. 4.2(b)]. Then we Fourier transform (FT) this fringe pattern to the frequency domain, we can then directly retrieve the phase information by inverse Fourier transform one of the sidebands [Fig. 4.2(c)] [18]. We obtain the phase information at different time delays and combining them together, we could retrieve the entire temporal phase information [Fig. 4.1(d)]. The sign ambiguity can be avoided once we know the time direction on the interference patterns.

We demonstrate this capability by retrieving the pulses which have group velocity dispersion (GVD) and third-order-dispersion (TOD) from grating pairs. The pulses from an all-normal-dispersion Yb-doped fiber laser [19] were dechirped to almost TL by a grating pair [Fig. 4.1(b)]. Then the beam is then split into the probe beam and the object beam by a non-polarization dependent beam splitter. The object beam travels through another grating pair with adjustable distances, where the GVD and TOD is imposed on the pulses. The probe beam is delayed and then combined with the object beam by a beam splitter with an angle 0.05 radians. The interference patterns are recorded on a CCD camera and then analyzed as described. Combining every slice at each time delay, we are able to retrieve the temporal phase from the pulse and achieve good agreement from the calculations. It agrees with the values calculated from the configuration of the grating pair [Fig. 4.2(d)]. The temporal intensity also agrees with the spectrum FT including the phase information, where the quantitative discrepancy may come from the phase cross-correlation effect [17] and also the fact that the probe pulses are not completely TL [Fig. 4.2(b)].

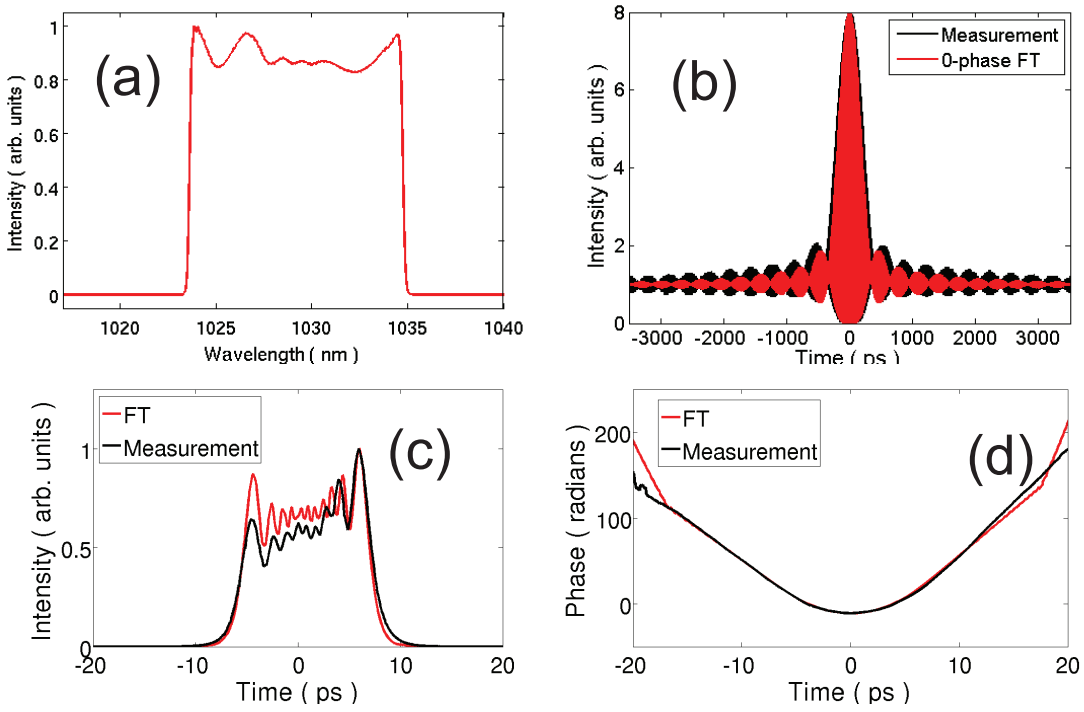

Figure 4.2: The experimental phase retrieval results: a) spectrum, b) measured autocorrelation and the 0-phase FT from the spectrum, c) the retrieved temporal intensity and the FT including the phase information, d) the retrieved phase and the phase imposed on the FT from the experimental configuration.

4.3 Conclusions

In conclusion, we demonstrate that this diagnostic can directly retrieve the temporal phase with good accuracy, and it can be applied to any arbitrary phase as long as the period of these phase structures are larger than the period of the interference fringes. This diagnostic will be useful for applications when pulses have complicated phase structures and also coherent close-to-TL reference pulses are available. Further work will explore the possibility to retrieve the three-dimensional phase.

4.4 Acknowledgments

Portion of this work were supported by the National Science Foundation (NSF)(ECS-0701680 and PHY-0131508) and the National Institutes of Health (NIH)(EB002019). Portion of this work were supported by the NSF award DMR-0807731.

BIBLIOGRAPHY

[1] W. H. Knox, R. L. Fork, M. C. Downer, R. H. Stolen, and C. V. Shank, "Optical pulse compression to 8 fs at a 5-kHz repetition rate", Appl. Phys. Lett. **46**, 1120 (1985).

[2] R. L. Fork, C. H. Brito Cruz, P. C. Becker, and C. V. Shank, "Compression of optical pulses to six femtoseconds by using cubic phase compensation", Opt. Lett. **12**, 483 (1987).

[3] A. Baltuska, Zhiyi Wei, M. S. Pshenichnikov, and D. A. Wiersma, "Optical pulse compression to 5 fs at a 1-MHz repetition rate", Opt. Lett. **22**, 102 (1997).

[4] J. K. Ranka, R. S. Windeler, and A. J. Stentz, "Visible continuum generation in air-silica microstructure optical fibers with anomalous dispersion at 800 nm", Opt. Lett. **25**, 25 (2000).

[5] W. J. Wadsworth, A. Ortigosa-Blanch, J. C. Knight, T. A. Birks, T.-P. M. Man, and P. St. J. Russell, "Supercontinuum generation in photonic crystal fibers and optical fiber tapers: a novel light source", JOSA B, **19**, 2148 (2002).

[6] X. Liu, L. J. Qian, and F. W. Wise, "Generation of Optical Spatiotemporal Solitons", Phys. Rev. Lett. **82**, 4631, (1999).

[7] A. Chong, W. H. Renninger, D. N. Christodoulides and F. W. Wise, "Airy-Bessel wave packets as versatile linear light bullets", Nature Photonics **4**, 103 (2010) .

[8] S. Minardi, F. Eilenberger, Y. V. Kartashov, A. Szameit, U. Rpke, J. Kobelke, K. Schuster, H. Bartelt, S. Nolte, L. Torner, F. Lederer, A. Tnnermann, and T. Pertsch, "Three-Dimensional Light Bullets in Arrays of Waveguides", Phys. Rev. Lett. **105**, 263901 (2010).

[9] J. M. Diels, J. J. Fontaine, I. C. McMichael, and F. Simoni, "Control and measurement of ultrashort pulse shapes (in amplitude and phase) with femtosecond accuracy", Appl. Opt. **24**, 1270 (1985).

[10] R. Trebino and D. J. Kane, "Using phase retrieval to measure the intensity and phase of ultrashort pulses: frequency-resolved optical gating", J. Opt. Soc. Am. A **10**, 1101 (1993).

[11] C. Iaconis and I. A. Walmsley, "Self-referencing spectral interferometry for measuring ultrashort optical pulses", IEEE J. Quantum Electron. **35**, 501 (1999).

[12] M. A. C. Potenza, S. Minardi, J. Trull, G. Blasi, D. Salerno, A. Varanavicius, A. Piskarskas, and P. D. Trapani, "Three dimensional imaging of short pulses", Opt. Commun. **229**, 381 (2004).

[13] P. Bowlan, P. Gabolde, A. Shreenath, K. McGreham, R. Trebino, and S. Akturk, "Crossed-beam spectral interferometry: a simple, high-spectral-resolution method for completely characterizing complex ultrashort pulses in real time", Opt. Express **14**, 11892 (2006).

[14] P. Gabolde and R. Trebino," Single-frame measurement of the complete spatiotemporal intensity and phase of ultrashort laser pulses using wavelength-multiplexed digital holography", J. Opt. Soc. Am. B **25**, A25 (2008).

[15] Y. Li and S. Chemerisov, "Manipulation of spatiotemporal photon distribution via chromatic aberration", Opt. Lett. **33**, 1996 (2008).

[16] S. L. Cousin , J. M. Bueno , N. Forget, D. R. Austin , and J. Biegert, "Compact spatio-temporal ultrashort pulse characterisation using a pulse shaper and a wavefront sensor", CTuH2, CLEO 2011.

[17] H. Li, I. V. Bazarov, B. M. Dunham , and F. W. Wise, "Three-dimensional laser pulse intensity diagnostic for photoinjectors", Phys. Rev. ST Accel. Beams **14**, 112802 (2011).

[18] M. Takeda, H. Ina, and S. Kobayashi, "Fourier-transform method of fringe-pattern analysis for computer-based topography and interferometry", JOSA, **72**, 156 (1982).

[19] A. Chong, J. Buckley, and F. W. Wise, "All-normal-dispersion femtosecond fiber laser", Opt. Express **14**, 10095 (2006).

CHAPTER 5

THREE-DIMENSIONAL INTENSITY AND TEMPORAL PHASE MEASUREMENT OF THE AIRY-BESSEL WAVE PACKET

We measured the three-dimensional intensity profile of the Airy-Bessel linear light bullet and clearly resolved its complicated three-dimensional structures. The measurement also retrieved its step-function-like temporal phase shift with π steps.

This chapter is submitted to Frontiers in Optics (FiO) 2012 by H. Li, C. Wan, A. Chong, and F. W. Wise. I am still preparing the manuscript for a journal.

5.1 Introduction

Generating a three-dimensional (3D) optical soliton, which is referred as a light bullet, has been an elusive challenge. Only limited successes have been achieved in this field because of the challenges to balance the dispersion, diffraction, and nonlinearity simultaneously in 3D against its inherent instability [1].

In contrast, numbers of 3D wave packets, which referred as linear light bullets, that propagate undistorted in linear media have been reported. For example, by coupling the temporal and spatial domain of wave packets appropriately, linear light bullets in the form of X-waves (such as a Bessel-X wave) and O-waves are possible in normal and anomalous dispersive media respectively [2]. Recently reported Airy-Bessel wave packet is qualitatively different from previously reported linear light bullets. It has an Airy profile in time domain with a Bessel profile in spatial domain. Its unique 3D iso-surface profile is

shown in Fig. 1(a). The Airy-Bessel wave packet is referred as a 'versatile' linear light bullet since it propagates without spreading for any media (regardless of any combination of diffraction and dispersion) by decoupling its spatial and temporal profile [3].

Even though there are many linear light bullets are reported, direct 3D measurements are still quite rare. Recently, a direct measurement of a Bessel-X wave by a spatially encoded arrangement for temporal analysis by dispersing a pair of light E-fields technique was reported [3]. A direct 3D measurement of the Airy-Bessel wave packet will be not only the first step to understand the exotic wave packet propagation further in 3D but also an interesting test bed for measurement techniques. Here we present the first 3D intensity and the temporal phase measurement of the Airy-Bessel wave packet by a simple 3D interferometer. A 3D interferometer measurement technique was recently demonstrated for its fidelity [5] and phase retrieval ability [6]. We successfully resolved the complicated 3D Airy-Bessel profile. A step-function like temporal phase shift with π steps is also retrieved.

5.2 The experiment

The setup for Airy-Bessel wave packet generation is very close to the setup in ref. [4]. Chirped pulses are generated from a Yb-doped fiber laser and divided into two arms with a beam splitter. One of arm is dechirped to 60 fs full width at half maximum (fwhm) with a grating pair, which serves as the probe pulse. The other arm of the beam goes through a specifically-designed grating telescope to cancel the group velocity dispersion (GVD) and also impose the

third-order dispersion (TOD) on it to produce the Airy temporal profile [4]. The cross-correlation between the probe and the Airy pulse is recorded as shown in Fig. 5.1(b). The temporal width of the main lobe of the Airy pulse is 150 fs fwhm. By passing through an axicon, a Gaussian beam profile converts into a Bessel beam profile to produce an Airy-Bessel wave packet. The central lobe of the Bessel beam has diameter 200 μm [Fig. 5.1(c)].

The measurement setup is same as shown in ref. [5]. For the 3D measurement, we cross-correlate the probe and the linear light bullet with a small angle [5]. We cross-correlated the probe and the Airy-Bessel wave packet with an angle 0.05 rad to produce spatial fringes with period 20 μm so that they are just resolvable by the CCD camera whose pixel size is 4.4 μm. The time step is around 25 fs and we took 400 slices at different time delays for the retrieval process. The 3D measurements are shown in Fig. 5.2.

The ideal iso-surface plot of a typical Airy-Bessel wave packet is shown in Fig. 5.2(a). Every lobe has a π phase step shift which comes from the Airy temporal profile. We successfully resolved its complicated structure. Fig. 5.2(b) shows the intensity profile measurement as an iso-surface plot, where the wave packet is cut in the middle in order to reveal its complicated structures. The lobes from the Airy pulse and the ring structure from the Bessel beam profile are clearly observed. Furthermore, we also retrieved its temporal phase based on the same setup. The angle between the probe and light bullet beam produces a time delay on the CCD camera and the phase information can be directly retrieved from interference fringes [6]. Since this method is based on inverse Fourier transform, it is direct and there is no ambiguity [6]. Fig. 5.2(c) shows the iso-surface intensity with a horizontal viewing angle. The tilted pulse could come from the fact that

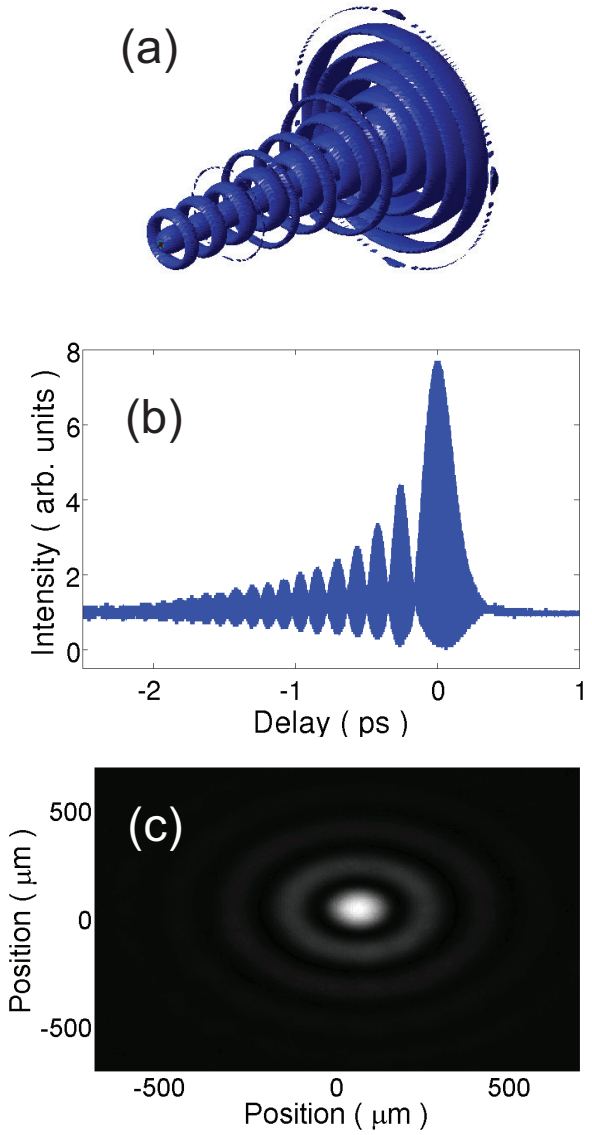

Figure 5.1: The Airy-Bessel pulse characterizations. a) theoretical three-dimensional intensity iso-surface, b) the temporal cross-correlation of the Airy pulse, c) the spatial intensity of the Bessel beam.

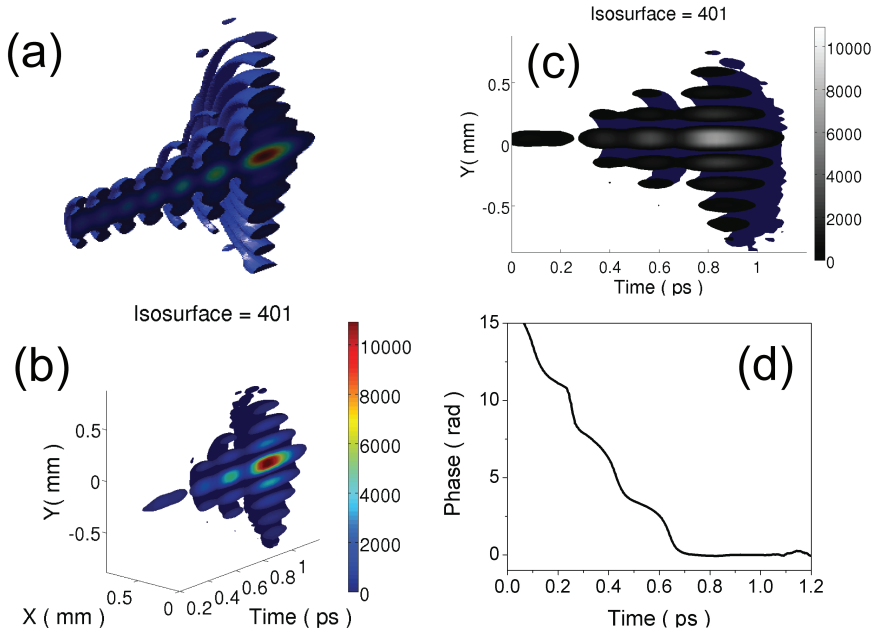

Figure 5.2: The Airy-Bessel light bullet. a), the expected three-dimensional intensity iso-surface, b), c) the three-dimensional intensity iso-surface from different viewing angles, d) the retrieved temporal phase.

the CCD camera was not perfectly perpendicular with the light bullet beam. Fig. 5.2(d) shows a clearly resolved temporal phase with a step-function-like with π phase shift.

5.3 Conclusions

In conclusion, we demonstrated the 3D intensity and the temporal phase retrieval of the Airy-Bessel wave packet. We successfully resolved the complicated intensity structures and the temporal phase in 3D with a very simple 3D interferometer measurement technique. Because of the capability of retrieving these complicated 3D intensity and temporal phase structure, we are confident that this diagnostic will be important once we push the electron emittance to its

very limit when the 3D shaping of the laser pulse profile is needed.

5.4 Acknowledgments

Portion of this work were supported by the National Science Foundation (NSF)(ECS-0701680 and PHY-0131508) and the National Institutes of Health (NIH)(EB002019). Portion of this work were supported by the NSF award DMR-0807731.

BIBLIOGRAPHY

[1] Y. Silberberg, "Collapse of optical pulses", Opt. Lett. **15**, 1282 (1990).

[2] H. E. Hernandez-Figueroa, M. Zamboni-Rached, and E. Recami, Localized Waves (John Wiley & Sons, 2008).

[3] R. Trebino, H. Valtna-Lukner, M. Löhmus, P. Piksarv, and P. Saari, "Directly Measuring the Spatiotemporal Electric Field of Ultrashort Bessel-X Pulses," in CLEO, OSA Technical Digest (CD) (Optical Society of America, 2009), paper CThW6.

[4] A. Chong, W. H. Renninger, D. N. Christodoulides and F. W. Wise, "Airy-Bessel wave packets as versatile linear light bullets", Nature Photonics **4**, 103 (2010) .

[5] H. Li, I. V. Bazarov, B. M. Dunham , and F. W. Wise, "Three-dimensional laser pulse intensity diagnostic for photoinjectors", Phys. Rev. ST Accel. Beams **14**, 112802 (2011).

[6] H. Li, Z. Zhao, I. V. Bazarov, B. M. Dunham , C. Wan, A. Chong and F. W. Wise, "Direct optical phase retrieval from a three-dimensional interferometer", CLEO 2012, CF3C.5.

CHAPTER 6

MULTI-VARIABLE EMITTANCE OPTIMIZATION, BEAM ALIGNMENTS AND CALIBRATIONS

The Cornell ERL photoinjector has many parameters such as the laser pulse profile, the shape of the gun focusing electrodes, gun high voltage (HV), solenoid currents, and RF amplitudes and phases. More than ten parameters need to be optimized simultaneously to achieve ultra-low emittance. The multi-dimensional nature of the problem dictates that it cannot be done by brute force and has to be done with some strategy. We use genetic algorithms to find the optimized parameter space and apply them in the experiments [1].

The experiment is complicated and matching it perfectly to numerical simulations is difficult. To reduce various aberrations, we have developed methods for the beam alignment to optimize the machine performance. We also found that some of the components such as the buncher amplitude and SRF cavity amplitudes were not as accurate as they should be, therefore, we performed various measurements to calibrate their amplitudes.

6.1 Emittance compensation

The ERL photoinjector is a complicated machine and has many variables that affect the transverse and longitudinal emittance [2, 3]. Because of the relatively low gun HV (350 kV), the space charge effects dominate the initial emittance growth. To compensate for the space charge effects, the beamline has two solenoids and a buncher in between. Loosely speaking, the first solenoid is

used to focus the beam inside the buncher to compensate the transverse space charge effect, while the buncher operates in the bunching mode that compresses the electron bunch to compensate the longitudinal space charge effect, then the second solenoid focuses the beam inside the first SRF cavity to shrink the beam size to compensate the time-dependent RF focusing [4, 5]. These three components along with the first SRF cavity are the most important elements once the laser profile is selected. Shaping the laser pulse profile can also reduce the emittance by up to a factor of two [1, 3]. Right now we are using laser pulses which have a near-flat-top temporal distribution 30 ps FWHM by stacking eight individual pulses with different polarization and a truncated-Gaussian in the spatial domain by truncating at its FWHM with an iris [6, 7]. The SRF cavity amplitudes and phases will also contribute to the emittance compensation. Assuming the on-crest phase is zero, phases smaller/larger than zero are near the bunching/debunching mode, which will compress/elongage electron bunches. By setting these SRF phases off-crest, we can further optimize the emittance a little more according to the General Particle Tracer (GPT)/A Space Charge Tracking Algorithm (ASTRA) simulations [9, 8]. However, because of the experimental uncertainties, we first operate the SRF cavities at their on-crest phases to simplify the investigation.

6.2 Multi-variable optimization

In such context, a genetic multi-variable algorithm is used to select the valid parameter space. The method was first pioneered in accelerator physics in [1]. The initial trials are taken; the random trials spread the parameter space; the sound solutions are selected, and mutations happen on them. After many gen-

erations, the solution parameter space becomes stable. Practically, we use GPT and ASTRA to perform the numerical simulation [8, 9]. GPT is developed in Netherlands, and has been used to simulate the Cornell ERL photoinjector prototype [3, 9]. ASTRA is developed at the Deutsche Elektronen-Synchrotron (DESY) in Germany, and has been used to perform the start-to-end simulations for the soft x-ray Free-electron -LASer in Hamburg (FLASH) [8]. We normally perform the simulation with two to five thousand particles as a start, then perform a two hundred thousand particle run to refine the results. Normally, their results are quite close. It takes several tens of minutes to run one ASTRA/GPT simulation with several thousand particles with the SC effect turned on from a quad-core computer. With ten parameters, if one generation contains three hundreds trials, it takes fifty generations before the solution becomes stable, which corresponds to days (weeks) of CPU time on a forty node quad-core computer cluster. The full optimization shows that at 20, 80 pC, the optimized transverse emittance are 0.15, 0.3 mm-mrad respectively [Fig. 6.4]. It is valuable to have such a simulation tool to guide the experiments.

The setup schematic of the emittance measurement system (EMS) is as shown in Fig. 6.1. It has two pairs of magnet scanners to shift the beam transversely, two EMS slits with opening 20 μm to select the beamlet [Fig. 6.3] [12], the Faraday to collect the current and the home-made fast charge amplifier with response time less than 0.1 ms to amplify the signal. The circuit diagram of the fast charge amplifier is depicted as in Fig. 6.2 [13]. The two-slit EMS contains two pairs of dipole magnets, that we call the magnet scanners. The first (second) scanner has two almost identical dipole magnets 0.700 m (0.687 m) away from each other with alternating pole direction, so that the electron beam is shifted after it goes through one of the scanner. The field integral of each magnetic dipole

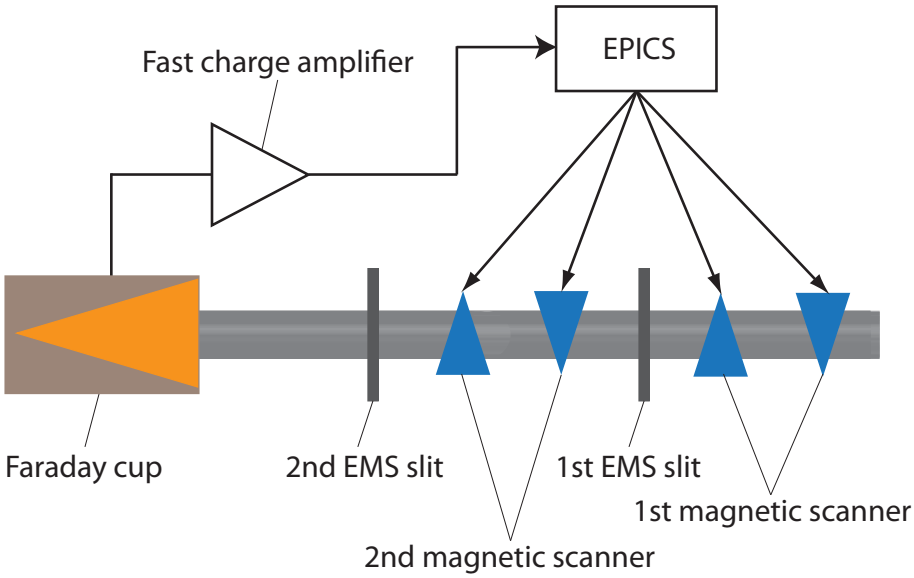

Figure 6.1: The setup schematic of the EMS, not to the scale. The beam direction is from the left to the right. EPICS, the Experimental Physics and Industrial Control System.

is measured experimentally, and the error of same dipole pair is within 5% [10]. The position and their field integrals are shown in Table. 6.1, where the position is the distance along the beamline from the photocathode [10]. The transverse shift (L_{shift}) of the beam can be calculated as Eq. 6.1 [11],

$$L_{\text{shift}} = D \cdot \frac{\int B_z dz}{\langle B\rho \rangle}, \tag{6.1}$$

where D is the distance between the two dipole magnets in one scanner, $\int B_z dz$ is the field integral, $\langle B\rho \rangle = 33.3564 P_0 \cdot \text{kG} \cdot \text{m}$, P_0 is the beam momentum with the unit GeV/c, c is the speed of light. The EMS slit is located just after the magnetic scanner to sample the beamlet. The first, second horizontal scanners are located at distance z =9.480, 10.755 m respectively; while the first, second vertical scanners are located at distance z =9.550, 10.825 m respectively. The scanner can work up to 2 kHz, and this defines our data acquisition rate. The

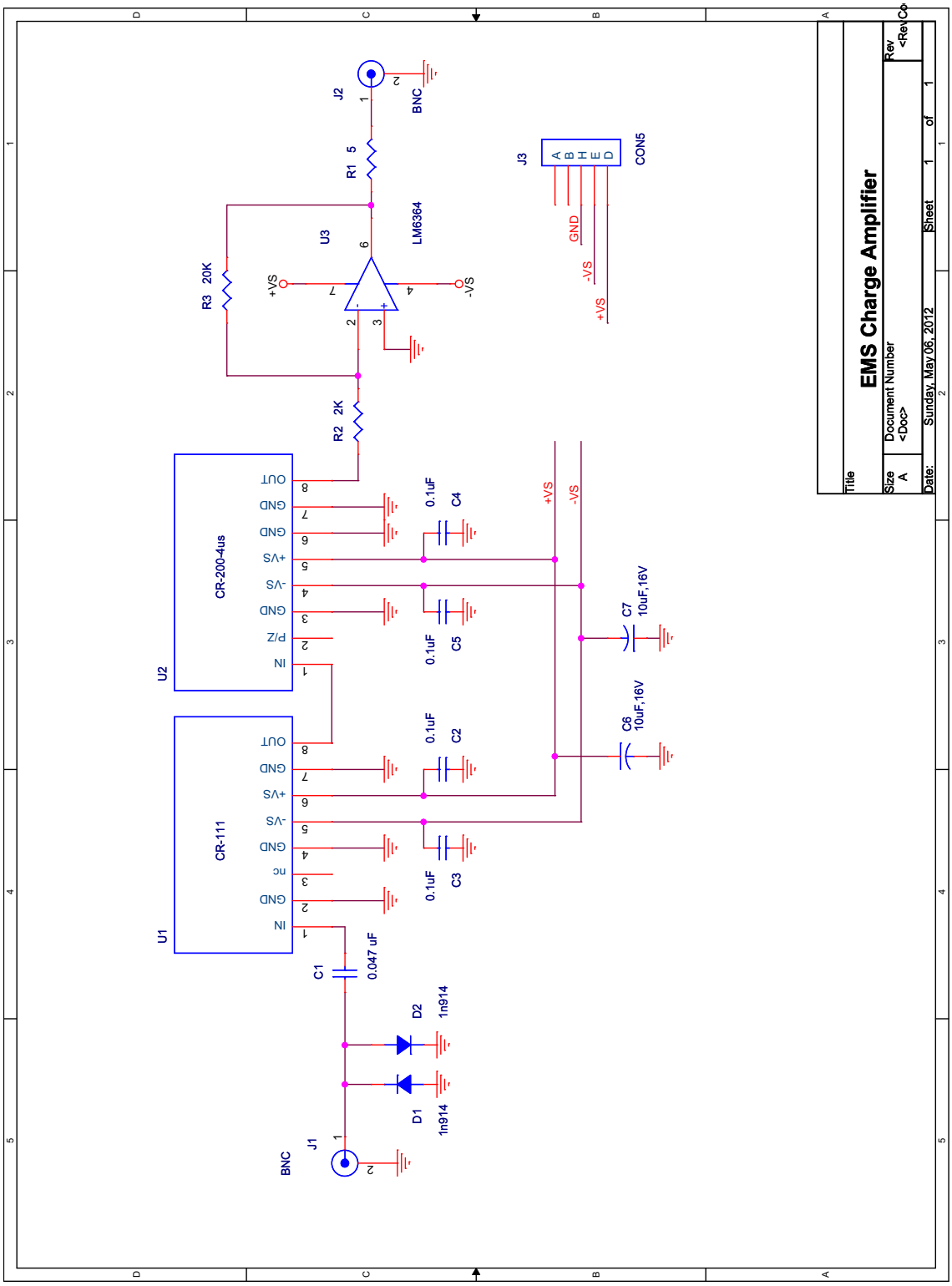

Figure 6.2: The circuit of the fast charge amplifier [13]. It makes use of modules from Cremat.com, CR-111 and CR-200-4uS [13].

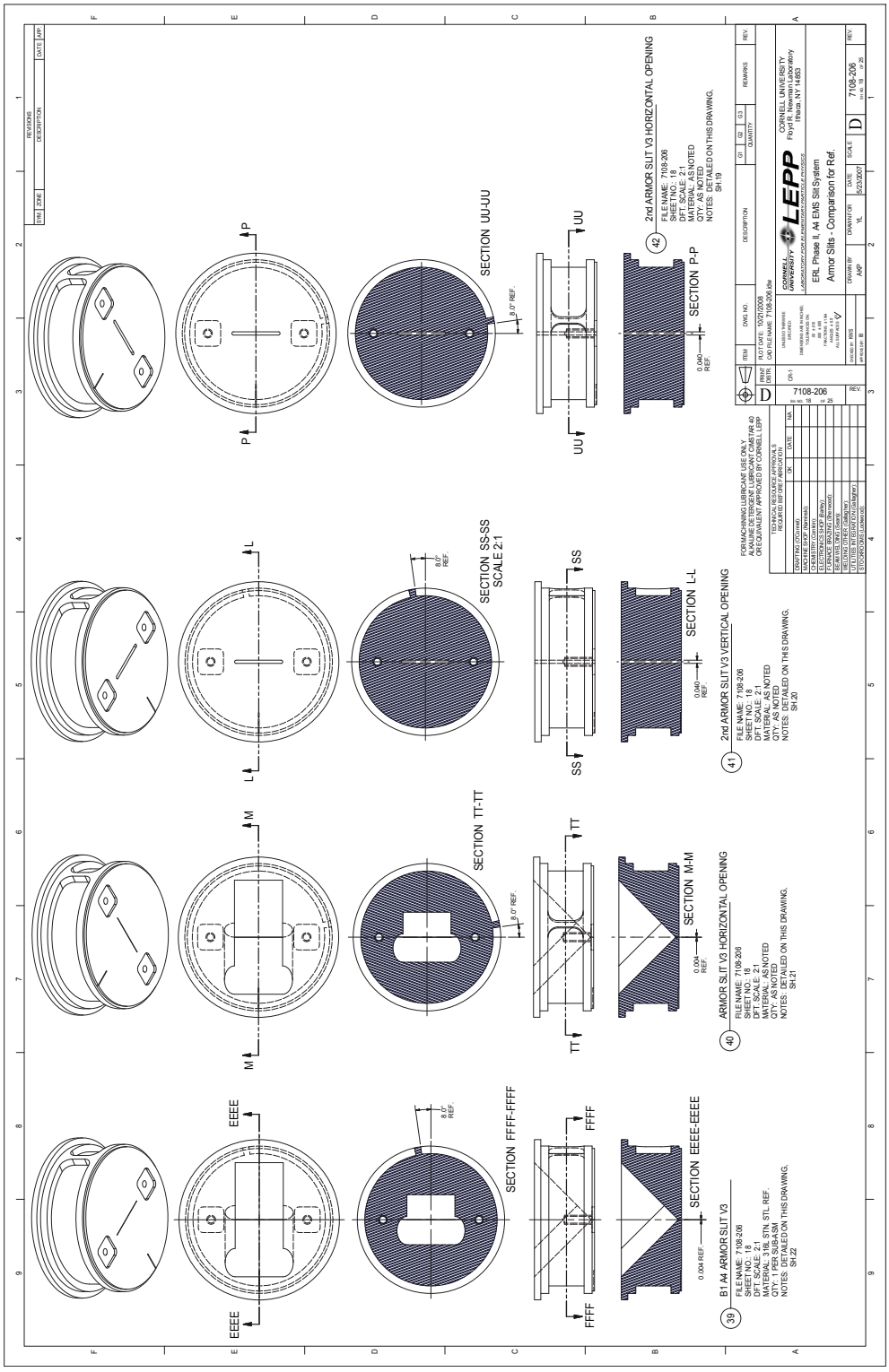

Figure 6.3: The mechanical design of the EMS slit [12].

Table 6.1: The position and field integrals of the magnetic scanners

Scanners	Distance z (m)	Field integral (G·m/A)
1st horizontal scanner corrector1	8.625	1.727
1st horizontal scanner corrector2	9.312	-1.684
1st vertical scanner corrector1	8.625	2.146
1st vertical scanner corrector2	9.312	-2.147
2nd horizontal scanner corrector1	9.709	1.702
2nd horizontal scanner corrector2	10.409	-1.689
2nd vertical scanner corrector1	9.709	2.170
2nd vertical scanner corrector2	10.409	-2.138

Faraday cup is located at distance z =11.393 m downstream the cathode and it is connected to a fast charge amplifier.

When the parameter space is much less complicated (less than four dimensions), brute force scan can be done. In the experiment have done first, the laser pulse profile is optimized according to the simulation guidance, with 2 mm diameter, 30 ps FWHM pulse duration, the gun HV operates at the stable maximum 350 kV, the beam energy is fixed to 5.7 MeV, and the buncher operates at 50 kV. In such a case, the solenoid currents are the most important factors: they are essentially the linear lenses plus rotation used to compensate the transverse SC effect, and also focus the beam inside the buncher, and the first SRF cavity so that the beam does not pick up too much time-dependent RF focusing. I ran ASTRA to scan the two solenoid currents from 0 to 4 A in the step of 0.2 A. The simulation result indicates that if the first solenoid current is 3.8 A and the second solenoid current is 2.0 A, we can obtain the emittance 1.0 mm-mrad in both the horizontal and vertical plane, with bunch length 10 ps rms. We imple-

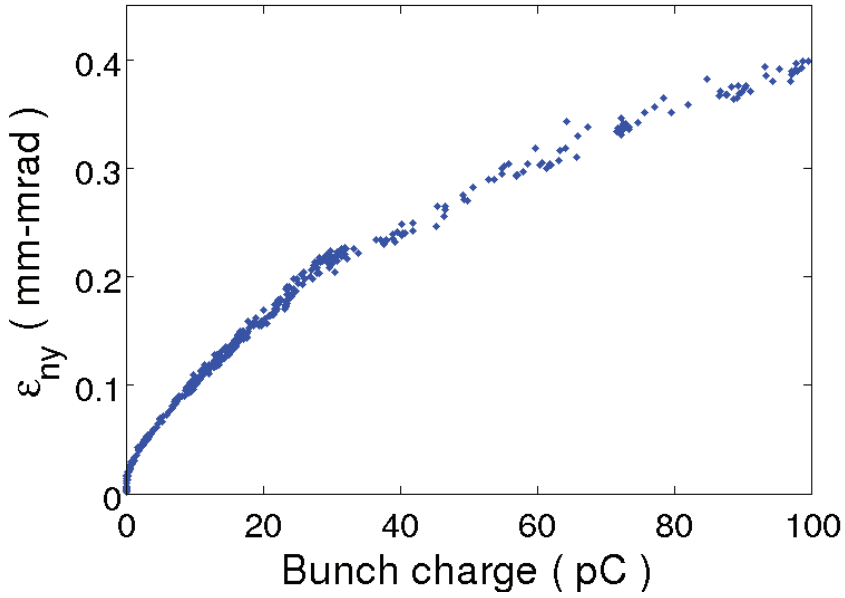

Figure 6.4: The full optimization of the Cornell ERL photoinjector 9.5 m after the photocathode at different bunch charge.

mented these settings in the experiment, and immediately we obtained emittance 2.0 mm-mrad in both planes in the May 2011, which is about twice smaller compared to the 3.6 mm-mrad in the March 2010 [10]. With further more careful experimental optimizations, we obtained 1.0 mm-mrad emittance in both planes; the bunch length was measured to be 14 ps rms, which is about twice longer than the results from the numerical optimizations [10]. We will discuss the discrepancy in the later parts of this chapter.

Being encouraged by the experiments, we continued the numerical optimization in both GPT and ASTRA. This time we set more variables to be optimized, that included two solenoid currents, the buncher voltage, the SRF cavity amplitudes on-crest, at 20 and 80 pC. The results were more promising, with emittances smaller than 0.7 mm-mrad and bunch lengths shorter than 8 ps rms. A little to our surprise, although the buncher voltage was a little higher (60 kV

compared to 50 kV), the two solenoid currents are still close to the ones obtained by the brute force approach (3.8 A and 2.0 A). We tried these parameters in the experiments; we could get the emittance 0.8 mm-mrad, however, the bunch lengths were always longer than 15 ps rms. In order to investigate this, we checked various things, the first thing is to calibrate the gun and RF amplitudes.

6.3 Beam alignment and voltage calibrations

In the theoretical as well as experimental studies, we found that the misalignment of elements in the beamline can contribute a lot to the emittance growth [3, 10]. Therefore, we developed various methods to align the beam inside the beamline. We center the laser beam in the gun field center, then we align the beam in the buncher and the first two SRF cavities, after that, we move the two solenoids physically to center them in the beamline.

6.3.1 Laser beam centering

We align the laser spot in the gun center first. The gun field strength varies at different locations, this results in the focusing force. We set the laser beam to the 'continuous-wave' mode and put in the smallest 200 μm pinhole to align the beam based on the aberration of the gun focus. It is done by moving two one-dimensional optical stages: one of them moves in the horizontal direction while the other one moves in the vertical direction. After scanning each direction by ±5 mm, and doing a fitting algorithm, we can center the laser beam on the center

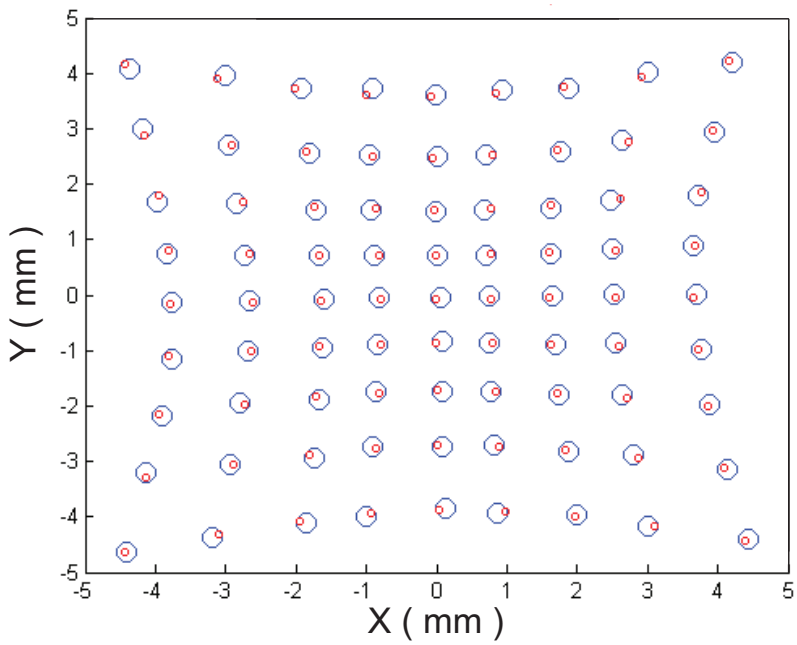

Figure 6.5: Scanning the laser spot on different spots on the photocathode. The blue circles are the calculation, while the red circles are the measurement. The gun field focusing is observed.

of the gun field as shown in Fig. 6.5.

6.3.2 The buncher and the first two SRF cavity alignment

After centering the laser spot in the gun, we align the buncher using the first A1 corrector pair. The laser also operates in the 'continuous-wave' mode, and the laser power was reduced to avoid damage on the view screen.

We compare the beam locations on the A3 view screen when the buncher is off and in the debunching mode. Then we can calculate the position offsets of the beam inside the buncher, and move the first A1 corrector pair to compensate these offsets. After several iterations, the beam is centered inside the buncher.

The offset measurement and calculation is done by one Matlab script which uses the buncher cavity field map.

The alignment of the first two SRF cavity is similar to the buncher alignment: we use the last A1 and the A2 corrector pairs to center the beam inside the first two SRF cavities. It is a little trickly to perform the alignment because the two corrector pairs are coupled together, it is like to use two 'z-configuration' mirrors to guide the laser beam through two pinholes: we used the last A1 corrector pair to center the beam in the first SRF cavity and used the A2 corrector pair to center the beam in the second SRF cavity and by iterating, we could get the beam aligned in both of them. Later we found that it could be done by using the response matrix.

Let us take the horizontal correctors as the example. Assume position offset measured by the first SRF cavity is x_1. It comes from both the correctors C_1 and C_2, and $x_1 = h_{11}C1 + h_{12}C2$, where h_{11} (h_{12}) is the unit offset from unit corrector current C_1 (C_2). The second SRF cavity has the similar effect, $x_2 = h_{21}C1 + h_{22}C2$. This effect can be written as

$$\begin{bmatrix} x_1 \\ x_2 \end{bmatrix} = \begin{bmatrix} h_{11} & h_{12} \\ h_{21} & h_{22} \end{bmatrix} \begin{bmatrix} C_1 \\ C_2 \end{bmatrix}. \tag{6.2}$$

Because the last A1 corrector is further from the first SRF cavity, therefore, we expect $h_{11} > h_{12}$. It is the same for the A2 corrector, therefore, we have $h_{21} > h_{22}$. Also because that the two correctors are relatively close, and the second SRF cavity are further from the first SRF cavity, therefore $h_{11} \sim h_{22}$ and $h_{11} < h_{21}$. The measurement shows that h_{11}=50, h_{12}=10, h_{21}=115, h_{22}=41, where the unit is μm/mA. Once we measured the offset x_1, x_2, it is easy to calculate the correction

currents that are needed to be applied to the corrector currents C_1 and C_2,

$$\begin{bmatrix} C_1^{\text{correction}} \\ C_2^{\text{correction}} \end{bmatrix} = - \begin{bmatrix} h_{11} & h_{12} \\ h_{21} & h_{22} \end{bmatrix}^{-1} \begin{bmatrix} x_1 \\ x_2 \end{bmatrix}. \tag{6.3}$$

When the initial offsets x_1, x_2 are less than 1 mm (which usually is the case), at most three iterations are needed to find the corrector currents C_1, C_2. We also measured the response matrix for the vertical direction, and found that v_{11}=60, v_{12}=18, v_{21}=153, v_{22}=68, where the unit is also μm/mA. These matrices were measured when the gun HV is 350 kV, SRF1 and SRF2 amplitudes 50 kV.

6.3.3 Solenoid alignment

The solenoids' alignment is difficult because initially, these solenoids are not designed to be movable. Now several motors are installed to move them. For one of the solenoids, two of the motors move it in the plane that is perpendicular to the beamline; two of them move it in the angular direction that is perpendicular to the beamline. They need to be aligned so that the beam travels through the center of it and its plane should be perpendicular to the beamline.

6.4 The gun and RF cavity amplitude calibrations

We calibrated the gun and RF cavity amplitudes by using both the BPM arrival time method and a magnetic spectrometer. Because the speed of the electron bunches are still not fully relativistic just after the gun, we used the BPM arrival

time to calibrate the gun HV. When the electron beam energy is several MeV, the dipole magnet which measures the beam momentum gives a more accurate beam energy value so that we use it to calibrate the RF cavity amplitudes. We also calibrated the buncher amplitude with the gun HV as a reference.

6.4.1 The gun amplitude calibration

The BPMs measure the phases based on when the electron bunches arrive. When we use two BPMs to measure the phases, we can calculate the speed of the electron bunches because we also know the position of these BPMs; because the speed of the electron bunches are still not fully relativistic (β <0.8 when gun HV<350 kV), we can change the gun HV and measure the speed of these electron bunches. We measure the time of flight to calculate the electron bunch speed. The gun HV calibration shows that the gun HV is very accurate, within 0.5% as depicted in Fig. 6.6, that is not a surprise for the good direct current high power supply.

6.4.2 The buncher and SRF cavity amplitude calibrations

The amplitude calibrations of the RF cavities are a little more complicated. When the electron beam goes through the RF cavities, because the non-perfect beam alignment, it will be kicked transversely due to the time-dependent RF focusing; also because its speed is approaching the speed of light (c), thus the time difference from the energy difference is smaller (several ps, or several mm in distance) and become comparable with the orbit difference from the trans-

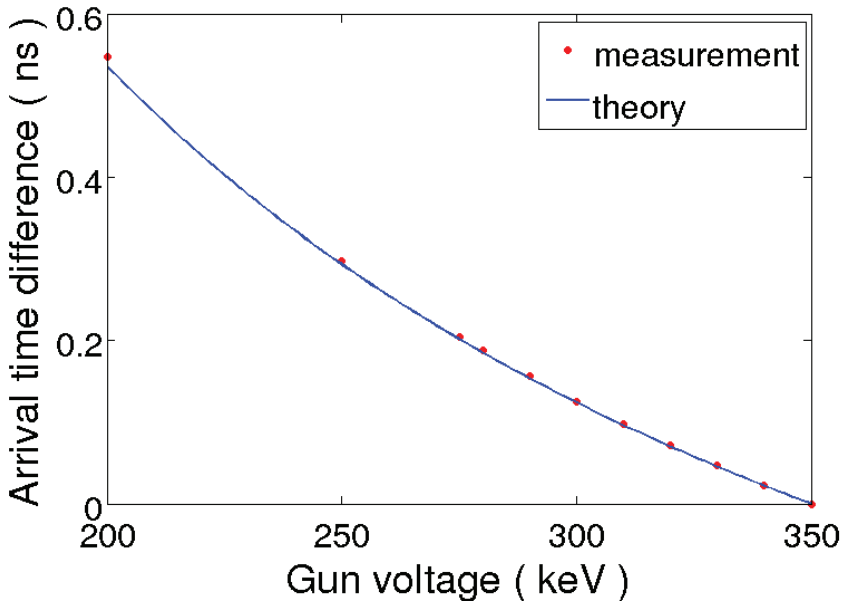

Figure 6.6: The gun amplitude calibration by BPM arrival time difference, the dots are the measurement, and the curve is the expected behavior.

verse kicks (several mm over more than 5 m). We tried to calibrate the RF cavity amplitudes by the BPM arrival time difference, but it did not work well. Then we calibrate all the RF cavity amplitudes (the buncher and the SRF cavities) with the dipole magnet because we know its field map and can calculate the beam energy from its current. In experiment, we direct the beam to the C2 section, and keep the beam spot nearly the same by adjusting the dipole current while keeping the beam orbit about the same after the cryomodule.

We first calibrate the buncher, from 10 to 130 kV in the step of 10 kV, at less than 1 pC bunch charge [Fig. 6.7], then we set it to 50 kV in the bunching mode to calibrate the SRF cavities. In the SRF cavity calibrations, we set the SRF cavity amplitudes from 200 kV to 1600 kV in the step of 200 kV, then set them to 1395, 825, 1100, 1100, 1100 kV, and turn them one by one to calibrate the amplitudes. We keep the beam orbit the same before the beam enters the C2 dipole section

Table 6.2: The SRF cavity calibration results

The SRF cavity	ASTRA slope	Measured slope	Correction
Buncher	0.8897	0.7949	0.89
SRf1	0.9277	0.9251	1.00
SRF2	0.9856	1.006	1.02
SRF3	0.9932	0.9721	0.97
SRF4	0.9977	0.8246	0.82
SRF5	0.9996	0.8962	0.89

to minimize the error from the orbit. Then we plot the RF cavity voltage vs. the measured energy from the C2 dipole as in Fig. 6.7 and Fig. 6.8, and then extract the slopes from these graphs. By comparing these slopes with the ASTRA simulations, we can obtain the calibrations of these RF cavities. The buncher and SRF cavity calibration results are shown in Table. 6.2: the calibrated values should be the previous values on the Experimental Physics and Industrial Control System (EPICS) screen times the correction factor. For example, if the previous EPICS screen value of the SRF5 cavity reads 1000 kV, its real voltage is 1000×0.89 kV=890 kV.

6.5 The bunch length investigation

In the experiment done in 2011, we achieved normalized transverse emittance 0.8 mm-mrad in both planes [10]. However, the bunch length was 15 ps rms, which is about twice longer than the optimized results from the GPT and ASTRA numerical simulations. It turned out that several effects could contribute

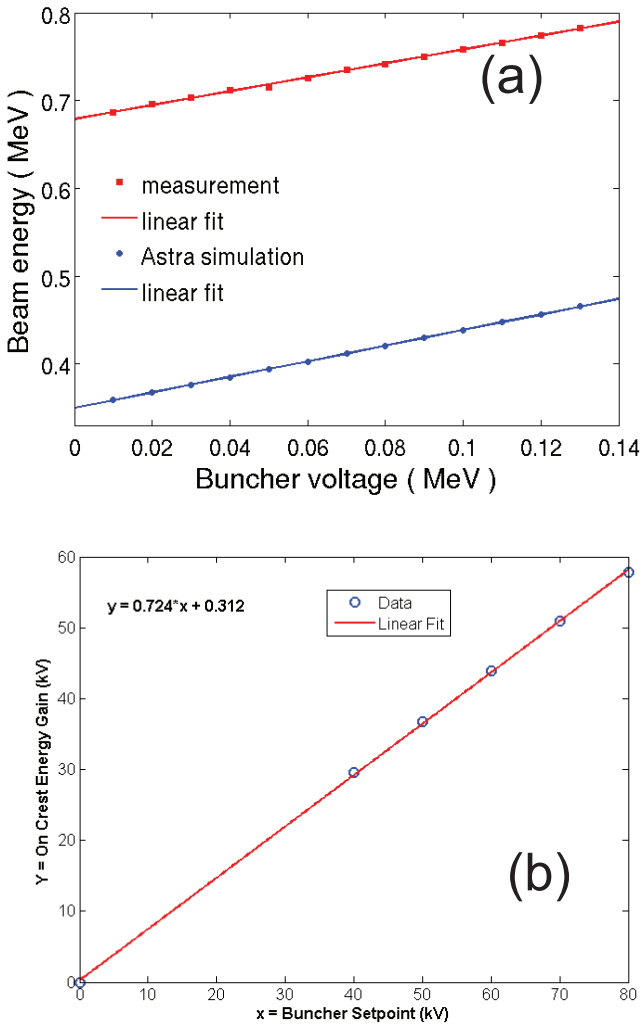

Figure 6.7: The buncher voltage calibration. a) the measured and simulated buncher energy gain, b) the buncher calibration by changing the gun HV.

to it: the most severe one is the buncher voltage miscalibration, the second one is the transient effect of the RF cavities, the third one is the method of phasing the SRF cavities.

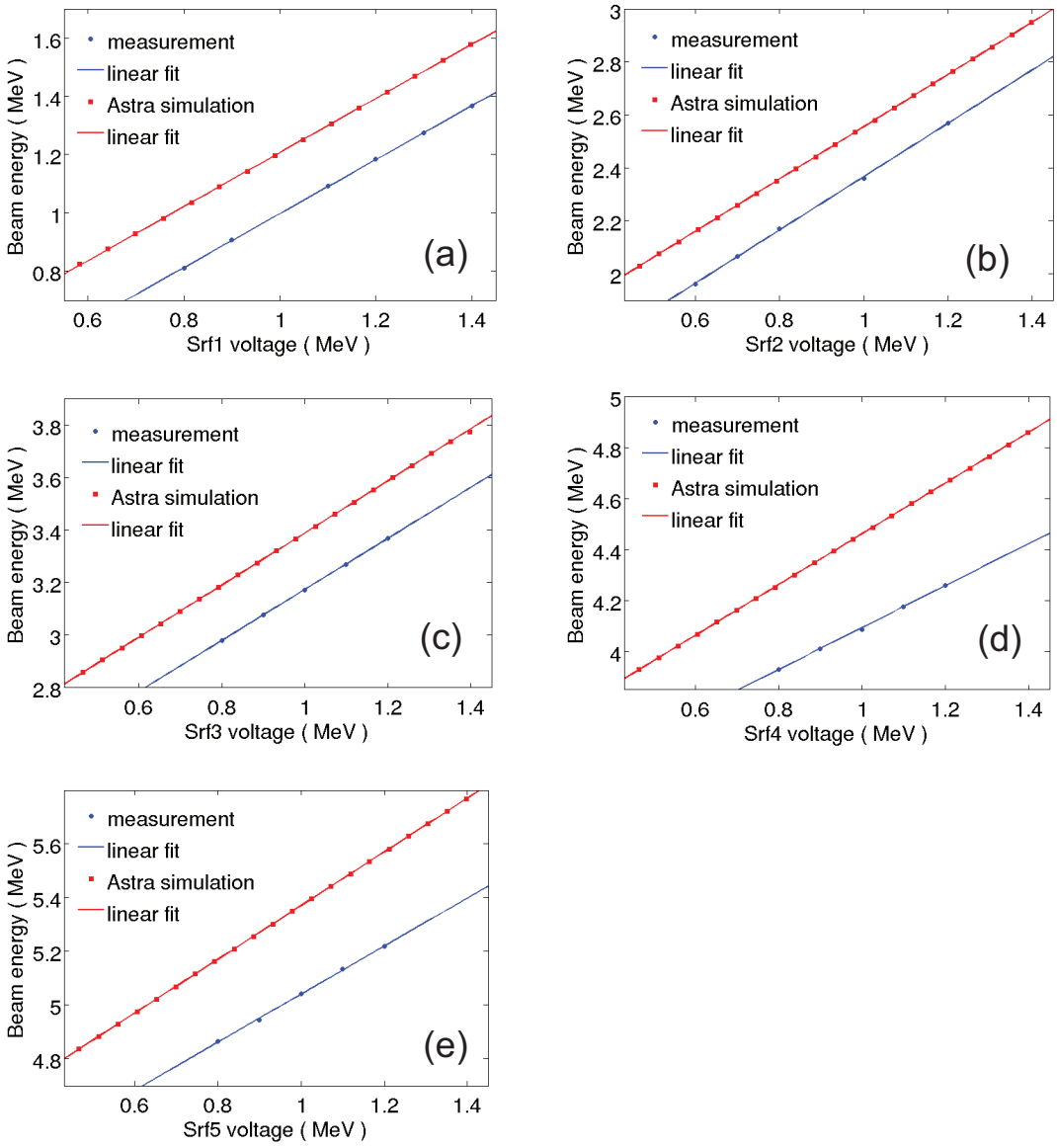

Figure 6.8: The SRF cavity amplitude calibrations. a), b), c), d), e) the SRF1, SRF2 SRF3, SRF4, SRF5 cavity amplitude calibration, the blue dots are the measurements, the red squares are the ASTRA simulations. The red lines are the linear fits of the measurements, the blue lines are the linear fits of the ASTRA simulations.

6.5.1 The buncher effect

At the full bunch charge (77 pC), the buncher works in the bunching mode to compress the bunch length and also to compensate the longitudinal space charge effect. It is an important element in the emittance compensation section. According to the ASTRA/GPT numerical simulations, the buncher should operate at 60 kV to produce bunch length 8 ps rms at 80 pC bunch charge. We did not question the calibrations of the buncher until we observed the large discrepancy in the bunch length measurement.

Then we performed GPT simulations to change the buncher strength and to observe the bunch length variations. It turns out that the bunch length is very sensitive the buncher strength. Simulations show that changing the buncher strength by 20% is large enough to change the bunch length by a factor of two [Fig. 6.9(a)]. The beam size also varies quite a bit when the buncher strength varies, because the phase space volume remains about the same near the optimized operating point [Fig. 6.9(b)]; while the transverse emittance remains about the same [Fig. 6.9(c)].

Then we used two methods to calibrate the buncher voltage. The first method is to use the dipole magnet to measure the beam energy while keeping the orbit the same after the cryomodule. The second one is to change the gun HV while keeping one BPM phase after the cryomodule the same, because the gun HV is well calibrated. The first method shows that the buncher has 89% of its nominal strength [Fig. 6.7(a)]; the second method shows that the buncher has 85% of its nominal strength [Fig. 6.7(b)]. These results are close and we took the results from the second calibration method because the gun HV is more trustable and has less error.

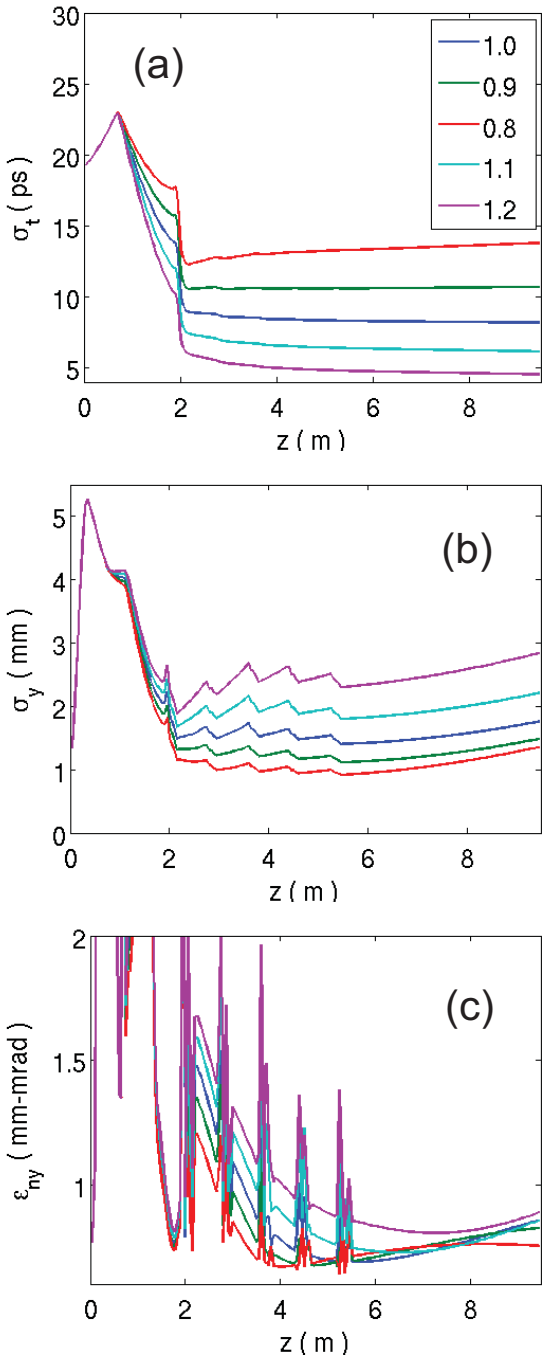

Figure 6.9: The buncher strength effect on the bunch length. a) the beam line position vs. the bunch length, 1.0 corresponds to the optimized buncher strength at 60 kV, b) the beam line position vs. the beam size, c) the beam line position vs. the vertical emittance. Different lines correspond to different relative buncher strength respect to 60 kV.

After we corrected the buncher calibration, it is much easier to produce a shorter bunch length at the full bunch charge.

6.5.2 The transient effect of the RF cavities on the bunch length measurement

The observed bunch length is about twice longer than the simulations at full bunch charge in the experiments done in 2011. The discrepancy is smaller at the lower bunch charge, and negligible at the near-zero bunch charge (experimentally smaller than 0.1 pC). We attribute the larger discrepancy of the bunch length measurement partially to the transient effect of the RF cavities: when we are measuring the bunch length, we have to operate the machine in the macro-bunch mode, where a Pockels cell chops down the 50 MHz laser pulse train to macro-pulses with repetition rate of several kHz and macro-bunch length of several μs; when these macro-bunches pass through the RF cavities (the buncher, the SRF cavities and the deflecting cavity), they deposit energy to these cavities at the head of the macro-bunch, however, the RF regulations could not compensate the energy change from these macro-bunches at the bunch head and over correct the voltages/phases at the bunch tail. Therefore, the bunch head loses energy while the bunch tail gains energy; these transient effects change the amplitudes and phases experienced by bunches at different temporal part of the macro-bunch, and these change their energy gain, and their arrival time. These transient effects can be approximated by equations below,

$$\Delta E_{\mathrm{kin}} = E_{\mathrm{gain}} \sin\Delta\phi \sim E_{\mathrm{gain}}\Delta\phi, \qquad \text{buncher} \tag{6.4}$$

$$\Delta E_{\text{kin}} = E_{\text{gain}}\Delta\eta, \qquad \text{SRF cavity}, \tag{6.5}$$

$$\Delta\gamma = \frac{1}{mc^2}\Delta E_{\text{kin}}, \tag{6.6}$$

$$\tilde{\beta} = \sqrt{1 - \frac{1}{(\gamma + \Delta\gamma)^2}} = \beta + \Delta\beta, \tag{6.7}$$

$$\Delta t = \frac{\Delta l}{\beta c} - \frac{\Delta l}{(\beta + \Delta\beta)c} \approx \frac{\Delta l \Delta\beta}{\beta^2 c} \approx \frac{\Delta l}{\beta^3 c}\frac{\Delta\gamma}{\gamma^3}, \tag{6.8}$$

where E_{gain} is the energy gain from the RF cavity, $\Delta\phi$ is the phase transient, $\Delta\eta$ is the relative amplitude transient, and Δl is the distance from the RF cavity under investigation to the next RF cavity, because usually the beam energy is boosted closer to the speed of light (c) and then the arrival time difference in the previous cavity is frozen. The phase transient from the buncher in the bunching mode results in the residual beam energy change, and the amplitude transient of the SRF cavity also changes the beam energy, then the arrival time. Because the slice emittance bunch length measurement is an average measurement over several ms at each phase space point, hence any fluctuation of the arrival time elongates the measured bunch length. Furthermore, the transient effect is proportional to the average current of the macro-bunch, thus this artificially elongated effect becomes stronger at the higher bunch charge and is negligible at the near-zero bunch charge, as we expected, as well as what we observed.

We observed these transient effects experimentally by monitoring the amplitudes and phases from probes inside the RF cavities on an oscilloscope. The buncher phase changes by ±3° peak-to-peak, and the first two SRF cavity amplitudes change by ±3% peak-to-peak. The buncher, SRF1, SRF2 and SRF3 cavities locate at 0.714, 2.047, 2.833, 3.696 m respectively along the beamline. When the machine setting is the same as in Table. 7.2, from Eq. (6.8), 1° buncher phase tran-

sient corresponds to 3 ps arrival time change, 1% of SRF1 and SRF2 cavity amplitude transient corresponds to 1 and 0.2 ps arrival time change respectively; these agree with the simulation results in Fig. 6.10 to the first order. Simulations show that 1° change in the buncher phase can change the arrival time by 2 ps rms [Fig. 6.10(a)], while 1% variation in the SRF1 and SRF2 amplitude change can result in 1 and 0.2 ps [Fig. 6.10(b) and (c)] change in the arrival time respectively. Therefore, the entire transient effect can produce 4 ps rms artificially elongated measurement if these effects are independent of each other [Fig. 6.10(d)]. These can account for 50% of the bunch length measurement discrepancy.

6.5.3 The method of phasing the RF cavities

In the experiment, we need to phase the buncher and the SRF cavities. For all the data in this thesis, the gun HV normally operates at 350 kV, which corresponds to β ~0.8. The beam from the gun is near-relativistic, but not ultra-relativistic. This brings some complications in the beam operation, one of them is the emittance compensation, another one is the phasing of the SRF cavities.

There are several ways to phase the RF cavities: the first is to use one BPM after the cryomodule to measure arrival time, the second one is to use two BPMs after the cryomodule to measure the arrival time difference, the third one is to use the dipole magnet to measure the beam energy. At the very beginning, we used the dipole magnets to measure the beam energy. However, because the electron beam is not perfectly centered in the RF cavities, thus it will be kicked by the time-dependent RF focusing, and this effect will change the orbit. This effect gives the artificial effect on the measured beam energy. Although it is

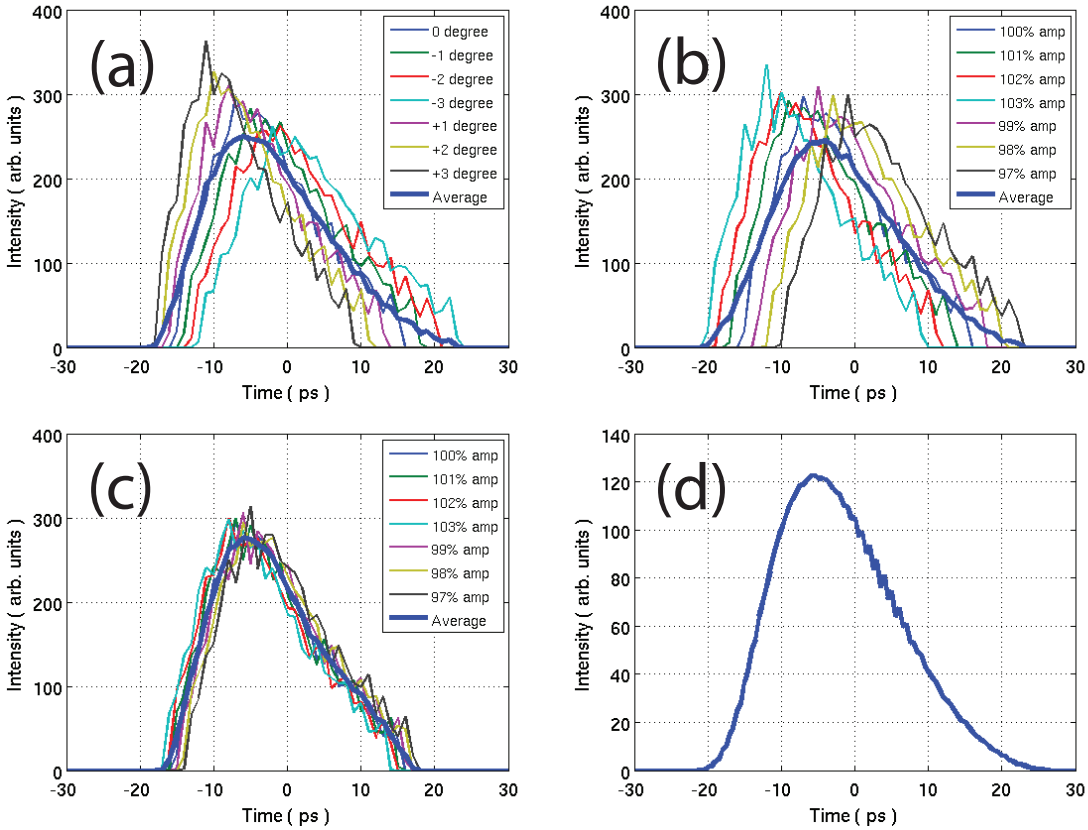

Figure 6.10: The RF transient effect on the slice emittance bunch length measurement. a) the bunch phase transient effect, b) the SRF1 cavity amplitude transient effect, c) the SRF2 cavity amplitude transient effect, d) the entire RF transient effect with the assumption that the buncher, SRF1 and SRF2 transient effects are independent of each other.

possible to fix the beam orbit by changing the corrector currents, it is too time consuming to practice it. Therefore, we switched to phasing the RF cavities by the arrival time. Naively speaking, the minimal arrival time corresponds to the maximum energy gain. This is true for the ultra-relativistic case, but is not true when β is only 0.8. Because the beam is not ultra-relativistic, thus it will gain and lose energy inside the RF cavity even at the maximum energy gain. If the BPM used to detect the arrival time is infinite far away from the the cryomodule, phasing the RF cavities by the minimum arrival time is equivalent to phasing

them by the maximum energy. However, the BPM is only 2 to 3 meters away from the last SRF cavity of the cryomodule, so that we need to apply corrections to insure that the phases are on-crest.

We performed GPT simulations to simulate the difference between phasing the RF cavities by the arrival time and the maximum energy gain. For the buncher, its voltage is relatively low compared to the gun HV (350 kV), usually 50 kV; phasing it by the minimum arrival time and maximum energy gain turns out to give almost the same on-crest phase, the error is within 0.5 degree. We still phase the buncher by the minimum BPM arrival time. For the SRF cavities, their voltages are usually on the order of 1000 kV, about three time large compared to the gun HV (350 kV) and the difference between the two methods are noticeable. When the SRF cavity voltages are set to 1395, 825, 1100, 1100, 1100 kV, the phase corrections are -6.5, -1.5, -1.5, -1.5, -4.0 degree according to the GPT simulation as shown in Fig. 6.11 and Fig. 6.12. These phase corrections are different at different SRF cavity voltages.

We compared the bunch lengths between the two phasing methods, it turned out that the phasing method would contribute to 20% discrepancy in the bunch length measurement. When the SRF cavities work in the close-to-bunching/debunching mode, it will compress/elongate the bunch. When we phase the SRF cavities by the minimum arrival time, the SRF cavities work in the slightly debunching mode, and this is enough to elongate the bunch length by 20% [Fig. 6.13].

After we fixed all these issues, we were able to make the bunch length 8 ps rms instead of the 15 ps rms [10].

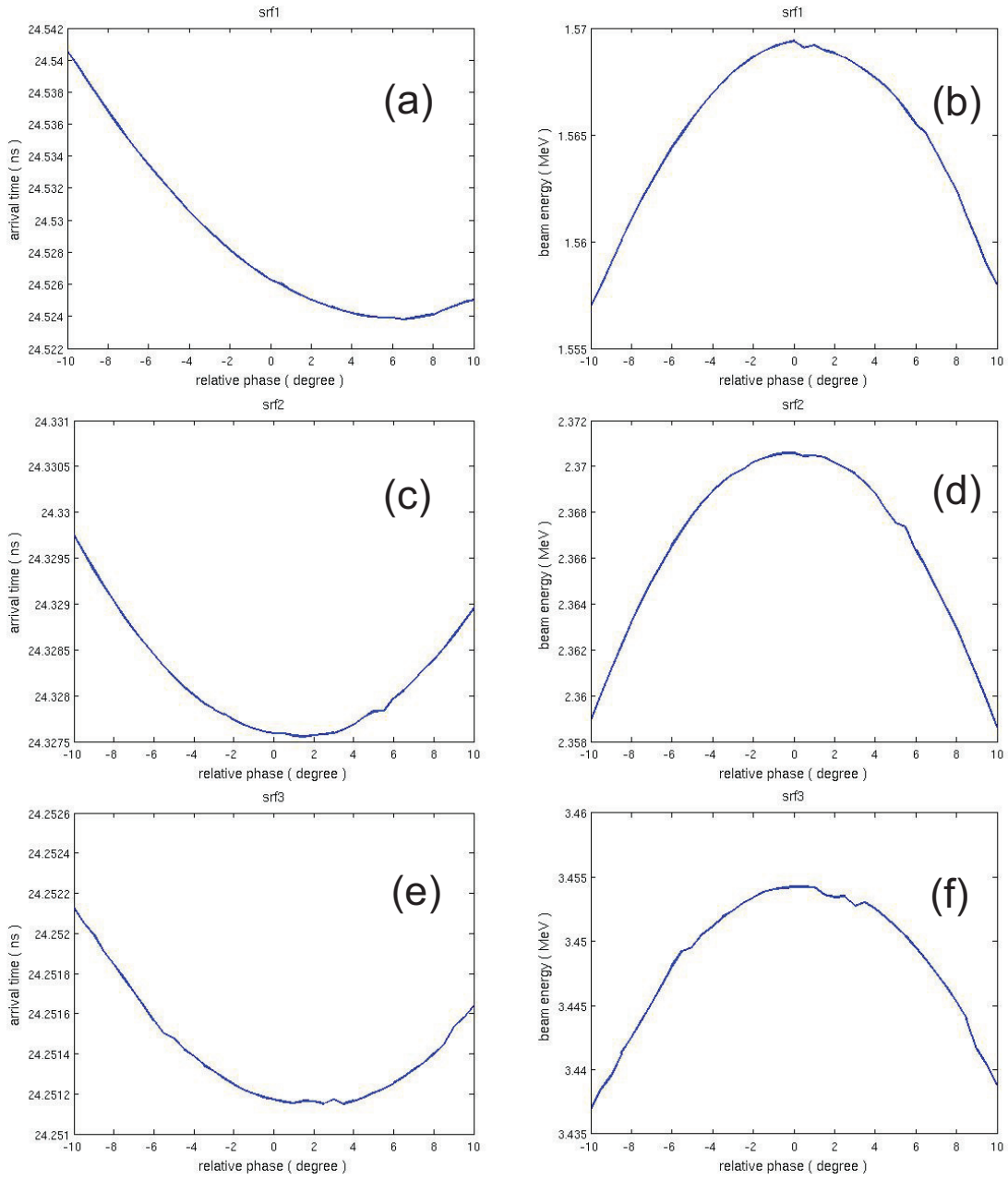

Figure 6.11: The RF phase difference between phasing by the minimum arrival time and maximum energy gain. a), b), SRF cavity 1 phasing by the minimum arrival time and maximum energy gain, c), d), SRF cavity 2 phasing by the minimum arrival time and maximum energy gain, e), f), SRF cavity 3 phasing by the minimum arrival time and maximum energy gain.

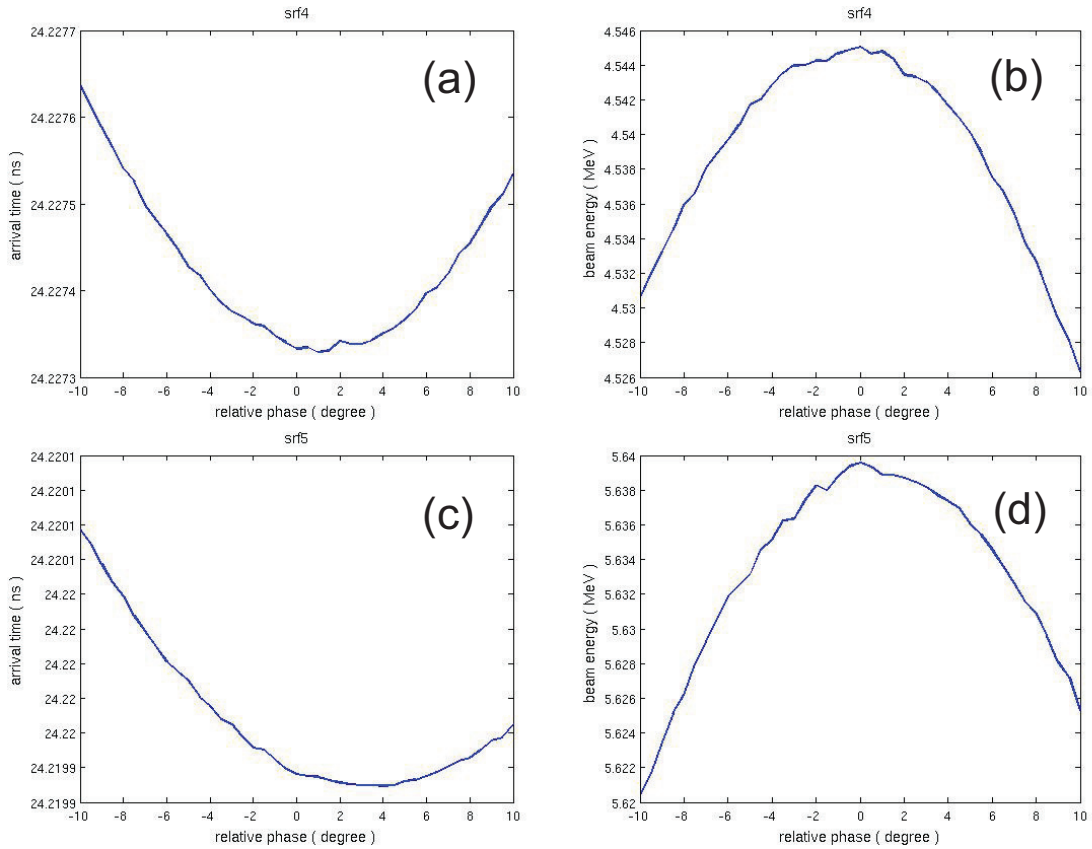

Figure 6.12: The RF phase difference between phasing by the minimum arrival time and maximum energy gain. a), b), SRF cavity 4 phasing by the minimum arrival time and maximum energy gain, c), d), SRF cavity 5 phasing by the minimum arrival time and maximum energy gain.

6.5.4 The entire elongation effect

The contributions from the buncher strength, the RF transient effect, and the RF phasing effect are summerized in Table. 6.3. The buncher strength and the RF phasing effect are additive, and the RF transient smears out the average measurement. Thus, we can obtain the entire elongation effect

$$\sigma_{\tau}^{\text{exp}} = (\sigma_{\tau,\,\text{buncher}} + \Delta\sigma_{\tau,\,\text{SRF phasing}}) \otimes \Delta\sigma_{\tau,\,\text{RF transient}} \tag{6.9}$$

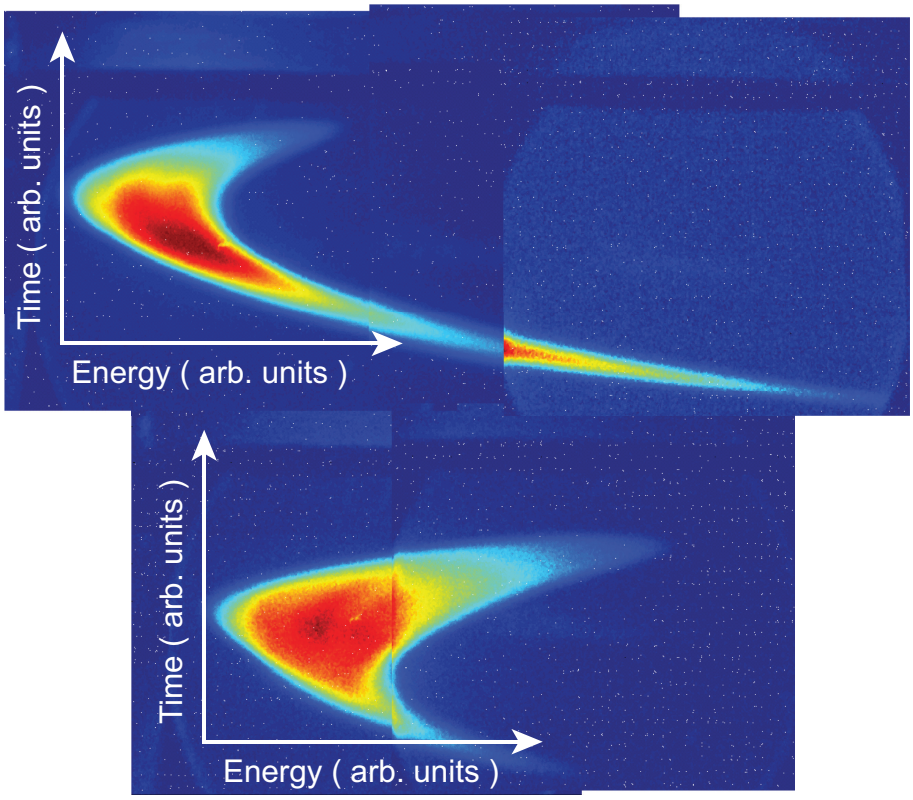

Figure 6.13: The time-resolved energy spread measured in the C2 section. a) phase the SRF cavities by the minimum arrival time, b) phase the SRF cavities by the minimum arrival time with phase corrections.

Table 6.3: The combination of the elongation effects

Effects	Elongation percent (%)	Bunch length (ps rms)
Buncher	80	12
RF transient	50	4
SRF phasing	20	2

where σ_τ^{exp} is the experimental measured bunch length, $\sigma_{\tau,\,\text{buncher}}$ is the bunch length at lower buncher voltage, $\Delta\sigma_{\tau,\,\text{RF transient}}$ is the artificial elongated bunch length, $\Delta\sigma_{\tau,\,\text{SRF phasing}}$ is the elongated bunch length from the SRF phasing, $\otimes$ stands for the convolution. After counting all these effects, the experimental measured bunch length from Eq. 6.9 is 15 ps rms and close to the theoretical prediction 15 ps rms. After applying corrections, we are able to produce bunch lengths 8 ps rms, that will be discussed in the next chapter.

6.6 Acknowledgments

We would like to acknowledge the colleagues continuously working on this project. This work was supported by the NSF award DMR-0807731.

BIBLIOGRAPHY

[1] I. V. Bazarov and C. K. Sinclair, "Multivariate optimization of a high brightness dc gun photoinjector", Phys. Rev. ST Accel. Beams **8**, 034202 (2005).

[2] I. V. Bazarov, B. M. Dunham, and C. K. Sinclair, "Maximum Achievable Beam Brightness from Photoinjectors", Phys. Rev. Lett. **102**, 104801 (2009).

[3] I. V. Bazarov, A. Kim, M. N. Lakshmanan, and J. M. Maxson, "Comparison of dc and superconducting rf photoemission guns for high brightness high average current beam production", Phys. Rev. ST Accel. Beams **14**, 072001 (2011).

[4] B.E. Carlsten, "New photoelectric injector design for the Los Alamos National Laboratory", Nucl. Instrum. Meth. A **285** 313-319 (1989).

[5] K. J. Kim, "Rf and space-charge effects in laser-driven rf electron guns", Nucl. Instrum. Meth. A **275**, 201-218 (1989).

[6] S. Zhou, D. G. Ouzounov, H. Li, I. Bazarov, C. Sinclair, and F. W. Wise, "Efficient temporal shaping of ultrashort pulses with birefringent crystals", Appl. Opt. **46**, 8488 (2007).

[7] I. V. Bazarov, D. G. Ouzounov, B. M. Dunham, S. A. Belomestnykh, Y. Li, X. Liu, R. E. Meller, J. Sikora, C. K. Sinclair, F. W. Wise, and T. Miyajima, "Efficient temporal shaping of electron distributions for high-brightness photoemission electron guns", Phys. Rev. ST Accel. Beams **11**, 040702 (2008).

[8] ASTRA, http://tesla.desy.de/ lfroehli/astra/.

[9] GPT, http://www.pulsar.nl/gpt/.

[10] Cornell ERL Elog, https://webdb.lepp.cornell.edu/elog/ERL+L0/.

[11] A. W. Chao, and M. Tigner, "Handbook of Accelerator Physics and Engineering", World Scientific, (2009).

[12] K. Smolenski, ERL Phase II, A4 EMS Slit System, Cornell University, (2007).

[13] J. Dobbins, EMS Charge Amplifier, Cornell University, (2012).

CHAPTER 7

THE SLICE EMITTANCE OF THE CORNELL ENERGY RECOVERY LINAC PHOTOINJECTOR AT NEAR-0 PC, 80 PC BUNCH CHARGE, 5 MEV BEAM ENERGY

The slice emittance of the Cornell Energy Recovery Linac (ERL) photoinjector was measured by the two-slit method and a vertical deflecting cavity at 5.7 MeV beam energy. We demonstrate the measurement technique by measuring the slice emittance at the near-zero bunch charge and then measured the 0.8 mm-mrad vertical emittance at 80 pC bunch charge in 2011. The core of the electron beam has 70% of the particles and has the core emittance 0.3 mm-mrad. This was a large improvement from the 3.6 mm-mrad emittance measured in 2010 and was reported as one milestone of the Cornell ERL.

7.1 Introduction

Free-electron lasers (FELs) and energy recover linacs (ERLs) are the next generation light sources which produce high brightness x-ray beams from diffraction-limited electron beams, the average brightness is expected to be at least one order of magnitude greater than the storage ring based x-ray sources, either in existence or under construction. The transverse emittance is extremely important in the hard x-ray regime, and ultra-low transverse emittance is required to achieve the the targeted performance. Most of these facilities use photoinjectors to produce electron beams, and the initial emittance from photoinjectors determines the performance of the entire facilities [2]. The normally quoted emittance is the projected emittance, which is integrated over the time domain; while the slice emittances is the time-resolved emittance. Because the emittance of the

photoinjector is a complicated interplay of the incident laser beam profile, the field in the gun, the emittance compensation solenoids and the time-dependent Radio Frequency (RF) focusing, therefore the slice emittance can help to reveal the electron beam dynamics and also guide to further optimize the emittance [3].

The transverse emittance is normally characterized by the quadrupole scan technique at hundreds MeV beam energy, when the transverse space charge effect of the beam is freezed, and the beam size is usually monitored by optical transition radiation view screens and wire scanners [4, 5, 6, 7]. The first slice emittance measurement was demonstrated at 0.4 nC bunch charge and ~4 MeV beam energy by the combination of this technique and the energy selection in a dispersion section, where the time slice is selected by a slit in the dispersion section for an energy chirped bunch; a phosphorous screen was used to image the beam. It also demonstrated the linear space charge emittance compensation with a focusing solenoid [4, 8]. Modern facilities use RF cavities/structures to enable the time-resolved measurements in a more generic way, which make the both the time-resolved emittance and energy spread measurements possible [5, 6, 7, 9]. The slice emittance was measured at the hard x-ray FEL facility, the linac coherent light source (LCLS) at SLAC National Accelerator Laboratory in the United States, by using the quadrupole scan technique and a transverse RF deflector. The slice emittance was measured at 135 MeV beam energy at 20 pC and 1 nC bunch charge to be ~0.2 mm-mrad and ~1 mm-mrad respectively, with 1 ps resolution, <6 keV rms slice (intrinsic) energy spread at 1 nC (which could be limited by the instrument resolution); good agreements were found between experiments and simulations for the core part of the beam [6, 7]. Slice emittance phase space distribution was also measured at the soft x-ray free-electron laser in Hamburg (FLASH) from Deutsches Elektronen-Synchrotron

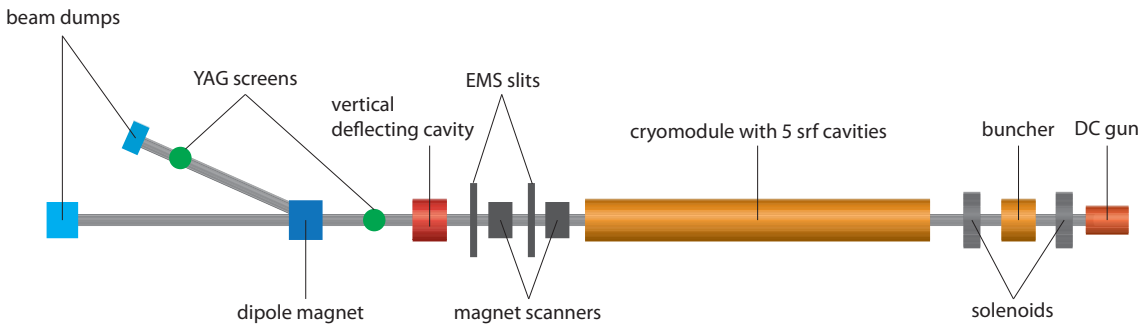

Figure 7.1: The Cornell ERL photoinjector slice emittance measurement scheme (not to the scale). The beam direction is from the right to the left.

(DESY) in Germany in the operating condition, by combining the quadrupole scan tomography and a transverse deflecting structure, at 677 MeV beam energy and 0.5 nC bunch charge with ~30-fs root-mean-square (rms) time resolution. It was found that the high-intensity core which contributes to the lasing process has a much smaller transverse emittance 2 to 3 mm-mrad compared to the much larger projected transverse emittance. The time-resolved energy spread was measured to be much larger than the values measured from the photoinjector section and could be estimated as its instrument resolution [5]. Both the SLAC and FLASH produce electrons with energy larger than hundreds of MeV and the transverse space charge effect on the emittance measurement could almost be ignored [10].

Although the quadrupole scan is established in the transverse emittance characterization, careful optical modeling is required for such a technique; while the space charge effect can still contribute to the emittance measurement even at hundreds MeV beam energy [5, 6]. For the Cornell ERL photoinjector, the electron beam is produced from a direct current (DC) gun, thus it has lower energy (350 kV to 750 kV) compared to RF guns (several MeV) and the transverse space charge effect dominates the emittance growth [11]. Furthermore,

the beam energy produced from the Cornell ERL photoinjector is designed to be several MeV instead of hundreds MeV, thus the transverse space charge effect cannot be ignored in the quadrupole scan emittance measurement except for the smallest bunch charges (less than a pC). Therefore we use the two-slit technique to measure the emittance phase space distribution: the first slit is used to select the beam position and the second slit is used to select the transverse beam momentum, a Faraday cup or a view screen is used to measure the beam intensity after these two slits; after scanning the phase space, the emittance phase space distribution can be retrieved. Meanwhile, by correctly designing the width of these slits, the transverse space charge effect from each beamlet after these slits is negligible in practical experiments. Details of the double-slit emittance measurement system (EMS) are described in [12]. A normal-conducting RF vertical deflecting cavity (VDC) downstream is used to streak the beam vertically and to provide the time-resolved beam along the vertical direction [9]. Together with the two-slit emittance diagnostic, we are able to measure the time-solved vertical emittance, i.e., the vertical slice emittance; together with the dipole magnet, we are also able to measure the time-resolved energy spread on the view screen downstream the dipole magnet.

Here we present the slice emittance measurements of the Cornell ERL photoinjector at beam energy 5 MeV and bunch charge 80 pC, which corresponds to the high-flux mode of the proposed x-ray facility. We demonstrate this diagnostic by measuring the time-dependent RF focusing at the near-zero bunch charge at 5 MeV beam energy, where the instrumental temporal resolution is measured to be 380-fs rms at 5 MeV beam energy. Then we continue with the slice emittance measurements at 80 pC bunch charge, where the projected emittances is 0.8 mm-mrad, which is the smallest emittance has ever been achieved from a dc

gun driven photoinjector at the usable bunch charge. The core part of the beam contains 70% of the electrons and has 0.3 mm-mrad emittance, this was reported as one milestone of the Cornell ERL [1].

7.2 The experiment setup

The Cornell ERL is designed to be operated at 5 GeV at 100 mA current in the high-flux mode, that correspond to 77 pC bunch charge. The projected experiment is described in the previous chapters. In the slice emittance measurement, we replace the Faraday cup with the VDC and a view screen to enable the time-resolved capabilities.

A VDC (z=11.02 m) operating at 5 kHz macro-pulse mode and in the TM110 mode streaks the beam in the vertical direction and is used to enable the time-resolved measurements. An insertable RF shielded Faraday cup (z=11.39 m) is located downstream of the VDC and is used to measure the beam current. A home-made charge amplifier is used to amplify the current. The data acquisition (DAQ) rate is up to 2 kHz. A Yttrium aluminium garnet (YAG) screen (z=12.68 m) is used as the scintillator to monitor the electron beam profile, and a CCD camera (Point Grey, FL2-03S2C) with image lenses is used to collect the data. In a projected transverse emittance measurement, the horizontal/vertical slits and the Faraday cup are inserted into the beam pipe to measure the vertical/horizontal projected emittance, a 100×100 ($x \times p_x$ or $y \times p_y$) data set takes less than ten seconds and the analysis can be done within the same time scale. While in the slice emittance measurement, the horizontal slits and the YAG screen are inserted and the VDC is turned on to perform the vertical slice emittance mea-

surement. A 120×120×300 ($y \times p_y \times t$) data set takes sixty minutes, more than 20,000 images from the CCD camera are saved to a computer and used for the data analysis off-line, which takes another sixty minutes. Some sample raw data are shown in Fig. 7.2: they are the images on the YAG screen at a specific phase space point (y^{sample},p_y^{sample}), the vertical axis y_{raw} is the time axis t when the VDC is turned on, and the horizontal axis x_{raw} needs to be integrated out; then we obtain the time intensity at this specific phase space point (y^{sample},p_y^{sample}). The slice emittance is retrieved by combining every point in the phase space. Background noise exists in Fig. 7.2(a), these noise comes from the scattered light and contributes to measurement error, and it needs to be removed. We first fit the signal with an ellipse, and calculating the background noise outside it. If the signal inside the ellipse is below the background noise, we set it to zero. In this way, we remove the background noise. Then we obtain the raw data after this background noise reduction, as depicted in Fig. 7.2(b). We apply this procedure to every raw image before the next step analysis, which is similar to the analysis of the projected emittance with the additional time dimension.

With the fast projected emittance diagnostic, we are able to do real-time multivariate optimization for the emittance compensation section, which includes scanning the solenoid currents and the buncher voltage. Both the transverse projected and slice emittance are average measurements and the beam stability is assumed throughout the data acquisition process. However, we do observe this kind of fluctuation from one measurement to another.

In the slice emittance measurement, the fluorescence light produced on the YAG screen is reflected by a silicon mirror and then collected by the CCD camera. The YAG screen is imaged by an image lens with f-number 20 to the CCD

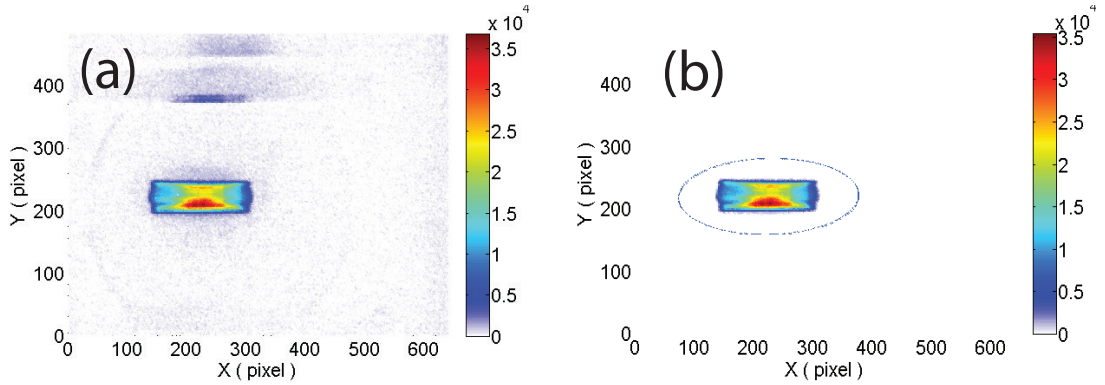

Figure 7.2: The sample raw data of the slice emittance measurement, the images on the YAG screen. a) the raw image before removing the background noise, the circle outside is the beam pipe, b) the raw image after removing the background noise. The blue ellipse is obtained by calculating the second moment of the signal distribution. The color map is the same for the emittance results.

camera, where each pixel corresponds to 55×55 μm ($\Delta l_{\text{pixel}} \times \Delta l_{\text{pixel}}$) of the view screen and this defines our spatial resolution. The DAQ rate of the slice emittance measurement is 3 Hz and is limited by the data write speed on the hard disk drive and the networking speed. It may be further limited by the exposure time of the CCD which is 67 ms in our experiments. The electron beams are deflected by the VDC, and results in a streak on the CCD camera, where the different vertical position corresponds to the different arrival time. The deflection length of the beam (Δy) is proportional to the effective VDC voltage (V_y) and and the RF offset angle ($\Delta\phi$) from the zero-crossing point, and inversely proportional to the beam momentum.

$$\begin{aligned} \Delta y &= \Delta l_{\text{pixel}} N_{\text{pixel}} = \Delta y' L_{ds} \\ &= \frac{p_y}{p_z} L_{ds} \approx \frac{eV_y}{c|p|} L_{ds} \sin\Delta\phi \approx \frac{eV_y}{c|p|} L_{ds} \xi_t \Delta\tau, \end{aligned} \tag{7.1}$$

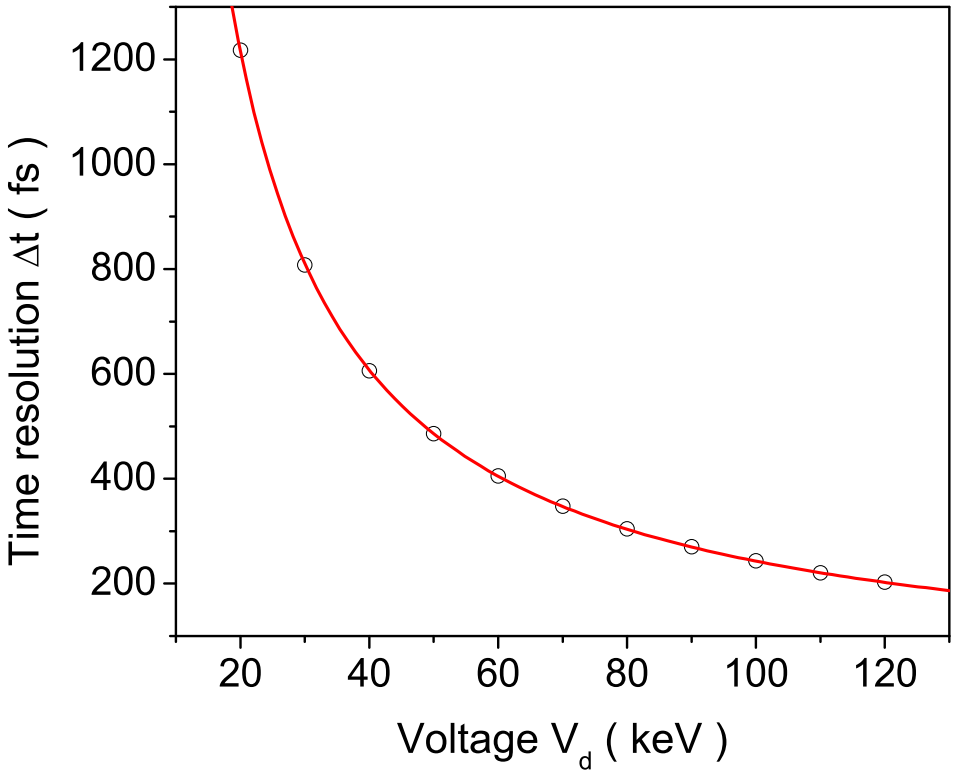

Figure 7.3: The VDC time resolution calibration on the YAG screen at 5.3 MeV beam energy, the red curve is the best fit of Eq. (7.2).

where N_{pixel} is the number of pixels, $\Delta y'$ is the deflection angle, L_{ds} is the distance between the VDC and the YAG screen, p_y is the change of the transverse momentum after the VDC (a few keV/c), p_z is the longitudinal momentum (several MeV/c), c is the speed of light, p is the total momentum, ξ_τ is 2.1 ps/deg at 1.3 GHz RF frequency, and $\Delta\tau$ is the bunch length. Good linearity between the RF offset angle and the deflection angle was observed in the experiment. Then we calibrated the time resolution per pixel (Δt) on the view screen at different VDC voltage (V_d) at 5.3 MeV/c beam momentum, as the graph shown in Fig. 7.3. The time resolution per pixel is inverse proportional to the VDC voltage, as we expected from Eq. (7.2); it is 200 fs/pixel at 120 keV and decreases as the VDC

voltage is reduced,

$$\Delta t \approx \frac{\Delta\tau}{N_{\text{pixel}}} = \frac{\Delta l_{\text{pixel}}}{\xi_\tau L_{ds}} \frac{c|p|}{eV_y}. \tag{7.2}$$

However, the time resolution of the slice emittance measurement also needs to account for the timing jitter from the synchronization between the RF and the laser system, which is measured by an Agilent E5052B Signal Source Analyzer to be 300 fs rms when integrating from 10 Hz to 10 MHz. We measured the instrument time resolution experimentally by operating the VDC at 120 keV and inserting in both the horizontal slits to reduce the beam width at the near-zero bunch charge. The initial laser pulses have 2-ps fwhm duration and the buncher operates in the bunching mode to compress the bunch length. The bunching phase is -90° from the on-crest phase. Then we scanned the buncher voltage to minimize bunch length on the YAG screen. The minimal length is measured to be 380-fs rms (or 1-ps fwhm). This is our instrument time resolution, which is limited by the width of the slit. This resolution is sufficient for most of our beam experiments presented here, where the bunch length is usually more than a few ps rms.

It was also found that we need to compensate the vertical momentum introduced by the second horizontal slit: the second horizontal slit selects beamlet with transverse momentum p_y^{slit}, and the total transverse momentum after the VDC is $p_y + p_y^{\text{slit}}$ instead of p_y, thus this transverse momentum imposed by the second horizontal slit has to be removed in the data analyzing process later in order to avoid the artificial effect on the vertical slice emittance measurement. Experimentally, we know every p_y^{slit} in the phase space scanning process, and we can compensate the displacement on the YAG screen by adding a term

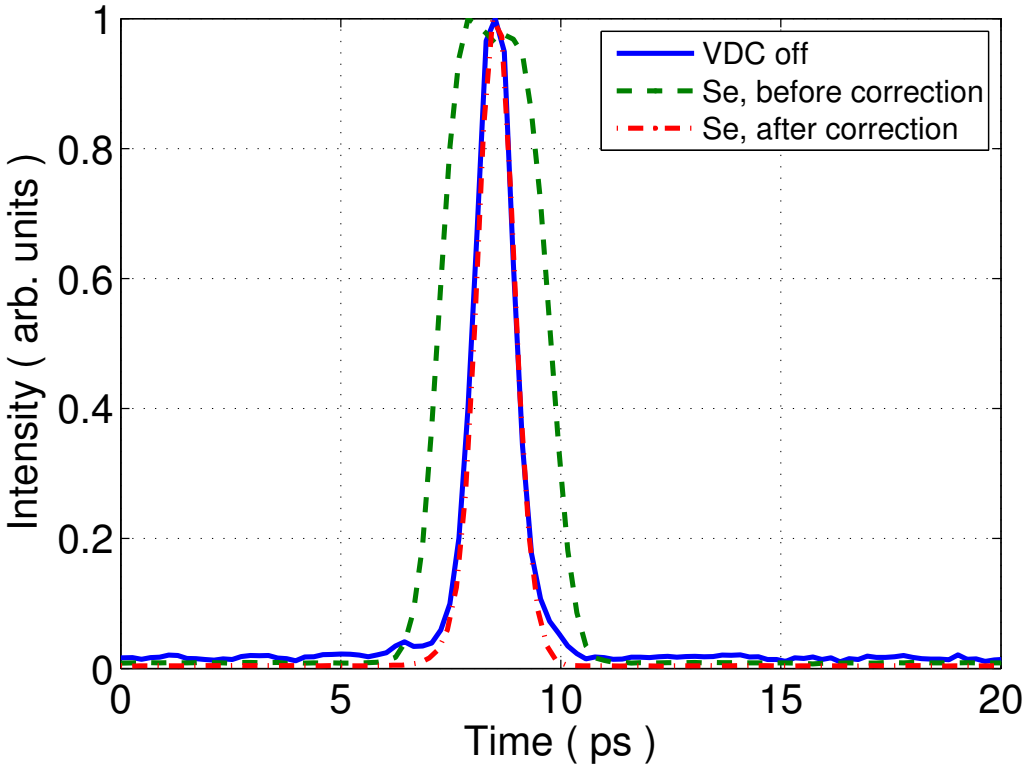

Figure 7.4: The measured time resolution of the slice emittance with the VDC operating at 120 keV, and 5 MeV beam energy. Se stands for slice emittance measurement.

$$\Delta y^{\mathrm{sc}} = -\Delta y^{\mathrm{slit}} = -\frac{p_y^{\mathrm{slit}}}{p_z} L_{ds} \approx -\frac{p_y^{\mathrm{slit}}}{p} L_{ds}, \tag{7.3}$$

where Δy^{sc} is the second slit compensation displacement on the YAG screen and this correction is applied to every point in the vertical emittance phase space. This correction outcome is illustrated in Fig. 7.4: the solid line is the beamlet integrated over the vertical axis, with the VDC off, which represents the spatial resolution of the imaging system of the YAG screen; the dashed line is the retrieved time intensity from the slice emittance measurement, without the second slit transverse momentum correction, it gives an artificially elon-

gated bunch length. The dot dashed line is the time intensity retrieved from the same slice emittance measurement, with the transverse momentum correction applied, it almost overlaps with the solid line, which implies that the instrument time resolution is limited by the width of the slits; that is the 380-fs rms (or 1-ps fwhm) when the VDC operates at 120 keV voltage at 5.3 MeV beam energy.

7.3 The slice emittance from the time-dependent RF focusing

It is well known that RF cavities have time-dependent RF focusing. The emittance growth from this effect is proportional to the beam size squared (σ_x^2) and also the bunch length (σ_t) for a DC gun and bunch length squared (σ_t^2) for a RF gun, therefore bunches with small volume are preferred when they enter the RF cavities [3, 15]. Here we will show the analytical formula of the transverse emittance growth from the time-dependent RF focusing in the ultra-relativistic case and also present experiments to show that this result can also be applied to the situations when the beam is near-relativistic.

7.3.1 The transverse emittance growth from the time-dependent RF focusing

The SRF cavities at the Cornell ERL photoinjector have two cells, to the first order, the electric field can be approximated by

$$E_z(z,t) = E_0 \sin(kz)\sin(\omega t + \phi_0). \tag{7.4}$$

where E_0 is the peak electric field, $k = 2\pi/\lambda$ is the RF wave number, λ is the RF wavelength, c is the speed of light, $\omega = ck$ is the RF frequency, ϕ_0 is the initial phase of the bunch when it enters the RF cavities, $\phi_0 = 0, -\pi/2$ correspond to the on-crest and bunching phase, respectively. $t = \frac{1}{c}\int \frac{1}{\beta} dz$, where β is the relative speed regards to the speed of light, $\beta = \frac{v}{c}$. In the ultra-relativistic case, $\beta \approx 1$, therefore, $t = \frac{z}{c}$, and Eq. (7.4) becomes

$$E_z^e(z) = E_0 \sin(kz)\sin(kz + \phi_0), \tag{7.5}$$

it is also equivalent to write Eq. 7.5 as

$$E_z^e(t) = E_0 \sin(\omega t)\sin(\omega t + \phi_0), \tag{7.6}$$

this is the electric field observed by the electrons traveling at the speed of light.

The time-dependent RF focusing comes from the radial electric field E_r and the axial magnetic field B_θ. The radial component of the Lorentz force on the bunch can be obtained by using the paraxial approximation,

$$\begin{aligned} F_r &= -e(E_r - \beta c B_\theta) = e(-\frac{r}{2}\frac{\partial}{\partial z}E_z - \beta\frac{r}{2c}\frac{\partial}{\partial t}E_z) \\ &= \frac{ekE_0}{2}\sin(2\omega t + \phi_0)r. \end{aligned} \tag{7.7}$$

If we assume that the beam is rigid (diameter and length do not change), the equation of motion for the radial component of the momentum ($p_r = \gamma mc\beta_r$) is

$$\frac{d}{dt}p_r = (\frac{d}{dt}\gamma)mc\beta_r + \gamma mc(\frac{d}{dt}\beta_r) = F_r. \tag{7.8}$$

In the ultra-relativistic case, the energy gain from one single RF cavity is usually several MeV, while the beam energy is at least tens of MeV, therefore, the term $(\frac{d}{dt}\gamma)mc\beta_r$ is much smaller than the term $\gamma mc(\frac{d}{dt}\beta_r)$, and can be ignored. Then Eq. (7.8) becomes

$$\frac{d}{dt}\beta_r \approx \frac{1}{mc}\frac{F_r}{\gamma}. \tag{7.9}$$

We can obtain β_r after the RF cavity by integrating Eq. (7.9),

$$\beta_r = \beta_r^0 + \frac{1}{mc}\int \frac{F_r}{\gamma}dt, \tag{7.10}$$

where γ can be obtained by integrating the acceleration force in the cavity from 0 to λ for a two-cell cavity,

$$\begin{aligned} \gamma &= \frac{E}{mc^2} = \gamma_0 + \frac{1}{mc^2}\int_0^{s(t)} eE_z(z)dz \\ &= \gamma_0 + \frac{eE_0}{2mc}[\cos\phi_0 \cdot t + \frac{1}{2\omega}\sin(2\omega t + \phi_0) - \frac{1}{2\omega}\sin\phi_0], \end{aligned} \tag{7.11}$$

where $s(t)$ is the position of the bunch in the cavity at the time t, γ_0 is the Lorentz factor of the beam before it enters the RF cavity, plug Eq. (7.7) and Eq. (7.11) into Eq. (7.9), we can obtain

$$\begin{aligned}\frac{d}{dt}\beta_r &= \frac{eE_0kr}{2mc} \\ &\times\frac{\sin(2\omega t+\phi_0)}{\gamma_0+\frac{eE_0}{2mc}[\cos\phi_0\cdot t+\frac{1}{2\omega}\sin(2\omega t+\phi_0)-\frac{1}{2\omega}\sin\phi_0]},\end{aligned} \tag{7.12}$$

define $\kappa = \gamma_0 - \frac{eE_0}{4m\omega c}\sin\phi_0$, and reorder the second term in Eq. (7.12), then do the Taylor expansion for the hyperbolic function around 0,

$$\begin{aligned}&\frac{1}{\kappa}\frac{\sin(2\omega t+\phi_0)}{1+\frac{eE_0}{2mc\kappa}[\cos\phi_0\cdot t+\frac{1}{2\omega}\sin(2\omega t+\phi_0)]} \\ =\ &\frac{1}{\kappa}\sin(2\omega t+\phi_0)(1-\frac{eE_0}{2mc\kappa}[\cos\phi_0\cdot t+\frac{1}{2\omega}\sin(2\omega t+\phi_0)]),\end{aligned} \tag{7.13}$$

integrate this term from 0 to $T = \frac{2\pi}{\omega}$; let us assume the energy gain from one two-cell RF cavity is $\gamma_c mc^2$ and $\beta_r^0 = 0$, we obtain

$$\frac{1}{\kappa}\frac{\pi\gamma_c c\cos(2\phi_0)}{2\kappa\lambda\omega^2}. \tag{7.14}$$

Then we can write the transverse momentum after the cavity as

$$\beta_r = -\frac{\gamma_c^2}{4\gamma_0^2}\frac{\cos(2\phi_0)}{(1-\frac{\gamma_c}{4\pi\gamma_0}\sin\phi_0)^2}\frac{r}{\lambda} = -\frac{\gamma_c^2}{4\gamma_0^2}f(\phi_0)\frac{r}{\lambda}, \tag{7.15}$$

for the on-crest case, the time-dependent RF fields focus the beam in the transverse domain, which is observed in experiments and simulations. We can obtain the horizontal and vertical $\beta_{x/y}$ by replace the subscript r with x/y; and because $\beta_z \sim 1$, therefore $r' \approx \beta_r$. This term describes the time-dependent RF

focusing: every slice of the phase space of (y, y') rotates differently according to it phase ϕ_0, its volume is conserved. Therefore, the slice emittance does not change when the beam travels through the RF cavity. However, the projected emittance increases because different slice of the phase space rotates differently, and the longer the bunch length, the larger the misalignment and the larger projected emittance. The projected vertical emittance is calculated later in this section.

Now we can calculate the vertical emittance growth ϵ_y^{RF} from the time-dependent RF focusing.

$$\begin{aligned}\epsilon_y^{\mathrm{RF}} &= \sqrt{\langle y^2\rangle\langle y'^2\rangle - \langle yy'\rangle^2} \\ &= \langle y^2\rangle \frac{\gamma_c^2}{4\gamma_0^2}\frac{1}{\lambda}\sqrt{\langle f(\phi_0)^2\rangle - \langle f(\phi_0)\rangle^2}. \end{aligned} \tag{7.16}$$

Let us consider the on-crest situation, where $\phi_0 \sim 0 + \phi$, the finite phase corresponds to the finite bunch length. Assume $\varrho = \frac{\gamma_c}{4\pi\gamma_0}$, we can expand $f(\phi_0)$ around 0 and calculate the terms $f(\phi_0)$ and $f(\phi_0)^2$,

$$\begin{aligned} f(\phi_0) &= 1 + 2\varrho\phi + (-2 + 3\varrho^2)\phi^2 + (-\frac{13\varrho}{3} + 4\varrho^3)\phi^3 \\ &+ (\frac{2}{3} - 7\varrho^2 + 5\varrho^4)\phi^4 + O(\phi^5), \\ f(\phi_0)^2 &= 1 + 4\varrho\phi + (-4 + 10\varrho^2)\phi^2 + (-\frac{50\varrho}{3} + 20\varrho^3)\phi^3 \\ &+ (\frac{16}{3} - \frac{130\varrho^2}{3} + 35\varrho^4)\phi^4 + O(\phi^5), \end{aligned}$$

if we assume that the bunch length is ϕ_τ and its intensity obeys the uniform distribution with centroid position 0, then we can simplify the term $\langle f(\phi_0)^2\rangle$ –

$\langle f(\phi_0)\rangle^2$,

$$\begin{aligned}\langle f(\phi_0)^2\rangle - \langle f(\phi_0)\rangle^2 &= 4\varrho^2\langle\phi^2\rangle + (\frac{12}{3} - \frac{116}{3}\varrho^2 + 25\varrho^4)\langle\phi^4\rangle \\ &- (4 - 12\varrho^2 + 9\varrho^4)\langle\phi^2\rangle^2, \end{aligned} \tag{7.17}$$

notice that $\langle\phi^4\rangle = \frac{1}{80}\phi_\tau^4$, $\langle\phi^2\rangle^2 = \frac{1}{144}\phi_\tau^4$ for the uniform distribution, we can get the emittance growth from the time-dependent RF focusing, ϵ_y^{RF},

$$\epsilon_y^{\mathrm{RF}} = \frac{\gamma_c^2}{4\gamma_0^2}\frac{1}{\lambda}\langle x^2\rangle\sqrt{\kappa_1\sigma_\tau^2 + \kappa_2\sigma_\tau^4}, \tag{7.18}$$

where κ_1 and κ_2 depend on ϱ and can be calculated from the bunch intensity distribution and Eq.(7.17).

The transverse emittance growth from the RF time-dependent focusing is proportional to the initial beam size square $\langle x^2\rangle$ and the bunch length ϕ_τ in the near-relativistic regime for the dc gun, $\varrho \sim 0.1$, which is consistent with the emittance from a dc gun [3]; in the RF guns [11], $\epsilon_{ny}^{\mathrm{RF}} \propto \phi_\tau^2$, which is consistent with the result from a RF gun[15]. We can also see that the transverse emittance growth becomes smaller as the initial beam energy increases, this is because that the beam gets more rigid and the radial component of impulse cancels each other more within a RF period. This approximation works reasonably well for the first SRF cavity of the Cornell ERL photoinjector. In the real experiment, because of the thermal energy, the gun focus, and the solenoid focus, β_r^0 has some finite value and is not 0. Therefore, the non-zero β_r^0 should be taken into account to get more accurate estimation. Another thing to notice is that the rigid

beam assumption does not always work. The time-dependent RF focusing not only focuses the beam transversely but also compresses the beam longitudinally near the on-crest values. After counting this effect, the emittance growth scales linearly with the energy gain from the RF cavity instead of quadratically. Never the less, this analytical expression of the emittance growth shows the correctly scaling with the beam size and bunch length of the electron beam.

From this result, we can see that small beam volume is preferred to control the transverse emittance growth from the RF cavities [3]. In experiment, this can be achieved by compressing the bunch length by the buncher and focusing the beam before it enters the cryomodule by solenoids. Now we will present slice emittance measurements to demonstrate this RF time-dependent focusing effect.

7.3.2 The slice emittance measurement of the time-dependent RF focusing

As we have shown, at the near-zero bunch charge, focusing the beam before the cryomodule can reduce the transverse emittance growth from the RF time-dependent focusing substantially. In this section, we measured the slice emittance of the Cornell ERL photoinjector at the near-zero bunch charge (in actuality less than 0.1 pC, that is called 'near-zero' to differentiate from the 80 pC bunch charge), where the measured projected emittance is a little larger compared to the thermal emittance from the photocathode and the slice emittance is almost exactly the same as the thermal emittance; the transverse emittance growth comes from the slice emittance misalignment from the RF cavities and

it agrees well with the numerical General Particle Tracer (GPT) simulation.

$$\epsilon_{nxy,\text{th}} = \sigma_{xy} \sqrt{\frac{\text{MTE}}{m_e c^2}}, \tag{7.19}$$

The initial laser pulses are shaped by three YVO_4 birefringent crystals to produce a near flat-top pulse with 33 ps fwhm pulse duration before it incident on the photocathode [13, 14]. The thermal emittance of the electrons is determined by the photon energy of the driven laser and the work function of photocathode, that give the mean transverse energy (MTE) of the electrons as Eq. (7.19) [3]. For the 520 nm photon energy and a GaAs photocathode, its MTE is 120 meV, which corresponds to 0.12 mm-mrad normalized transverse emittance for a 1 mm diameter beam on the cathode. Then the electrons are accelerated in the gun and go through the first solenoid, the buncher, the second solenoid before they enter the cryomodule. The machine setting is listed in Table. 7.1: the gun operates at 350 kV, a 1 mm pinhole was used to truncate the transverse Gaussian beam to provide the near flat-top distribution. The two solenoid currents are set to -2.43 and 2.05 A respectively, which correspond to -0.020 and 0.017 T magnetic peak on-axis field strength. The currents are opposite to each other to reduce the overall Larmour rotation from the solenoids. These currents were chosen to illustrate the time-dependent RF focusing: the beam size is reasonably small but can still receive enough RF time-dependent focusing which can be resolved by the two-slit EMS. The SRF cavity voltages are set to 1395, 825, 1100, 1100, 1100 kV which are the parameters optimized for the 80 pC bunch charge operation; the SRF cavity phases are -10, 0, 0, 0, 0 ° respect to the on-crest phase. The first SRF cavity phase is -10 ° from the on-crest value, that is one unintentional error from phasing the cavity by the arrival time measured by the beam position

monitors (BPMs).

The beam envelope evolutions are shown in Fig. 7.5. The beam is accelerated to 350 keV by the DC gun, then it is accelerated to 1.6 MeV after the first SRF cavity, and reaches 5.6 MeV beam energy after the cryomodule, as depicted in Fig. 7.5(a). Its bunch length is 8 ps rms after leaving the DC gun, and is compressed to 6 ps rms after the first SRF cavity increasing to 7 ps rms at the end of the cryomodule, as shown in Fig. 7.5(b). The beam size σ_y is 0.25 mm initially and keeps increasing, the second solenoid focuses it to 0.5 mm when it enters the first SRF cavity, and stabilizes to 0.5 mm at the first EMS slit, as in Fig. 7.5(c). In Fig. 7.5(d), the transverse emittance ϵ_{ny} is 0.13 mm-mrad just after the beam leaves the cathode. The solenoid focusing causes Larmour rotation, then it stabilizes to 0.13 mm-mrad, and begins to oscillate inside the first SRF cavity and increases to 0.16 mm-mrad, because the impulse from the time-varying field could not be canceled completely due to the energy gain from the SRF cavity. The transverse emittance growth from the other four SRF cavities is negligible because the beam energy increases and also the beam size becomes smaller. Keeping the beam volume small before it enters the RF cavities can reduce the emittance growth from the RF fields, although it is usually very challenging to achieve this goal when the space charge effect dominates the initial emittance growth at the higher bunch charge.

The beam energy is measured by a dipole magnet to be 5.2 MeV, which is not far from the simulated result 5.6 MeV, the discrepancy mainly comes from the calibration error of the SRF cavity amplitudes mentioned in the previous chapter. The measured projected emittance is depicted in Fig. 7.6(a), it has a similar look with the simulated projected emittance, the slight asymmetrical structure

Table 7.1: The Cornell ERL photoinjector settings for the near-zero bunch charge case. The RF phase values are respect to the on-crest values.

Components	Parameters	RF phases
Laser σ_τ	33 ps fwhm	
Laser $\sigma_{x/y}$	0.25 mm rms	
Cathode MTE	120 meV	
Gun HV	350 kV	
Iris size	1 mm	
Solenoid 1	-2.43 A	
Buncher	off	
Solenoid 2	2.05 A	
SRF1 cavity	1395 kV	-10°
SRF2 cavity	825 kV	0°
SRF3 cavity	1100 kV	0°
SRF4 cavity	1100 kV	0°
SRF5 cavity	1100 kV	0°
VDC	120 kV	

could come from the small misalignment of the elements in the beamline, such as the buncher, SRF cavities and solenoids, which can be improved by aligning these elements one by one. The vertical emittance ϵ_{ny} and vertical beam size σ_y are measured to be 0.16 mm-mrad and 0.50 mm respectively, which are very close to the simulation results 0.16 mm-mrad, 0.52 mm. Fig. 7.6(c) shows the beam intensity, the eight peaks from the YVO_4 shaping crystal can be observed clearly, the small spike in the middle comes from the undeflected beam in the extinction regime of the Pockels cell, which is usually more than 1,000,000:1 but

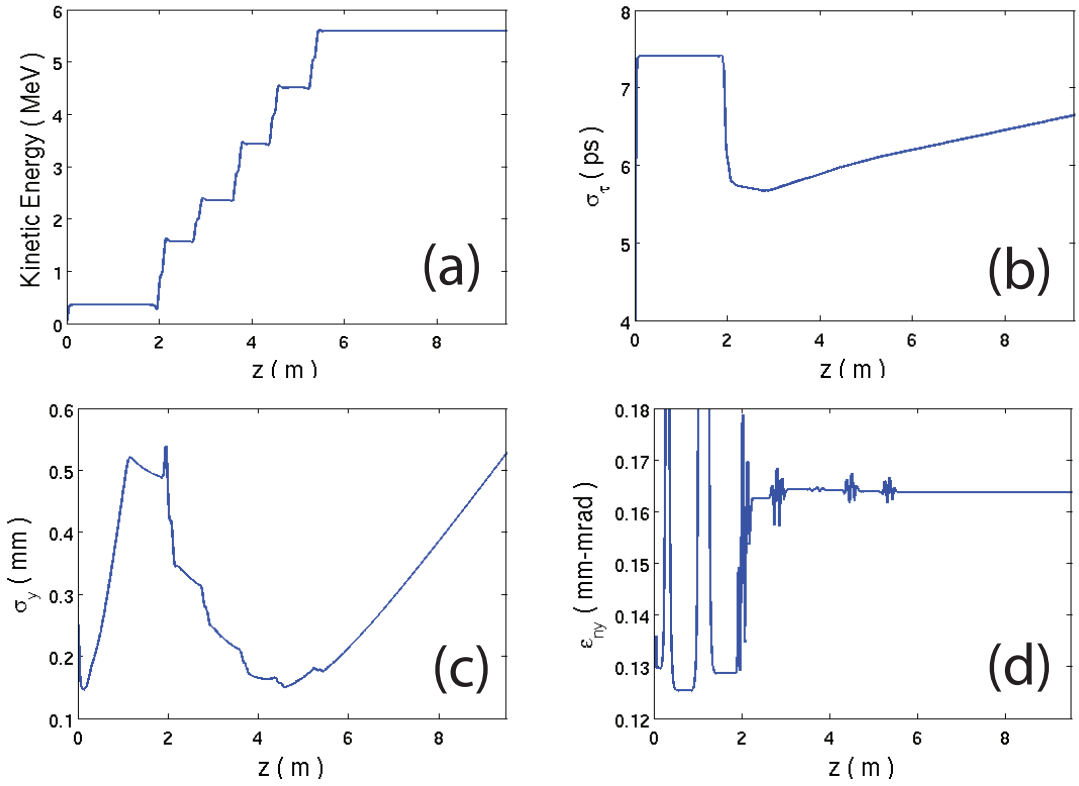

Figure 7.5: Beam envelope evolutions for the near-zero bunch charge case, the machine settings are listed in Table. 7.1. a) the kinetic energy (KE), b) the bunch length (σ_τ), c) beam size (σ_y), d) normalized vertical emittance (ϵ_{ny}).

happens to be worse from time to time due to the misalignment of the optical path. The peaks from the experiment are broader compared to the simulation, which indicates that the electron beam distribution is smoothed out in the beamline, which could come from the space charge effects. Smaller time indicates that this part of the beam arrives early, which we call the beam head, and it is focused due to the time-dependent RF focusing and therefore has higher intensity; the tilted intensity distribution is a signature that the beam is slightly off-crest, and is closer to the bunching phase. The slice emittance is shown in Fig. 7.6(d), it is really close to 0.12 mm-mrad, which is the thermal emittance from the photocathode, the thermal emittance is well-preserved at the near-zero bunch charge,

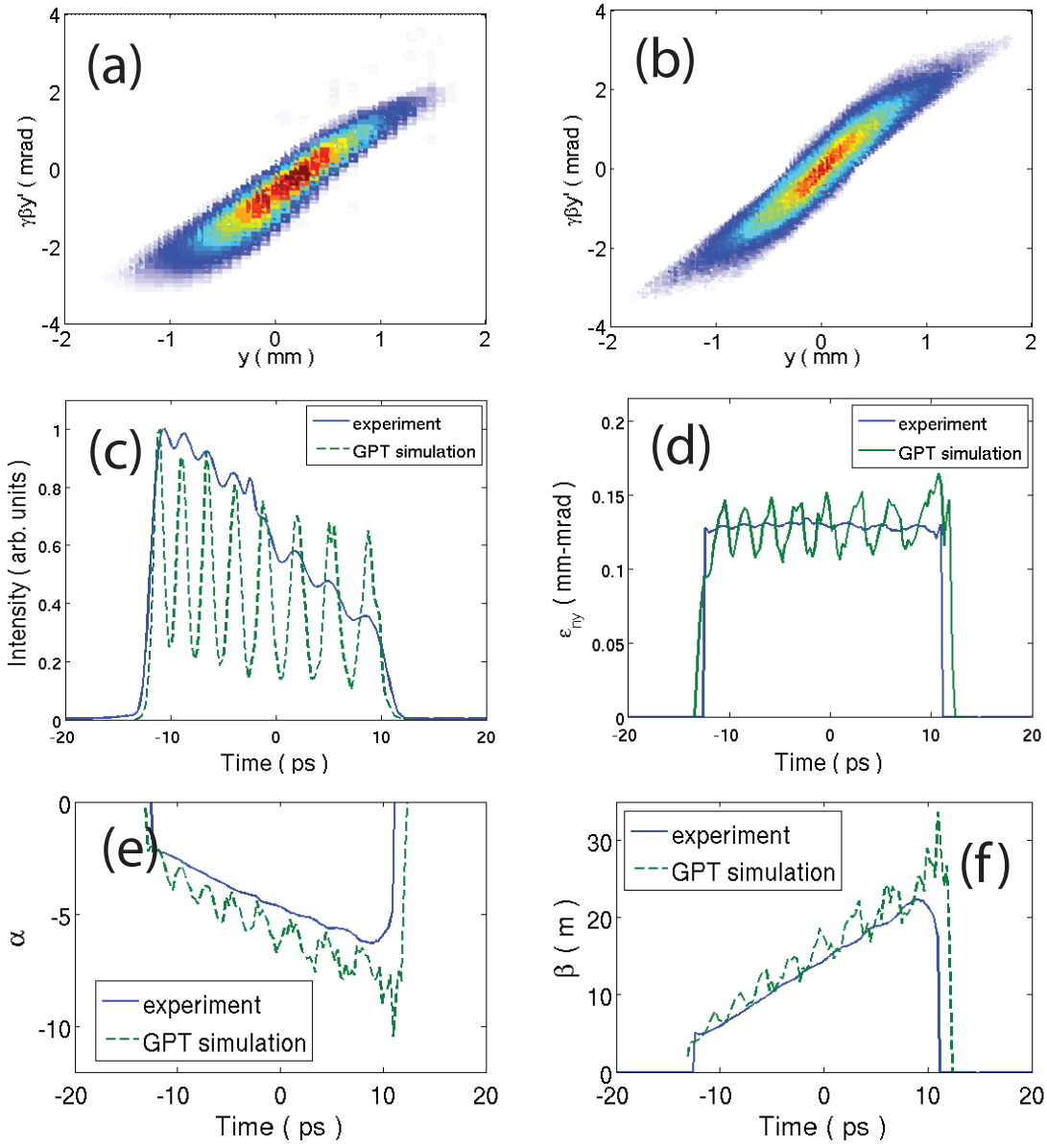

Figure 7.6: The slice emittance measurement and GPT simulation at the near-zero bunch charge. a) the measured vertical projected emittance, b) the simulated vertical projected emittance, c) the beam intensity, d) the slice emittance, e) the Twiss parameter α, f) the Twiss parameter β. The solid lines are the measurement, the doted lines are the GPT simulation.

and the (small) emittance growth mainly comes from the RF time-dependent focusing; the simulation shows more fluctuations the average value, which can come from the noise of the pseudo-random number generator, these features become smoother at the higher bunch charge. The Twiss parameter α is shown in Fig. 7.6(e), where the measurement and simulation show similar trend and agree with each other reasonably well. The β-function is depicted in Fig. 7.6(f), again, the measurement and simulation agree with each other well: at the on-crest RF phases and the near-zero bunch charge, the beam head gets focused both transversely and longitudinally; therefore, it has smaller size compared to the beam tail.

We achieved the good agreement for the slice emittance measurement between the experiment and simulation at the near-zero bunch charge case, which demonstrates the capability of this method and we employ it to explore the higher bunch charge regime.

7.4 The slice emittance at full bunch charge

It is challenging to maintain small emittance at the higher bunch charge, especially at the full bunch charge. The emittance compensation is more complicated for photoinjectors with a dc gun which has relative lower energy compared to the ones with a RF gun [6, 7, 11]. Almost every key element in the photoinjector couples together in the emittance compensation, such as the laser spatial and temporal profile, the solenoid strength, the buncher voltage, the SRF voltages and phases. We run multivariate genetic optimizer to narrow down the parameter phase space and test these solutions in experiments, and then perform

the experimental scan around the simulated values for the beamline elements thanks to the fast EMS.

The projected transverse emittance was measured in the photoinjector before, however, we encountered numerous issues and could not reduce the emittance below 3.6 mm-mrad for quite some time. It turned out that the alignment of the beam line is crucial: to the first order the emittance growth is proportional to the position offset of the misalignment [3]. Then we aligned the elements in the beamline to resolve this issue: we aligned the buncher, the first two SRF cavities one by one, then we aligned the two solenoids physically. By doing this we are able to reduce the emittance below 1 mm-mrad, and we present our measurements here.

7.4.1 The multi-variable optimization result at 80 pC, 5 MeV

We have used GPT to simulate the beam operation at 80 pC bunch charge, 5 MeV beam energy. The temporal laser intensity distribution is produced by passing through three (later four) YVO_4 shaping crystals, the transverse laser intensity profile is the Gaussian distribution truncated at its FWHM. In order to simplify the experimental situation, the gun HV is set to 350 kV, the SRF cavity amplitudes are set to 1395, 825, 1100, 1100, 1100 kV, and the buncher is set to the bunching mode. We varied the transverse laser beam size, the two solenoid currents and the buncher voltage to minimize the transverse emittance at 80 pC, 5 MeV. The simulations were performed with two thousand particles [Fig. 7.7]. Simulation with two hundred thousand particles show similar trend. 0.6 mm-mrad optimized emittance can be obtained as Fig. 7.7(a) with bunch length as

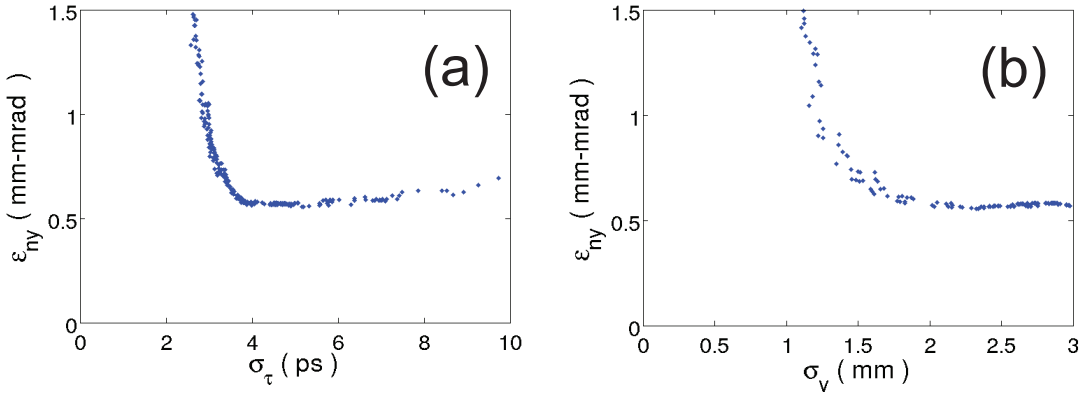

Figure 7.7: The emittance optimization front at full bunch charge 80 pC. a) the bunch length vs. the vertical emittance, b) the vertical beam size vs. the emittance.

short as 4 ps rms; at the optimized 0.6 mm-mrad emittance, the smallest beam size is at 1.5 mm, as shown in Fig. 7.7(b).

7.4.2 The 80 pC slice emittance measurement

We measured the slice emittance at several different machine settings from the simulation guidance. Here we present one that has the vertical projected emittance 0.83 mm-mrad and beam size 1.7 mm, which agree well with the simulation; although the bunch length is measured to be 15 ps rms which is about twice longer than the predicted 8 ps rms. We attribute the longer bunch length to the initially incorrect buncher calibration, the transient effect of the RF cavities, and the SRF cavity phasing; these were discussed in the previous chapter.

The machine settings are listed in Table. 7.2. A multi-alkali photocathode is placed in the gun which has 160 meV MTE. The laser beam passes through three (later four) YVO_4 birefringent shaping crystals to produce the near flat-top tem-

poral profile with 33 ps FWHM [Fig. 7.8(a, b)], and it is truncated by an iris with 2.5 mm diameter at its fwhm [Fig. 7.8(c)] to optimize the transverse space charge effect [3]. The first solenoid current is -3.66 A and it focuses the electron beam inside the buncher, the buncher operates at 54 kV and compresses the beam in the time domain, the second solenoid current is 2.37 A and it focuses the beam before the beam enters the cryomodule. The kinetic energy after the cryomodule is measured to be 5.2 MeV which is lower compared to the simulated 5.7 MeV [Fig. 7.9(a)], most of the error comes from the miscalibration of the SRF cavity amplitudes. The bunch is elongated by the space charge effect just after leaving the cathode, to 20 ps rms, then it is compressed to 14 ps rms by the buncher, then further compressed to 9 ps rms by the first SRF cavity, and stabilized to 8 ps rms after the cryomodule [Fig. 7.9(b)]. The beam size increases rapidly to 5 mm driven by the transverse space charge effect, then it is focused by the first solenoid to 4 mm, and further down to 2 mm by the second solenoid just before the first SRF cavity, then the on-crest time-dependent RF focusing keeps the beam size to 1.8 mm at the first slit of the EMS [Fig. 7.9(c)]. The vertical emittance also increases swiftly from its thermal emittance 0.24 mm-mrad to 0.8 mm-mrad and keeps growing; then the solenoid focusing, the buncher focusing and the SRF cavity focusing work together to cancel the emittance growth from the transverse space charge effect and stabilize it to 0.8 mm-mrad inside the cryomodule and further reduces it to 0.7 mm-mrad at the first slit of the EMS [Fig. 7.9(d)]; with more particles in the simulation, the vertical emittance is reduced to 0.5 mm-mrad.

The measured projected vertical emittance is shown in Fig. 7.10(a), $\epsilon_{ny}^{\mathrm{exp}} \approx 0.8$ mm-mrad, $\sigma_y^{\mathrm{exp}} \approx 1.7$ mm, they are not too far away from the simulated results $\epsilon_{ny}^{\mathrm{sim}} \approx 0.5$ mm-mrad, $\sigma_y^{\mathrm{sim}} \approx 1.8$ mm; meanwhile, the phase space distribu-

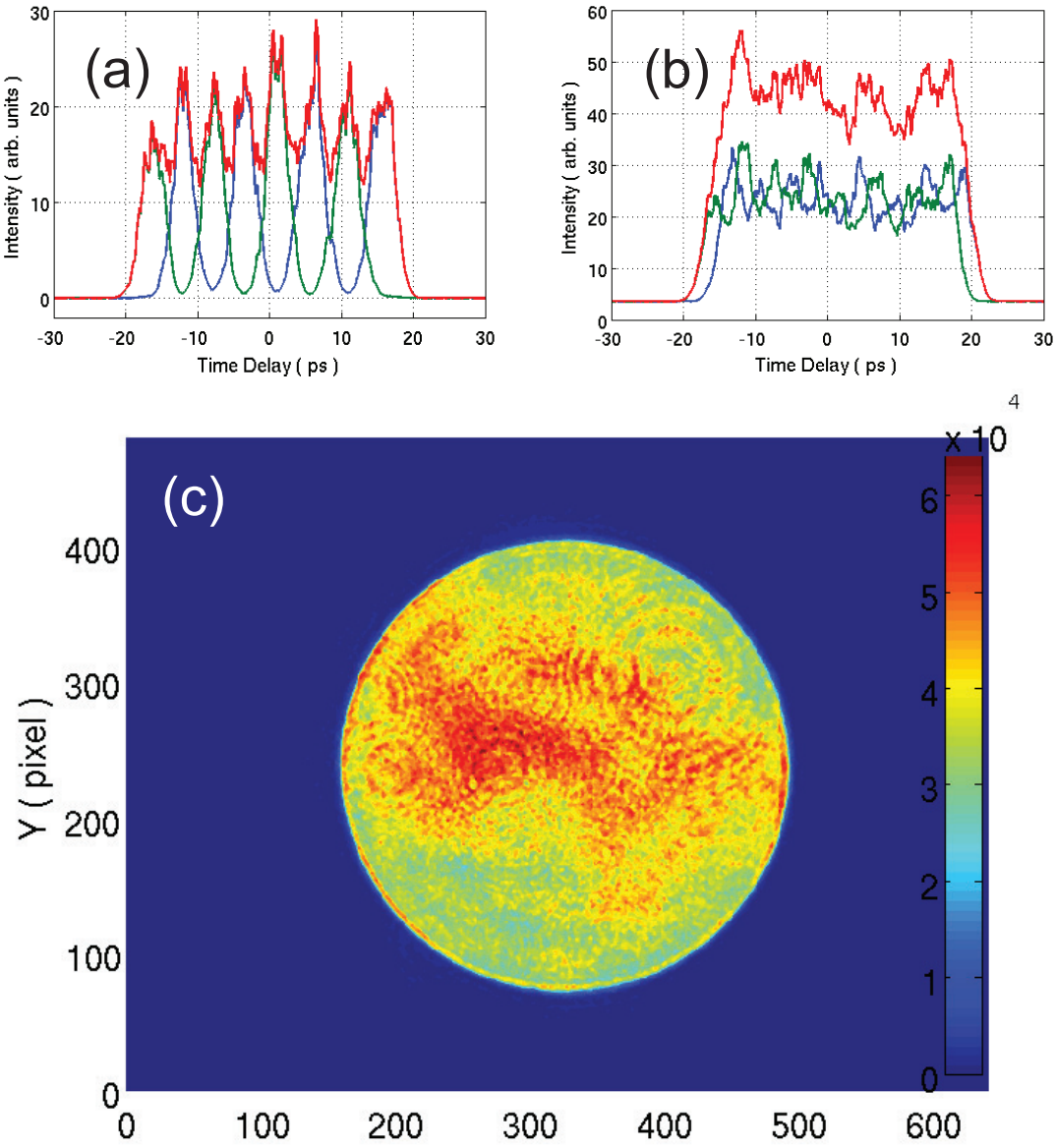

Figure 7.8: The laser beam profile. a) the temporal distribution with three YVO_4 shaping crystals; b) the temporal distribution with four YVO_4 shaping crystals; blue: the vertical polarization, green: the horizontal polarization; red: the total intensity. c) the transverse laser profile.

Table 7.2: The Cornell ERL photoinjector settings for the 80 pC case. The RF phase values are respect to the on-crest values.

Components	Parameters	RF phases
Laser σ_τ	33 ps fwhm	
Laser $\sigma_{x/y}$	0.44 mm rms	
Cathode MTE	160 meV	
Gun HV	350 kV	
Iris size	1.75 mm	
Solenoid 1	-3.66 A	
Buncher	63 kV	-90°
Solenoid 2	2.37 A	
SRF1 cavity	1395 kV	0°
SRF2 cavity	825 kV	0°
SRF3 cavity	1100 kV	0°
SRF4 cavity	1100 kV	0°
SRF5 cavity	1100 kV	0°
VDC	60 kV	

tion is also close to the simulated result in Fig. 7.10(b). The measured bunch length is about 15 ps rms, which is about twice longer than the simulated 8 ps rms, we attribute this to the lower buncher voltage, the transient effect of the RF cavities, and the SRF cavity phasing method, which were discussed in the previous chapter. Despite the large discrepancy, the temporal intensity has similar shape, it looks like a tilted Gaussian distribution, with the sharp edge in the beam head and the longer tail in the beam tail, which is produced by the longitudinal space charge effect: the head is accelerated to experience more RF

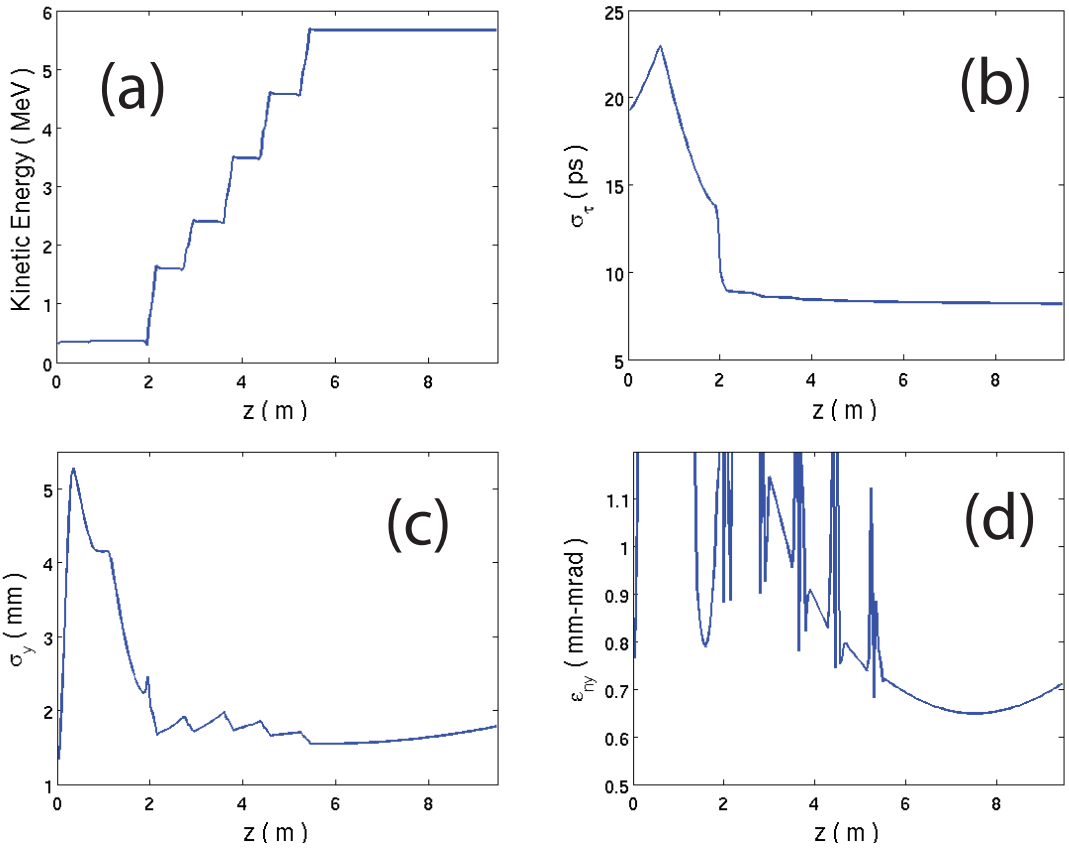

Figure 7.9: Beam envelope evolutions for the 80 pC case, the machine settings are listed in Table. 7.2. a) the kinetic energy (KE), b) the bunch length (σ_τ), c) beam size (σ_y), d) normalized vertical emittance (ϵ_{ny}).

time-dependent focusing and the tail is de-accelerated; all the peaks from the shaping crystals are smoothed out by the same longitudinal space charge effect [Fig. 7.10(c)]. The measured slice emittance is between 0.2 and 0.7 mm-mrad, even the slice emittance is larger than the thermal emittance 0.24 mm-mrad, again from the transverse space charge effect [Fig. 7.10(d)]; the simulated slice emittance has the similar distribution shape but with lower value, between 0.2 and 0.4 mm-mrad, the slice emittance misalignment contributes to the larger observed 0.8 mm-mrad. The transverse space charge effect has a much large effect on the emittance growth when compared to the slice emittance misalignment.

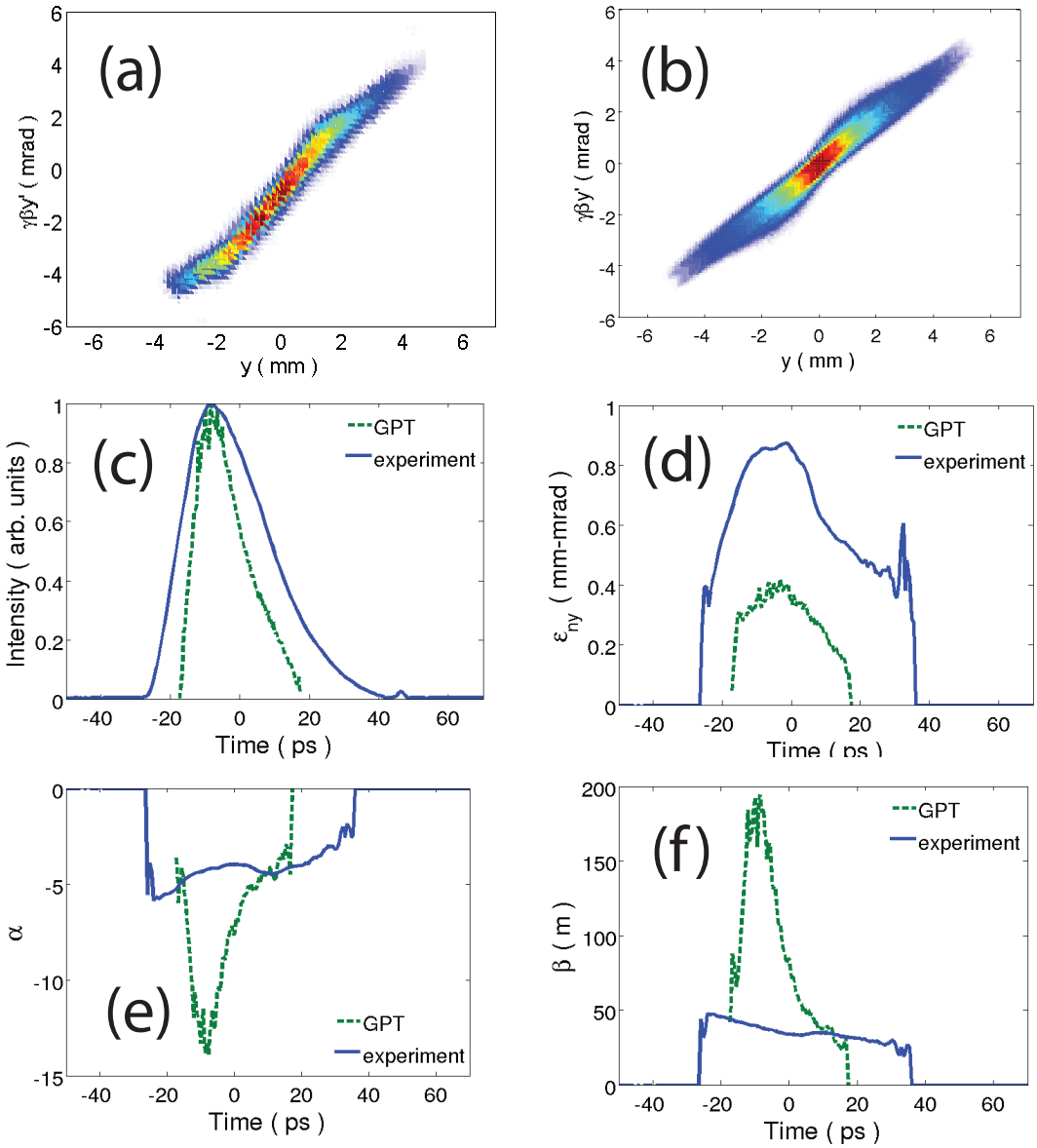

Figure 7.10: The slice emittance measurement and GPT simulation at the full bunch charge 80 pC. a) the measured vertical projected emittance, b) the simulated vertical projected emittance, c) the beam intensity, d) the slice emittance, e) the Twiss parameter α, f) the Twiss parameter β. The solid lines are the measurement, the doted lines are the GPT simulation.

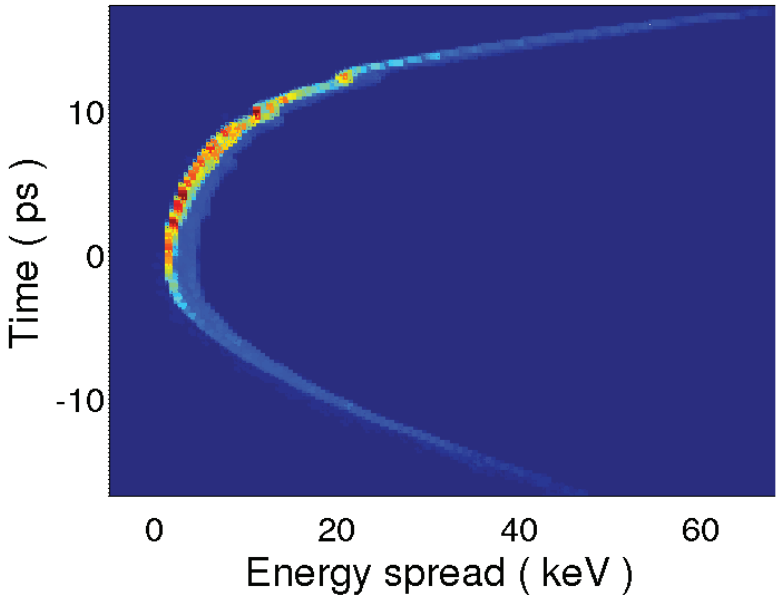

Figure 7.11: The time-resolved energy spread GPT simulation at 80 pC bunch charge.

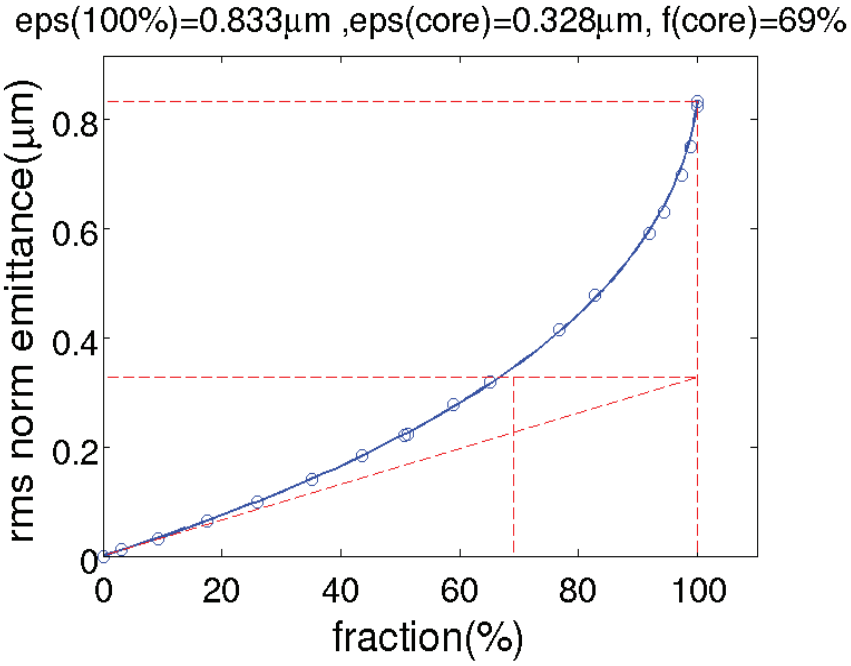

Figure 7.12: The beam fraction vs. beam emittance, 80 pC bunch charge.

The Twiss parameters α and β are depicted in Fig. 7.10(e) and (f), the larger charge density results in a larger beam diameter, as we expected from the transverse space charge effect. We observed an even larger discrepancy which come from the bunch length difference and slice emittance difference. Although the discrepancy exists, this is the smallest transverse emittance that has ever been reported for a laser-driven photoinjector with a DC gun. We are still investigating the bunch length discrepancy despite the knowledge we already learned from the experiments. We did not measure the time-resolve energy spread when we did the experiment, but the GPT simulation result is depicted in Fig. 7.11: the 'C' shape shows that the RF phases are on-crest; the energy spread is 12 keV rms while the bunch length is 7.5 ps rms. It is also worth noticing that although the entire projected emittance is 0.8 mm-mrad, the core part of the projected emittance is 0.3 mm-mrad, and it contains 70% of the electrons of the entire bunch as shown in Fig. 7.12. This ultra-low emittance was reported as one milestone of the Cornell ERL [1]. The core emittance is inverse proportional to the peak power and is a merit for the non-Gaussian shape electron beam distribution, and could contribute more to the x-ray generation process [16].

We spent quite some time to investigate the measured bunch length discrepancy. There are three main effects contributing to this discrepancy. The first one is that the buncher has only 86% strength than it should be; this effect alone elongates the bunch length by a factor of two. The second one is the RF transient effect from the buncher and the SRF cavities; these transient effects artificially elongate the measured averaged bunch length by up to 50%. The last one is the SRF phasing method, we used the minimum arrival time to phase the SRF cavities; this would elongates the bunch length by 20% as described in the previous chapter.

Table 7.3: The Cornell ERL photoinjector settings for the 80 pC case. The RF phase values are respect to the on-crest values. These machine settings count the real buncher strength and the RF phasing effects.

Components	Parameters	RF phases
Laser σ_τ	33 ps fwhm	
Laser $\sigma_{x/y}$	0.44 mm rms	
Cathode MTE	160 meV	
Gun HV	350 kV	
Iris size	1.75 mm	
Solenoid 1	-3.66 A	
Buncher	53 kV	-90°
Solenoid 2	2.37 A	
SRF1 cavity	1395 kV	+6.5°
SRF2 cavity	825 kV	+1.5°
SRF3 cavity	1100 kV	+1.5°
SRF4 cavity	1100 kV	+1.5°
SRF5 cavity	1100 kV	+4.0°
VDC	60 kV	

We re-ran the simulation to count the buncher strength and the RF phasing effects. Table. 7.3 lists the realistic machine settings. The beam envelope evolutions are depicted as shown in Fig. 7.13. The beam energy is about the same as Fig. 7.9(a). The bunch length increases to 15 ps rms [Fig. 7.13(b)], that is close to the measured 15 ps rms. It is also worth to notice that we do not count the RF transient effect in the simulation, although the convolution effect is small compared to the other effects. The beam size decreases to 1.3 mm rms

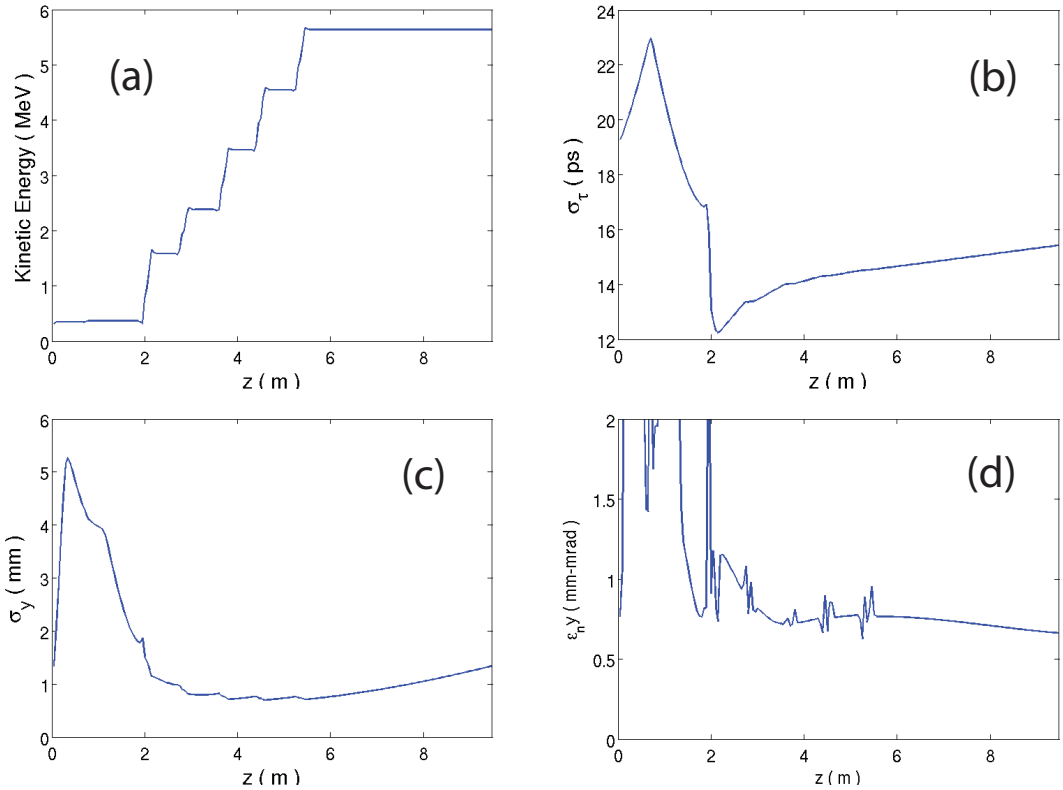

Figure 7.13: Beam envelope evolutions for the 80 pC case, the machine settings are listed in Table. 7.3. a) the kinetic energy (KE), b) the bunch length (σ_τ), c) beam size (σ_y), d) normalized vertical emittance (ϵ_{ny}).

[Fig. 7.13(c)]. The emittance is still around 0.7 mm-mrad [Fig. 7.13(d)]. The experimental and GPT simulated projected emittances are shown in Fig. 7.14(a, b), they have different shape. The time resolved parameters are depicted as shown in Fig. 7.14(c, d, e, f), the bunch length is very close, and the slice emittance has similar shape, while the Twiss parameter α and β have different trend; overall, the discrepancy is smaller compared to the previous results as shown in Fig. 7.10; because it is closer to the realistic experiments.

After we have resolved all these issues, we measured the slice emittance again at 80 pC bunch charge, 5 MeV beam energy. This time we also measured

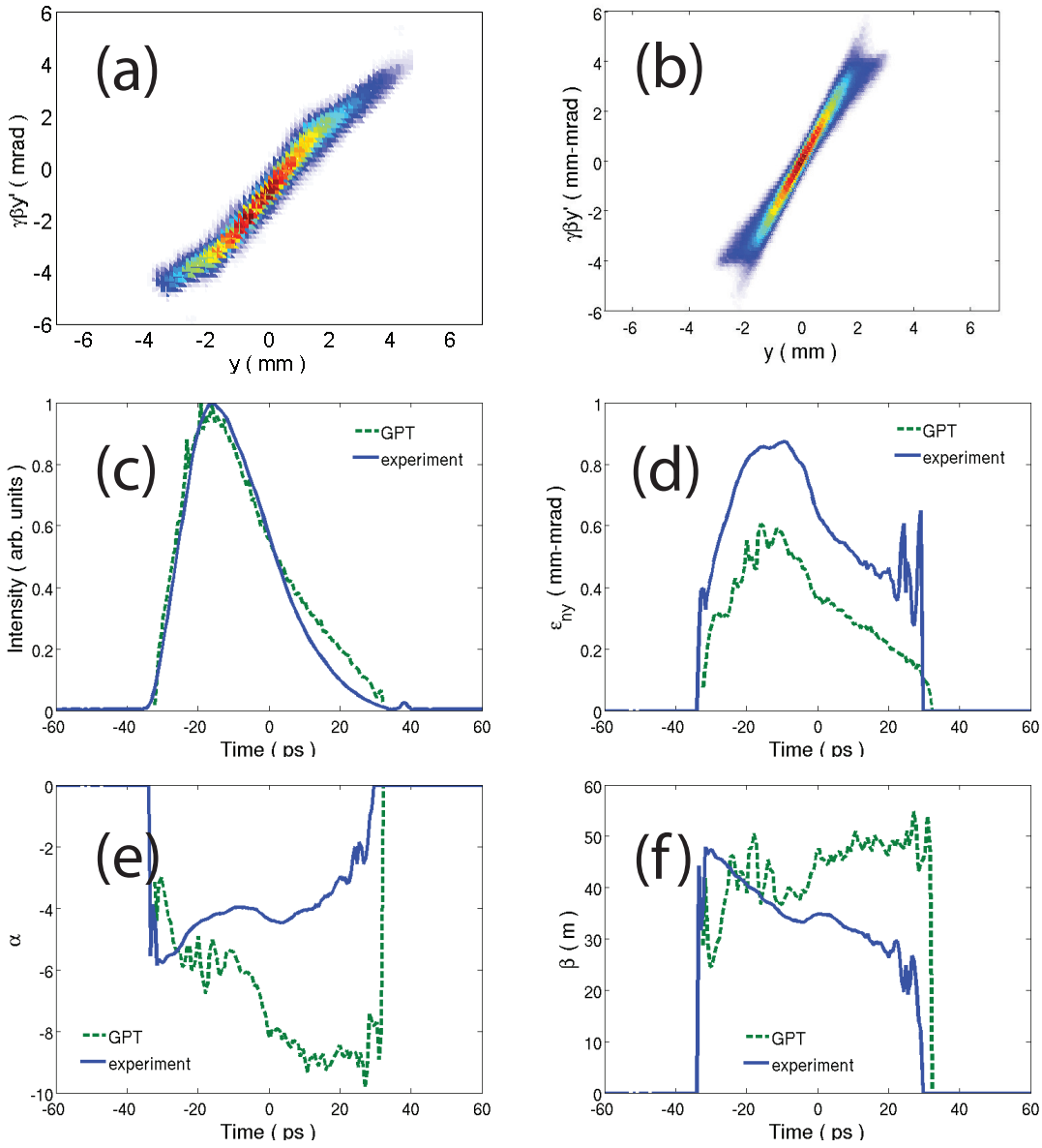

Figure 7.14: The slice emittance measurement and GPT simulation at the full bunch charge 80 pC in the realistic settings; the machine settings are listed in Table. 7.3. a) the measured vertical projected emittance, b) the simulated vertical projected emittance, c) the beam intensity, d) the slice emittance, e) the Twiss parameter α, f) the Twiss parameter β. The solid lines are the measurement, the doted lines are the GPT simulation.

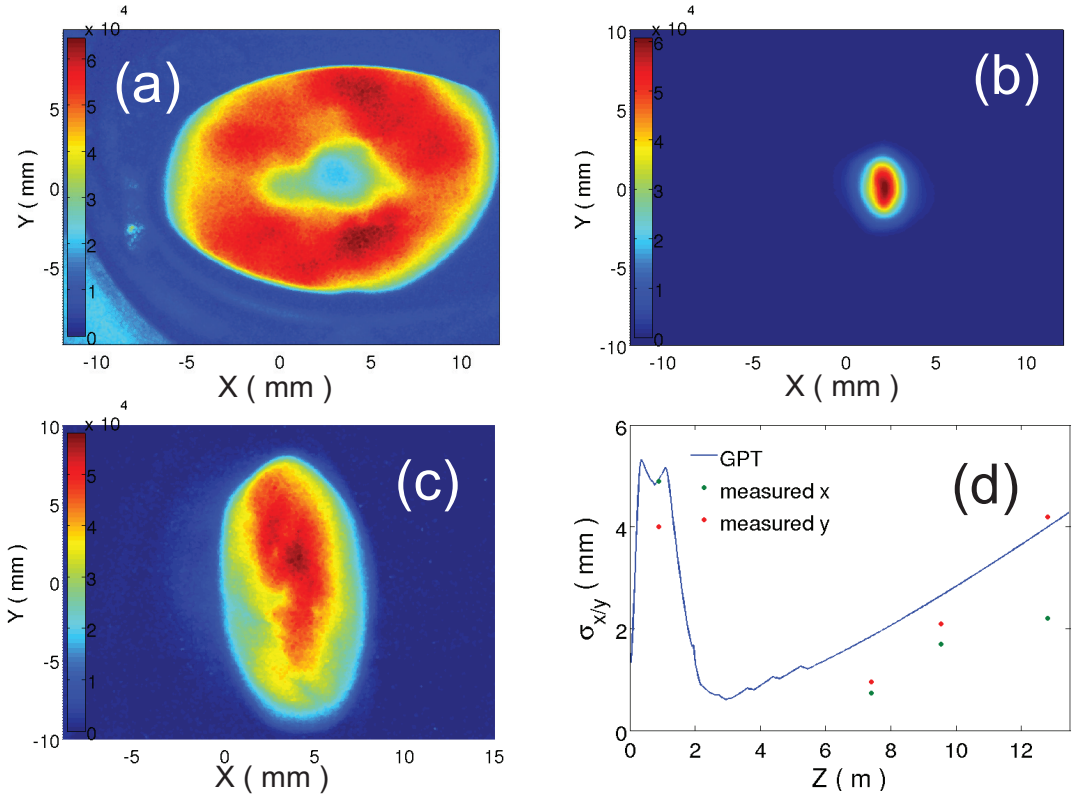

Figure 7.15: The beam size at different beamline locations. a) the beam on the A1 view screen (the center part is a dead spot on the view screen), b) the beam on the A3 view screen, c) the beam on the A4 view screen, d) the beam size measured at different beam locations, the line is the simulation, the dots are the experiment data.

the beam size at different locations of the beamline [Fig. 7.15] at the full bunch charge 80 pC. The A1 view screen is located at 0.890 m downstream the photocathode, the beam size there is 5 mm rms, the center part of the view screen is damaged by the electron beam and has lower response [Fig. 7.15(a)]. The A3 view screen is located at just after the cryomodule, 7.397 m downstream the photocathode, the beam size is 0.7, 0.8 mm rms in the horizontal and vertical planes respectively [Fig. 7.15(b)]. The A4 view screen locates at 12.806 m downstream the photocathode, the beam size is 2.0, 4.0 mm rms in the horizontal and vertical planes [Fig. 7.15(c)], the beam is elliptical. We are not sure what causes the

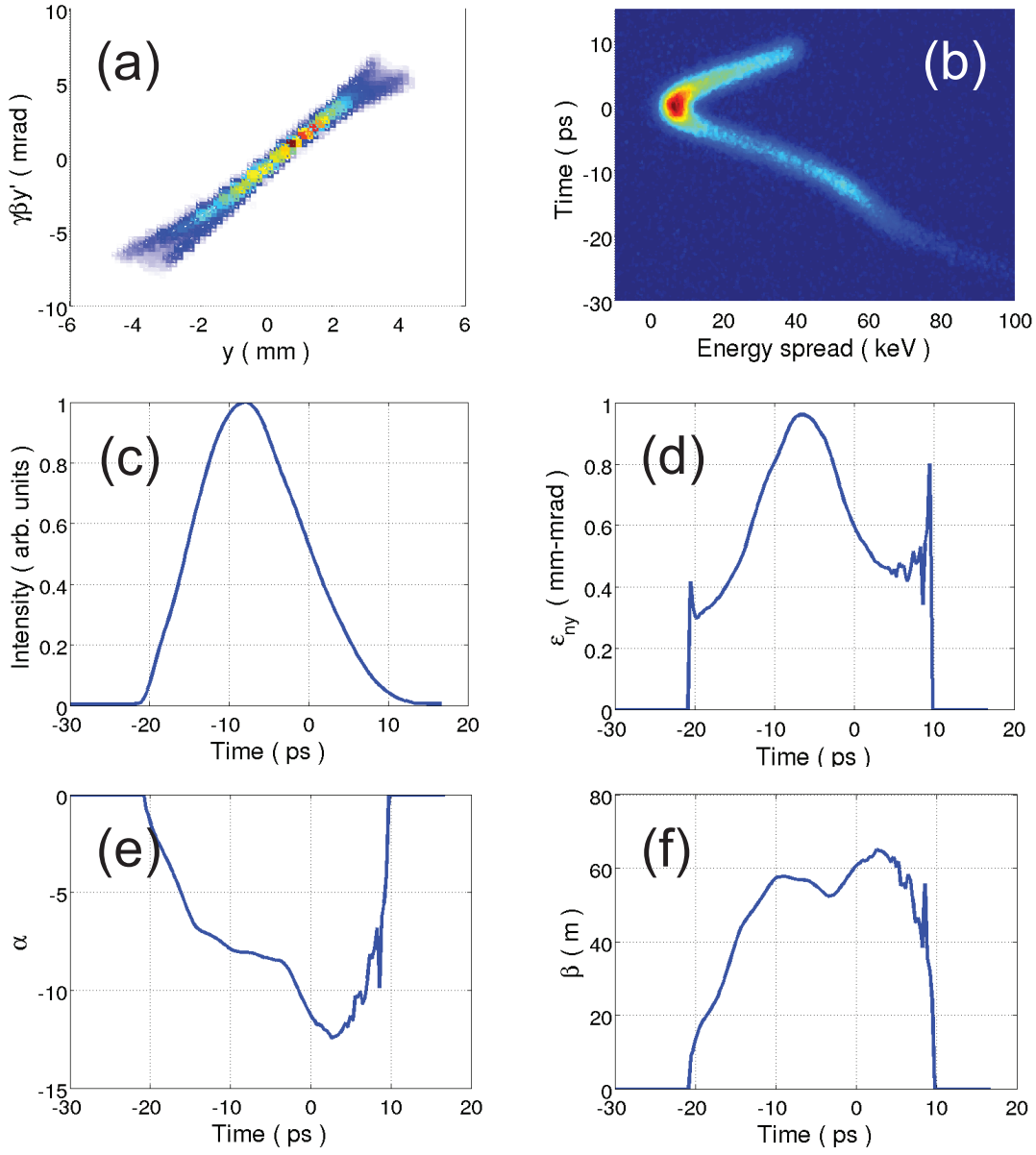

Figure 7.16: The slice emittance measurement at the full bunch charge 80 pC. a) the vertical projected emittance, b) the time-resolved energy spread, c) the beam intensity, d) the slice emittance, e) the Twiss parameter α, f) the Twiss parameter β.

elliptical shape of the beam, it could come from the residual quadrupole fields, the misalignment inside the SRF cavities or the space charge effects. Fig. 7.15(d) depicts the simulated beam size at varied locations, the experiments results are plotted as dots; they agree with each other fairly well. The bunch length does get shorter, 8 ps rms, however, the projected emittance is larger, 1.4 mm-mrad [Fig. 7.16(a)]. We measured the time-resolved energy spread as well, it also has the 'C' shape because most of the beam sits on-crest of the RF fields [Fig. 7.16(b)]. The energy spread is 18 keV rms while the bunch length is 7.3 ps rms. The bunch intensity is presented in Fig. 7.16(c), the bunch head has steeper edges because it is closer to the bunching phase and gets compressed a little bit. The slice emittance varies from 0.3 mm-mrad to 1 mm-mrad, the center part of the beam has the larger slice emittance while the head and tail part has the smaller slice emittance [Fig. 7.16(d)]. The Twiss parameters α and β are depicted in Fig. 7.16(e, f), they have complicated structures, that could come from the space charge effects and the interactions between the beam and elements in the beamline. It is interesting to notice that the Twiss parameter α and β have similar shape as the simulation results depicted in Fig. 7.14(e, f).

Besides these data above, we measured the slice emittance at the 80 pC bunch charge when the SRF cavities are slightly off-crest as predicted by the simulations. The normalized vertical emittance ϵ_{ny} and beam size σ_y were measured to be 0.8 mm-mrad and 1 mm, which agree well with the 0.8 mm-mrad and 0.8 mm values predicted by simulation. However, the pulse duration was measured to be 19 ps rms which is much longer than the simulation result 7 ps rms. The systematic discrepancy observed at the high bunch charge lead to us to investigate the causes of the elongation of the electron bunch length, that is discussed in the previous chapter.

7.5 Conclusions

We demonstrated the slice emittance measurement at the near-zero bunch charge with 380-fs rms time resolution, which is sufficient to diagnose electron bunches with few-ps rms bunch length. We also measured 0.8 mm-mrad vertical emittance from this diagnostic which is the smallest number that has ever been achieved from a laser driven DC gun photoinjector at a usable bunch charge. The core part has emittance 0.3 mm-mrad and it was reported as one milestone of the Cornell ERL. This diagnostic shows good agreement at the near-zero bunch charge and has larger bunch length measurement error at the higher bunch charge, that we attribute to the lower buncher voltage, the RF transient effects, and the phasing method of the SRF cavities. We are still investigating this issue. Despite this disadvantage, this diagnostic provides the multi-dimensional characterization of the electron beam which can give us the insight of the beam dynamics and more importantly, to help minimize the emittance for the operating conditions of the Cornell ERL. Furthermore, we plan to use this diagnostic to optimize the laser beam profile incident on the cathode to minimize the transverse emittance.

7.6 Acknowledgments

We would like to acknowledge the colleagues continuously working on this project. This work was supported by NSF award DMR-0807731.

BIBLIOGRAPHY

[1] ILC Newsline, http://newsline.linearcollider.org/2012/03/29/triple-milestone-for-cornells-erl-programme/.

[2] S. M. Gruner, D. Bilderback, I. Bazarov, K. Finkelstein, G. Krafft, L. Merminga, H. Padamsee, Q. Shen, C. Sinclair, and M. Tigner, "Energy recovery linacs as synchrotron radiation sources (invited)", Rev. Sci. Instrum. **73**, 1402 (2002).

[3] I. V. Bazarov, A. Kim, M. N. Lakshmanan, and J. M. Maxson, "Comparison of dc and superconducting rf photoemission guns for high brightness high average current beam production", Phys. Rev. ST Accel. Beams **14**, 072001 (2011).

[4] X. Qiu, K. Batchelor, I. Ben-Zvi, and X-J. Wang, "Demonstration of Emittance Compensation through the Measurement of the Slice Emittance of a 10-ps Electron Bunch", Phys. Rev. Lett. **76**, 3723 (1996).

[5] M. Rohrs, C. Gerth, H. Schlarb, B. Schmidt and P. Schmuser, "Time-resolved electron beam phase space tomography at a soft x-ray free-electron laser", Phys. Rev. ST Accel. Beams **12**, 050704 (2009).

[6] R. Akre, D. Dowell, P. Emma, J. Frisch, S. Gilevich, G. Hays, Ph. Hering, R. Iverson, C. Limborg-Deprey, H. Loos, A. Miahnahri, J. Schmerge, J. Turner, J. Welch, W. White, and J. Wu, "Commissioning the Linac Coherent Light Source injector", Phys. Rev. ST Accel. Beams **11**, 030703 (2008).

[7] Y. Ding, A. Brachmann, F.-J. Decker, D. Dowell, P. Emma, J. Frisch, S. Gilevich, G. Hays, Ph. Hering, Z. Huang, R. Iverson, H. Loos, A. Miahnahri, H.-D. Nuhn, D. Ratner, J. Turner, J. Welch, W. White, and J. Wu , "Measurements and Simulations of Ultralow Emittance and Ultrashort Electron Beams in the Linac Coherent Light Source", Phys. Rev. Lett. **102**, 254801 (2009).

[8] B. E. Carlsten, "New photoelectric injector design for the Los Alamos National Laboratory XUV FEL accelerator", Nucl. Instrum. Methods Phys. Res., Sect. A **285**, 313 (1989).

[9] S. Belomestnykh, I. Bazarov, V. Shemelin, J. Sikora, K. Smolenski, V. Veshcherevich, "Deflecting cavity for beam diagnostics at Cornell ERL injector", Nucl. Instrum. Methods Phys. Res., Sect. A **614**, 179 (2010).

[10] S. G. Anderson, J. B. Rosenzweig, G. P. LeSage, and J. K. Crane, "Space-charge effects in high brightness electron beam emittance measurements", Phys. Rev. ST Accel. Beams **5**, 014201 (2002).

[11] A. W. Chao, and M. Tigner, "Handbook of Accelerator Physics and Engineering", World Scientific, (2009).

[12] I. V. Bazarov, B. M. Dunham, C. Gulliford, Y. Li, X. Liu, C. K. Sinclair, K. Soong, and F. Hannon, "Benchmarking of 3D space charge codes using direct phase space measurements from photoemission high voltage dc gun", Phys. Rev. ST Accel. Beams **11**, 100703 (2008).

[13] S. Zhou, D. G. Ouzounov, H. Li, I. Bazarov, C. Sinclair, and F. W. Wise, "Efficient temporal shaping of ultrashort pulses with birefringent crystals", Appl. Opt. **46**, 8488 (2007).

[14] I. V. Bazarov, D. G. Ouzounov, B. M. Dunham, S. A. Belomestnykh, Y. Li, X. Liu, R. E. Meller, J. Sikora, C. K. Sinclair, F. W. Wise, and T. Miyajima, "Efficient temporal shaping of electron distributions for high-brightness photoemission electron guns", Phys. Rev. ST Accel. Beams **11**, 040702 (2008).

[15] K. J. Kim, "Rf and space-charge effects in laser-driven rf electron guns", Nucl. Instrum. Methods A **275**, 201 (1989).

[16] I. V. Bazarov, "Synchrotron radiation representation in phase space", Phys. Rev. ST Accel. Beams **15**, 050703 (2012).